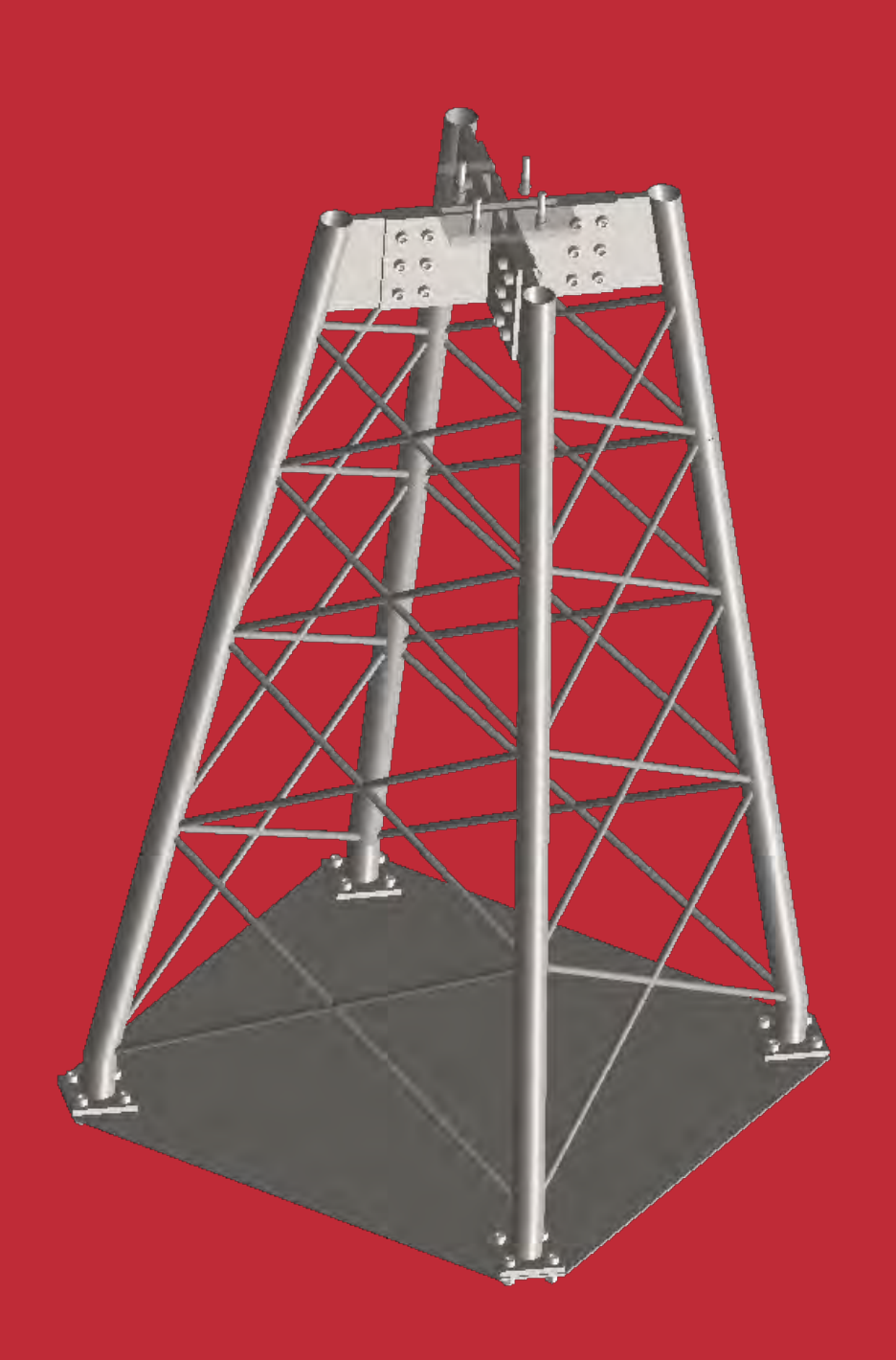


# Design and dynamic monitoring of a jacket foundation model by a digital twin.

# **Master Thesis**

Gian Marco Maratta



#### Design and dynamic monitoring of a jacket foundation model by a digital twin.

Master Thesis June, 2025

Ву

Gian Marco Maratta

ECTS: 30

Supervisors: Jan Becker Høgsberg & Mikkel Tandrup Steffensen

Copyright: Reproduction of this publication in whole or in part must include the cus-

tomary bibliographic citation, including author attribution, report title, etc.

Cover photo: Mock-up jacket modeled in SolidWorks by Gian Maratta, 2025

Published by: DTU, Department of Civil and Mechanical Engineering, Koppels Allé,

Building 404, 2800 Kgs. Lyngby, Denmark Denmark

www.construct.dtu.dk

## **Approval**

This thesis is the final step toward the completion of the Master of Science in Civil Engineering at the Technical University of Denmark (DTU). The project presented in this document accounts for 30 credits in the European Credit Transfer System (ECTS), with a starting date on the 20th of January 2025, and a submission date on the 20th of June 2025.

The process of this thesis is done for a specific case at Ramboll, and it has been performed under the supervision of Jan Becker Høgsberg, Associate Professor of the Department of Civil and Mechanical Engineering at DTU, and Mikkel Tandrup Steffensen, Postdoctoral Researcher.

The project has utilized AI to proofread, improve language, initialize, and modify specific data processing scripts.

Gian Marco Maratta - s230213

Signature

20/06/2025

Date

#### Abstract

This project investigates the design and dynamic monitoring of a jacket foundation model using a digital twin. This digital twin should be able to detect damages based on Structural Health Monitoring (SHM) system utilizing straightforward, existing tools. The system tracks changes in the structure's natural frequencies and mode shapes as indicators of potential damage.

In order to check the methodology and perform quality assurance on the method, the procedure is carried out first in a simple three-story frame structure, and then in a scaled jacket foundation proposed by Ramboll.

The experimental methodology consists of vibration tests analyzed with two methods: Experimental Modal Analysis (EMA) and Operational Modal Analysis (OMA). The former is well known for being more precise than the latter, since the experiments are carried out under controlled conditions and measured external forces. However, the OMA approach is beneficial in analyzing structures in real world conditions without artificial excitation.

The digital twin includes a numerical methodology and a Pyhton tool. The former consists of a Finite Element Model Updating (FEMU) approach, which involves calibrating some mechanical parameters of the model to obtain a closer representation of the real structure, while the latter consists of script that compares the modal properties of the healthy numerical model against damaged numerical models, and the healthy numerical model against the real structure (whose damage state is unknown). Using Euclidean distances, the type and location of a damage can be predicted.

The method is able to predict the location of damages in the three-story frame structure with an accuracy of at least 93.3% for an average relative change in frequency of 2.5%, and in the scaled jacket structure with an accuracy of 90% for an average relative change in frequency of 6.3%. However, it should be noted that the method is in an early stage and therefore different types and severity of damage should be included in future work to achieve a better estimate of the accuracy of the method.

Keywords: Jacket foundation, offshore wind turbine, Digital Twin (DT), Structural Health Monitoring (SHM), Operational Modal Analysis (OMA), Experimental Modal Analysis (EMA).

## **Acknowledgements**

I would like to express my heartfelt gratitude to everyone who supported me throughout the journey of this thesis.

First and foremost, I am deeply thankful to my thesis supervisor, Jan Becker Høgsberg, Associate Professor of the Department of Civil and Mechanical Engineering at the Technical University of Denmark (DTU), as well as my co-supervisor, Mikkel Tandrup Steffensen, Postdoctoral Researcher, for their dedicated guidance, insightful feedback, and continuous support throughout the project. Their combined expertise and encouragement have been invaluable, not only in shaping the direction of this thesis but also in contributing to my growth as a future professional.

I am also sincerely grateful to Johnny Sølvtorp and Torben Bender Christensen from the DTU Construct's workshop for their invaluable assistance in constructing the structure and accessories used in the experimental work. Their craftsmanship, flexibility, and willingness to help played a key role in making the physical setup possible.

Finally, I extend my warmest thanks to my friends and family, whose encouragement, patience, and understanding have been a constant source of motivation throughout my studies.

This thesis would not have been possible without the contribution and support of all those mentioned above, and for that, I am truly thankful.

# **List of Figures**

1.1	Diagram of the process followed in this report	3
2.1 2.2 2.3 2.4 2.5 2.6	Basic principle of experimental modal analysis [16] Correlation between $x(t)$ at time $t$ and time $t+\tau$ [17]	7 7 9
	Accelerometers and impact hammer used during the tests Frequency Response Function with a wrong hammer tip [23]. Frequency Response Function with an adequate hammer tip [23]. three-story frame structure in the laboratory. Simplified drawing of three-story frame Masses attached to the three-story frame structure. 3D CAD model of scaled jacket. Soft neoprene pads placed below the legs Main drawings for workshop. Location and names of accelerometers in the scaled jacket structure. Masses (ferrite magnets) attached to the scaled jacket structure.	17 19 20 21 22 22 23 24
<ul><li>4.1</li><li>4.2</li></ul>	Meshing and global coordinate system of the Finite Element (FE) model of three-story frame	26 28
<ul><li>5.1</li><li>5.2</li><li>5.3</li><li>5.4</li></ul>	Parameter sensitivity chart for three-story frame structure First-frequency response surface. P4 is the natural frequency for the first mode, P21 is the Young's modulus of the rulers in first floor, and P22 is the Young's modulus of the rulers in second floor	31 34
6.1 6.2 6.3 6.4	(a) shows the Power Spectral Density (PSD) of the input. (b), (c) and (d) shows the Frequency Response Function (FRF)s and coherence of the output in 1st, 2nd and 3rd floor.  Mode shapes obtained with EMA in three-story frame structure.  Info plot for measurement channel nr. 1 of three-story frame structure.  Plots of the singular value of the Spectral Density (SD) matrices of three-	39 39 40
6.5 6.6 6.7	story frame structure	40 41 42 43
6.8	Box plots with comparison between FEM and OMA in three-story frame structure	43

6.9	Box plots with comparison between Healthy Digital Twin (HDT) and OMA	
	in three-story frame structure	44
6.10	Confusion Matrix using EMA in three-story frame structure	45
6.11	Confusion Matrix using OMA in three-story frame structure	45
6.12	Info plot for measurement channel nr. 2 of scaled jacket structure	47
6.13	Plots of the singular value of the SD matrices of scaled jacket structure	48
6.14	Mode shapes obtained with OMA in scaled jacket structure	49
6.15	Mode shapes from FE model of scaled jacket structure	50
6.16	Box plots with comparison between FEM and OMA in scaled jacket structure.	51
6.17	Box plots with comparison between HDT and OMA in scaled jacket structure.	52
	Confusion Matrix using OMA in scaled jacket structure	53
6.19	Confusion Matrix for a 2.52 kg mass using OMA in scaled jacket structure.	53
A.1	Elements of jacket dimensions	67
A.2	Node coordinates of jacket. Side A	68
	Node coordinates of jacket. Side B	
A.4	Node coordinates of jacket. Side P	70
A.5	Node coordinates of jacket. Side Q	71

# **List of Tables**

3.1	Location of the mass for different cases. The "X" represents if there is a 38g mass on the specific floor or not	20 24
4.1 4.2	Material properties of FE model of three-story frame	27 27
5.1 5.2 5.3 5.4	Parameter correlation for three-story frame structure	29 30 31
5.5	The relative frequency difference is calculated as per Equation (2.26) Relative frequency differences and $\delta_{MAC}$ values of training vectors for threestory frame structure. Relative frequency differences are calculated with	32
5.6	Equation (2.26)	32
<b>5</b> 7	with Eq. (2.26)	32
5.7	story frame structure.	32
5.8	Euclidean distances between training vectors and test vector of three-story frame structure	33
5.9	Parameter correlation for scaled jacket structure. Mode 12 is a torsional mode	33
5.11	Value range of design variables for scaled jacket structure.  Experimental design points for scaled jacket structure.  Location of the mass for different cases and its relative frequency differ-	34 35
	ence. The relative frequency difference is calculated as per Equation (2.26). Relative frequency differences and $\delta_{MAC}$ values of training vectors for scaled jacket structure. Relative frequency differences are calculated with Equa-	36
E 11	tion (2.26)	36
5.14	jacket structure	37
6.1	First three natural frequencies, damping ratio and mode shapes of three-	
6.2	story frame structure obtained using EMA	38
6.3	story frame structure obtained with OMA	41
0.0	ture obtained from FE model	41
6.4	Change in natural frequencies when considering geometric stiffness in three-story frame structure. The difference is set as $\delta_f=(f_{OFF}-f_{ON})/f_{OFF}$	42
6.5	Optimization result in three-story frame structure	44
6.6	Similarity between adjacent cases in three-story frame structure	46
6.7	Frequencies, damping ratio and mode shapes of scaled jacket structure obtained with OMA	47

6.8	Modal properties of first two bending modes, and torsional modes of the	
	jacket structure's FE model	48
6.9	Change in natural frequencies when considering geometric stiffness in scaled	
	jacket structure. The difference is set as $\delta_f = (f_{OFF} - f_{ON})/f_{OFF}$	51
6.10	Optimization result in scaled jacket structure	51
6.11	Similarity between cases in scaled jacket structure.	52

# List of Acronyms CF Correlation Function

**DOE** Design of Experiments

**DOF** Degree Of Freedom

**DDT** Damaged Digital Twin

**DT** Digital Twin

**EMA** Experimental Modal Analysis

FDD Frequency-Domain Decomposition

**FE** Finite Element

**FEM** Finite Element Method

FEMU Finite Element Model Updating

FRF Frequency Response Function

**HDT** Healthy Digital Twin

MAC Modal Assurance Criterion

**OMA** Operational Modal Analysis

**PDF** Probability Density Function

**PSD** Power Spectral Density

RNA Rotor Nacelle Assembly

SD Spectral Density

**SHM** Structural Health Monitoring

SIMO Single Input Multiple Output

**SISO** Single Input Single Output

**SSI-Cov** Covariance-Driven Stochastic Subspace Identification

SVD Singular Value Decomposition

# **Contents**

	Preface Abstract Acknowledgements List of Acronyms	. iii . iv
1	ntroduction	1
2	Theoretical Background  2.1 Experimental Modal Analysis	. 6 . 11 . 12
3	Design, setup, procedure and analysis 3.1 Equipment and software	. 18
4	Finite Element Model 4.1 Three-story Frame Structure	
5	Digital Twin and Damage Detection 5.1 Three-story Frame Structure	
6	Results 6.1 Three-story Frame Structure	
7	Discussion 7.1 Comparative assessment between EMA and OMA	. 54 . 55
8	Conclusion 3.1 Further work	<b>57</b> . 57
Re	erences	59
Α	Appendices  A.1 Equipment documentation	. 66 . 72 . 76

A.6	Confusion matrix for method using no weights	88
A.7	List of scripts and description	89

# 1 Introduction

Operation and maintenance activities have been identified as one of the leading costs in the total expenditure of wind farm projects. Operators choose to invest money on this because the consequences of a structural failure are significantly more costly. These consequences include repair expenses, decreased productivity, and the reduction of the remaining life of the asset. These failures may result from physical damage like cracks, dent, missing members, etc. or from environmental factors such as severe scour. Rapid detection of these failures can lead to substantial cost savings, and further advantages can be gained by accurately identifying the type of damage and evaluating its severity. The main purpose of this project is to investigate the benefit of using a digital twin to monitor the structure and detect possible damages.

Vibration-based damage detection is based on the principle that damage or other change to a structure will manifest itself as variations in its modal characteristics, such as natural frequencies, mode shapes, and damping ratios. A typical example is a reduction in stiffness caused by crack formation, which in turn can be observed through changes in the structure's vibration behavior [1].

Although vibration tests record both excitation and response signals as time histories, directly identifying damage from time-domain data can be quite challenging. A more widely used approach involves transforming the time-domain signals into the frequency domain through modal analysis. From there, modal parameters can be extracted, making it easier to detect and interpret damage-related changes in the system.

Structural damage detection can be carried out using either EMA — where an external force is deliberately applied — or OMA, which relies on operational loads to excite the structure. In the case of OMA, it is assumed that the excitation energy distributed across the frequency spectrum is uniform. Consequently, any irregularities observed in the response are attributed to the structural properties rather than to the input itself. Although this assumption of frequency domain uniformity is not fully valid in wind energy applications, it is often met sufficiently to allow the identification of structural modes [2].

Since the 1970s, vibration-based damage detection has evolved significantly, with a wide variety of techniques being developed. However, when applying these methods to offshore wind turbines, one must carefully consider their limitations, particularly practical challenges and high costs associated with data collection in offshore environments, which often mean that only a limited number of sensors (typically accelerometers) can be installed. Due to this small numbers of accelerometers, promising techniques like curvature-based [3] or Rayleigh quotient-based methods [4] often become impractical. As a result, any viable approach for offshore applications must function effectively with minimal sensor data.

When only a few accelerometer signals are available, damage detection relies on the ability to identify certain structural modes and compute mode-based indicators. Methods utilizing eigen-frequencies and Modal Assurance Criterion (MAC) [5] are particularly well suited.

The four key aspects of structural damage evaluation are: damage detection, localization, severity assessment, and analysis of consequences or progression [6]. In the context of offshore wind jacket structures, simply detecting that damage has occurred can already

provide significant value, as it enables inspection teams to be deployed for further investigation. Identifying the specific location of the damage improves efficiency by reducing the effort and resources required to carry out reparations. Assessing the severity of the damage offers even greater benefit, as it supports decisions about the urgency of intervention. Finally, understanding how damage might evolve or impact future operations is essential for long-term planning. The achievement of all four levels of assessment requires the integration of both direct sensing technologies and dedicated monitoring systems. In this report, Digital Twin (DT) is used in the hope of achieving at least the first two key aspects.

The concept of a DT is well-established and has seen widespread adoption across various sectors, including aerospace engineering [7] and the oil and gas industry [8]. Augustyn et al. [9] provides a model updating application study concerning the jacket substructure of an offshore wind turbine, in which the maximum eigenfrequency deviation between the experimental estimates and the predicted ones in the model is reduced from 30% to 1%.

Creating a DT typically begins with the development of a baseline model using general estimates for the physical parameters of the structure. This initial model is then refined using operational data: features are extracted from measurements and compared with the predictions of the model. Often, only a selected set of modal parameters is used for this comparison, as these can be efficiently estimated from operational data through system identification techniques.

The aim of this work is to calibrate a FE model using data obtained with EMA or OMA, allowing the model to serve as a high-fidelity digital twin. The resulting digital twin is used to simulate various damage scenarios whose modal properties are used to predict the state of the physical structure.

This work differs from other studies in the area in two ways. (1) The proposed method is validated using a lab-scale jacket structure and does not rely only on data extracted from simulated damages using FE models [10] [11]. (2) Complex neural networks have been used for damage detection in floating wind turbine structures [12] and offshore jacket structures [13], which train their model only with frequency data. In contrast, the present method proposes a simpler approach, which relies not only on frequency data but also on mode shapes.

A limitation of this work is that the mass and moment of inertia for the Rotor Nacelle Assembly (RNA) is not included, which is important for jacket foundation of wind turbines, as the modal properties are not rotationally symmetric around the tower and have a substantial effect on the mode shapes.

The approach used in this report is illustrated diagrammatically in Figure 1.1. The process begins with the creation of a baseline model, which is subsequently updated using modal properties obtained from the real structure through EMA or OMA. Various damage scenarios are then introduced into the updated model, from which selected modal properties are extracted. The same modal properties are also obtained from the real structure under the same damage condition. By comparing these modal properties using Euclidean distances, the presence and location of damage can be predicted.

In order to check the methodology and perform quality assurance on the method, the process is carried out first in a simple three-story frame structure and then in a scaled jacket foundation proposed by Ramboll.

The report begins in Chapter 2 with the background of EMA, OMA, MAC, and the concept of Digital Twin and the damage identification method. In Chapter 3, the experimental

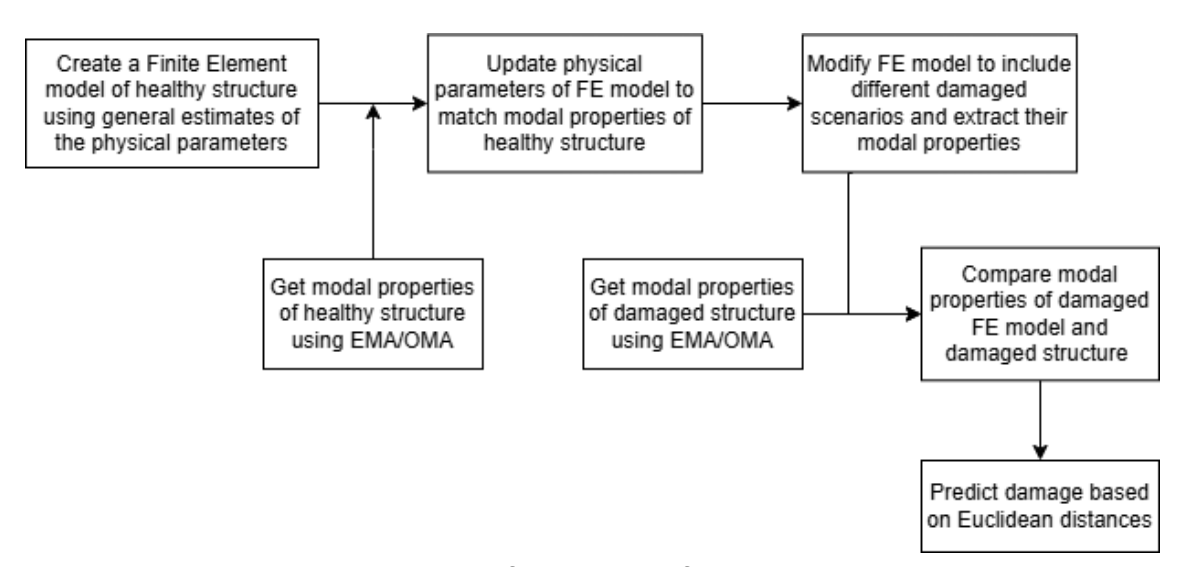


Figure 1.1: Diagram of the process followed in this report.

design, setup and procedures are presented. The test stands analyzed in Chapter 3 are implemented in numerical software in Chapter 4. Chapter 5 presents how the numerical model in Chapter 4 is updated, what the digital twin is based on, and how the damage identification method works. The results of Chapter 3, Chapter 4, and Chapter 5 are summarized in Chapter 6. Finally, a discussion is given in Chapter 7 and a conclusion is provided in Chapter 8.

# 2 Theoretical Background

To analyze vibration problems, it is essential to determine the natural frequencies, the associated mode shapes, and the corresponding modal damping of the structure under consideration. Accordingly, Section 2.1 and Section 2.2 outline the principles of two widely used methods: EMA and OMA. Furthermore, mode shapes are compared using MAC, as presented in Section 2.3. Finally, the concept of the DT and damage identification are described in Section 2.4 and Section 2.5, respectively.

## 2.1 Experimental Modal Analysis

Experimental Modal Analysis (EMA) is a widely used technique to determine the dynamic properties of structures, including natural frequencies, mode shapes, and damping ratios. This section will outline the key aspects of EMA, obtained primarily from *Introduction to Noise and Vibration Analysis* [14] and *Uncertainty in frequency response function estimates in experimental modal analysis* [15], unless otherwise noted.

In this project, it is decided to perform hammer impact tests, as is suitable for the two analyzed structures (three-story steel frame and scaled jacket). During the impact hammer test, an instrumented hammer (containing a force transducer) excites the structure and the response is measured using six accelerometers. In this way, the input (force) and the output (accelerations) are known and measured in time. In essence, a Single Input Multiple Output (SIMO) system can be interpreted as a combination of multiple Single Input Single Output (SISO) systems that share the same input but have different output locations. Therefore, the theoretical background of a SISO system is presented in this section.

For any linear SISO system, the Frequency Response Function (FRF), which relates the output response to the input force in the frequency domain, is given by

$$H(f) = \frac{Y(f)}{X(f)} \tag{2.1}$$

where:

- H(f) is the Frequency Response Function (FRF),
- Y(f) is the Fourier transform of the measured response,
- X(f) is the Fourier transform of the applied force.

The relationship between input and output is assumed to be linear, which means that doubling the input will double the output, and this allows the FRF to be independent of the size of the input force. H(f) at each frequency is a complex number and the magnitude of it is the ratio of the two amplitudes, and the phase of H(f) is the phase difference between output and input. The basic principle of EMA is shown in Figure 2.1.

However, in practice, there is always some noise present in the measuring devices and, therefore, some computation estimators must be used. In this case, H1 and H2 estimators are presented.

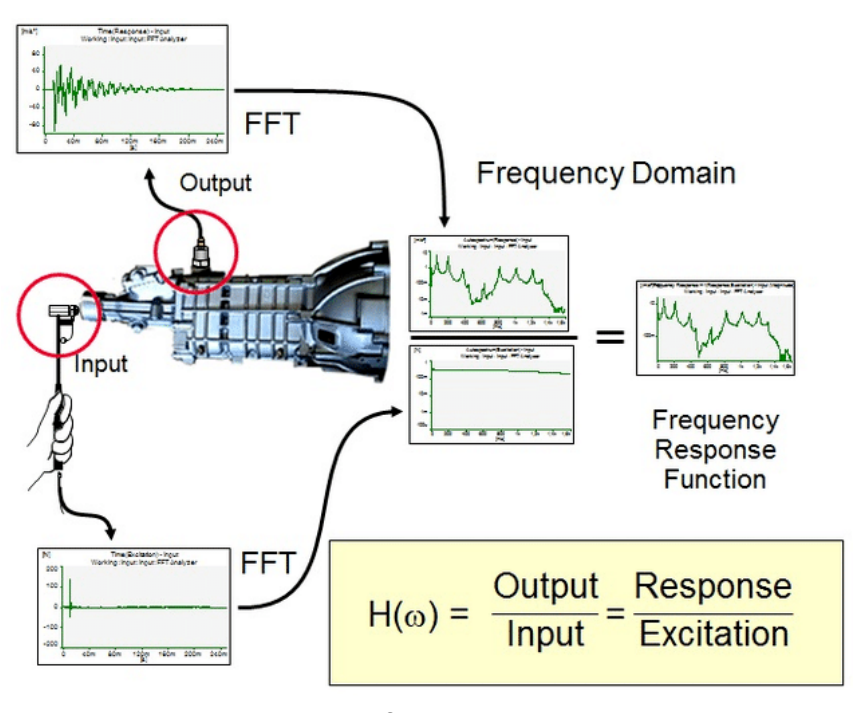


Figure 2.1: Basic principle of experimental modal analysis [16].

#### 2.1.1 H1 estimator

This method assumes that there is no noise affecting the system's input (e.g. the excitation produced with the hammer) and instead focuses on minimizing errors in the output (e.g. accelerations). This estimator is particularly useful because, in general, there is some degree of control over the force introduced into the system. In contrast, the response signal is significantly influenced by the dynamic properties of the structure. For example, at certain points and frequencies, antiresonances may occur, leading to minimal responses even when a substantial force is applied, potentially placing the response signal within the noise floor of the measurement.

However, the H1 estimator tends to underestimate the FRF at resonance points, which in turn leads to an overestimation of the damping. The H1 estimator for a SISO system is defined as

$$H_1(f) = \frac{G_{yx}(f)}{G_{xx}(f)}$$
 (2.2)

where  $G_{yx}(f)$  is the cross-spectral density between the output (y) and the input (x), and  $G_{xx}(f)$  is the auto-spectra density of the input (x). The H1 estimator represents the FRF for each output response.

#### 2.1.2 H2 estimator

The H2 estimator is less commonly used than the H1 method because the latter focuses on reducing noise in responses, and the former minimizes noise in excitation signals. However, the H2 estimator tends to overestimate the FRF at resonance, leading to an underestimation of damping. The H2 estimator for a SISO system is given by

$$H_2(f) = rac{G_{yy}(f)}{G_{xy}(f)}$$
 (2.3)

where  $G_{yy}(f)$  is the auto-spectra density of the output(y) and  $G_{xy}(f)$  is the cross-spectra density between the input(x) and the output(y). The H2 estimator represents the FRF for each output response.

#### 2.1.3 Coherence

In the construction of frequency response functions, the relationship between the output of the system (responses) and the applied input (force) is analyzed. Coherence serves as a crucial metric in this process, indicating the degree to which responses can be attributed to the applied force. Coherence values range from 0 to 1, where a value of 1 signifies that all responses are solely due to the input, while a value of 0 indicates that there is no correlation between output and input.

Poor coherence in a test can result from various factors. One common cause is a low excitation level, which allows measurement noise to significantly influence the response. Since this noise is unrelated to the applied input, it can lead to decreased coherence. A typical occurrence of this phenomenon is at anti-resonances in the FRF, where minimal system response makes measurement noise more prominent. Furthermore, if the entire response is not captured, such as when a system is impacted with a hammer, but measurement ceases while the system is still reacting, coherence will be lower due to missing data.

The coherence SISO system can be computed as

$$\gamma_{yx}^{2}(f) = \frac{|G_{yx}(f)|^{2}}{G_{xx}(f)G_{yy}(f)} = \frac{H_{1}(f)}{H_{2}(f)}$$
(2.4)

At each frequency line in the test, a specific coherence value is determined for each inputoutput pair.

## 2.2 Operational Modal Analysis

Operational Modal Analysis (OMA) involves determining the modal properties of the structure based solely on recorded vibration data from ambient excitation. These ambient responses arise from everyday operational influences, such as wind, waves, moving vehicles, or running machinery, which are generally assumed to resemble white noise.

In recent years, improvements in measurement technology and advances in computational data processing have contributed significantly to the wider adoption of OMA. This section will outline the key aspects of OMA, obtained primarily from *Introduction to Operational Modal Analysis* [17], unless otherwise noted.

#### 2.2.1 Correlation functions

Correlation is a key aspect in OMA, since correlation functions contain all the information hidden in the random response. Correlation describes the relationship between a set of variables, which can often be expressed through a simple linear model. The strength of this dependency between two variables is represented by a correlation coefficient, where ±1 indicates a perfect correlation, and 0 means that there is no correlation at all.

A variable can exhibit correlation with a time-shifted version of itself, a phenomenon known as autocorrelation, while correlation between two different signals is called cross-correlation.

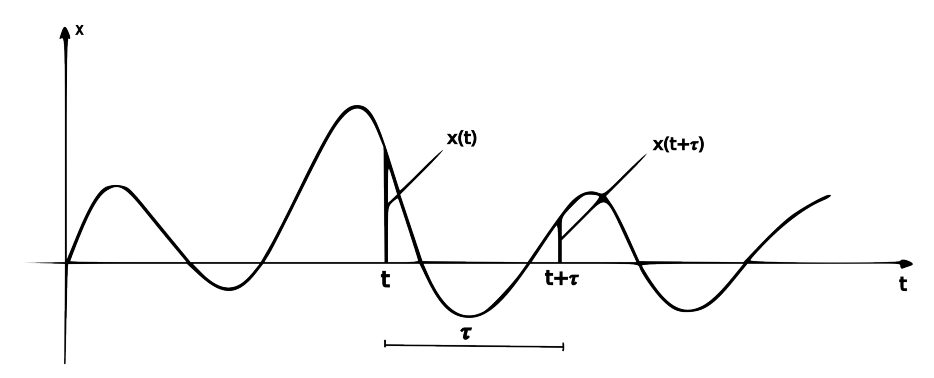


Figure 2.2: Correlation between x(t) at time t and time  $t + \tau$  [17].

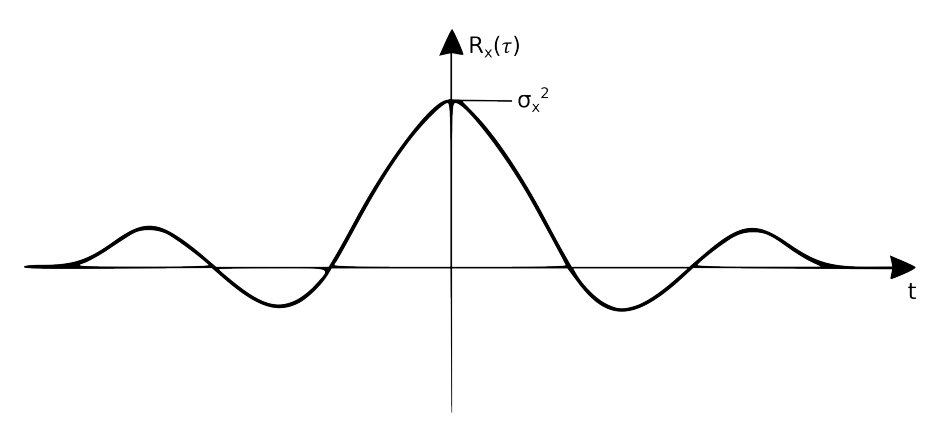


Figure 2.3: Autocorrelation function [17].

#### **Autocorrelation function**

The idea of autocorrelation is depicted in Figure 2.2, where two points x(t) and  $x(t+\tau)$  with a time separation  $\tau$  in between are considered. It is natural to think that the closer the points are (i.e.  $\tau \approx 0$ ), the higher the correlation, while the larger the separation between points, the lower the correlation. Therefore, the autocorrelation function is defined as

$$R_x(\tau) = \mathsf{E}\left[x(t)x(t+\tau)\right] = \frac{1}{T} \int_0^T x(t)x(t+\tau)dt$$
 (2.5)

where T is the duration of the signal and  $\mathsf{E}[\cdot]$  is the expectation. Furthermore, the mean of a time series in OMA does not have any meaning and should therefore be subtracted from the data set. From Equation (2.5), if the signal x(t) has zero-mean, it can be seen that for  $\tau=0$  the correlation function is equal to the variance  $\sigma_x^2$ . Moreover, if the density function is independent of time (meaning that the random signal is stationary), then all expectations do not depend on time, and the correlation function given by Equation (2.5) is also independent of time. In this way, any time shift could be introduced without changing the outcome. If the time shift  $-\tau$  is introduced, it leads to a symmetry, which is shown in Figure 2.3.

#### **Cross-correlation function**

Cross-correlation functions have the same concept as autocorrelation functions, but two different signals x(t) and y(t) are measured and the time shift  $\tau$  is applied to one of them. The cross-correlation functions can be defined as

$$R_{xy}(\tau) = \mathsf{E}[x(t)y(t+\tau)] = \mathsf{E}[x(t-\tau)y(t)] = R_{yy}(-\tau)$$
 (2.6)

$$R_{yx}(\tau) = \mathsf{E}[y(t)x(t+\tau)] = \mathsf{E}[y(t-\tau)x(t)] = R_{xy}(-\tau)$$
 (2.7)

Using the same concept as in the autocorrelation function, if the signal is stationary, the symmetry relation is obtained.

In practice, cross-correlation functions are computed using time averaging. This results in the following expressions:

$$R_{xy}(\tau) = \frac{1}{T} \int_0^T x(t)y(t+\tau)dt$$
 (2.8)

$$R_{yx}(\tau) = \frac{1}{T} \int_0^T y(t)x(t+\tau)dt$$
 (2.9)

Working with measured data, there will normally be several measurements, say N measurements, arranged in a response vector  $\mathbf{y}(t) = [y_1(t), y_2(t), ..., y_N(t)]^T$ . In this case, a matrix formulation that covers both autocorrelation and cross-correlation can be used to form the Correlation Function (CF) matrix, which is defined as

$$\mathbf{R}(\tau) = E\left[\mathbf{y}(t)\mathbf{y}^{T}(t+\tau)\right] \tag{2.10}$$

in which the diagonal elements are autocorrelation functions, and the off-diagonal elements are cross-correlation functions.

#### 2.2.2 Spectral density and Discrete Time Fourier Transform

Spectral density functions can be defined as the Fourier transform of the corresponding correlation functions, and they represent the distribution of energy as a function of frequency. In this subsection, only the core concepts of Fourier series and Transform will be presented, since they are out of the scope of this thesis.

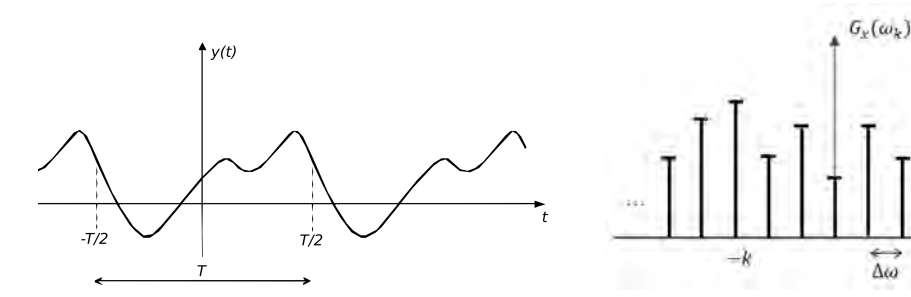
When applying the complex Fourier transform, the spectral density function for the auto-correlation function  $R_x(t)$  is expressed as

$$G_x(\omega) = \frac{1}{2\pi} \int_{-\infty}^{\infty} R_x(\tau) e^{-i\omega\tau} d\tau$$
 (2.11)

which is often referred to as the auto-spectral density function. The inverse relationship of Equation (2.11) is given by

$$R_x(\tau) = \int_{-\infty}^{\infty} G_x(\omega) e^{i\omega\tau} d\omega$$
 (2.12)

For a moment, the signal is assumed to be continuous (Figure 2.4a) and therefore the complex transform of a continuous signal in the time domain can be expressed as a discrete function in the frequency domain (Figure 2.4b). In reality, the signals obtained in OMA are discrete and, therefore, the spectral density function is not infinite. In contrast, the sampling frequency  $f_s$  and the total duration T of the recorded time-series determine



- (a) General continuous periodic function.
- (b) Discrete spectral density function of a continuous signal.

Figure 2.4: Complex Fourier Transform of a continuous signal.

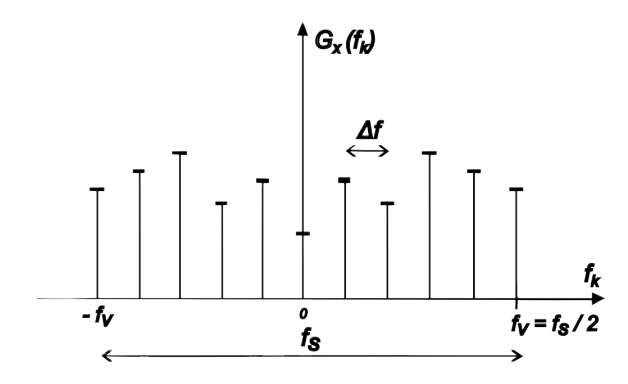


Figure 2.5: Discrete spectral density function of a discrete signal.

the frequency resolution and range of the spectral density function, as shown in Figure 2.5. The sampling frequency  $f_s$  is given by

$$f_s = \frac{1}{\Delta t} \tag{2.13}$$

where  $\Delta t$  is the sampling step. Additionally, the frequency resolution  $\Delta_f$  is defined as

$$\Delta_f = \frac{1}{T} \tag{2.14}$$

where  $T=N\,\Delta t$ , with N being the number of sample points. Moreover, since the sampling frequency  $f_s$  is placed symmetrically on the frequency axis, the spectral density function will span from  $-f_s/2$  to  $f_s/2$ , which defines the Nyquist frequency, which is given by

$$f_v = \frac{f_s}{2} \tag{2.15}$$

#### 2.2.3 Frequency Domain Decomposition

The objective of the Frequency-Domain Decomposition (FDD) technique is to obtain modal properties based on Singular Value Decomposition (SVD) of the Spectral Density (SD) matrix.

Any response y(t) can be expressed in terms of normal modes and modal coordinates, that is,

$$\mathbf{y}(t) = \mathbf{a}_1 q_1(t) + \mathbf{a}_2 q_2(t) + \dots = \mathbf{Aq}(t)$$
 (2.16)

where **A** is the mode shape matrix  $\mathbf{A} = [\mathbf{a}_1, \mathbf{a}_2, ...]$  and  $\mathbf{q}(t)$  is a column vector of modal coordinates  $\mathbf{q}^T(t) = \{q_1(t), q_2(t), ...\}$ .

Based on the definition of the CF matrix in Equation (2.10), the response can be expressed as

$$\mathbf{R}_{y}(\tau) = \mathbf{E} \left[ \mathbf{y}(t) \mathbf{y}^{T}(t+\tau) \right]$$

$$= \mathbf{A} \mathbf{E} \left[ \mathbf{q}(t) \mathbf{q}^{T}(t+\tau) \right] \mathbf{A}^{T}$$

$$= \mathbf{A} \mathbf{R}_{q}(\tau) \mathbf{A}^{T}$$
(2.17)

where  $\mathbf{R}_q(\tau)$  is the CF matrix of modal coordinates. Taking the Fourier transform of both sides of Equation (2.17), the corresponding SD matrix is obtained:

$$\mathbf{G}_{v}(f) = \mathbf{A}\mathbf{G}_{q}(f)\mathbf{A}^{T} \tag{2.18}$$

Since the modal coordinates are uncorrelated (and therefore the off-diagonal elements of the CF matrix are zero), then the SD matrix  $\mathbf{G}_q(f)$  of the modal coordinate is both diagonal and positive valued. The SD matrix, being Hermitian and associated with possibly complex mode shapes, requires the Hermitian operation instead of a simple transpose, resulting in

$$\mathbf{G}_y(f) = \mathbf{A} \left[ g_n^2(f) \right] \mathbf{A}^H$$
 (2.19)

where diagonal terms  $\left[g_n^2(f)\right]$  represent auto-spectral densities. Applying SVD to the SD matrix, an approximate representation emerges as

$$\mathbf{G}_y(f) = \mathbf{U}\mathbf{S}\mathbf{U}^H = \mathbf{U}\left[s_n^2(f)\right]\mathbf{U}^H \tag{2.20}$$

where singular values  $\left[s_n^2(f)\right]$  align with auto-spectral densities of the modal coordinates, and singular vectors in **U** represent mode shapes. The resulting decomposition deviates from the theoretical SVD due to biases, and consequently FDD solutions are approximate.

It is important to note that the SVD always force the singular vectors to be orthogonal, whereas in structural dynamics the mode shapes are not geometrically orthogonal but orthogonal with respect to the mass matrix. As shown in Figure 2.6, the mode shape should be estimated when the forced orthogonality has the least effect, i.e. for frequencies where the corresponding singular value dominates.

#### 2.2.4 Covariance-Driven Stochastic Subspace Identification

This subsection presents the key aspects of Covariance-Driven Stochastic Subspace Identification (SSI-Cov) [18]. The CF matrix  $\mathbf{R}(\tau)$  was previously defined in Equation (2.10), which is used by the SSI-Cov when building the block-Hankel matrix  $\mathbf{H}_i$ , which is defined as

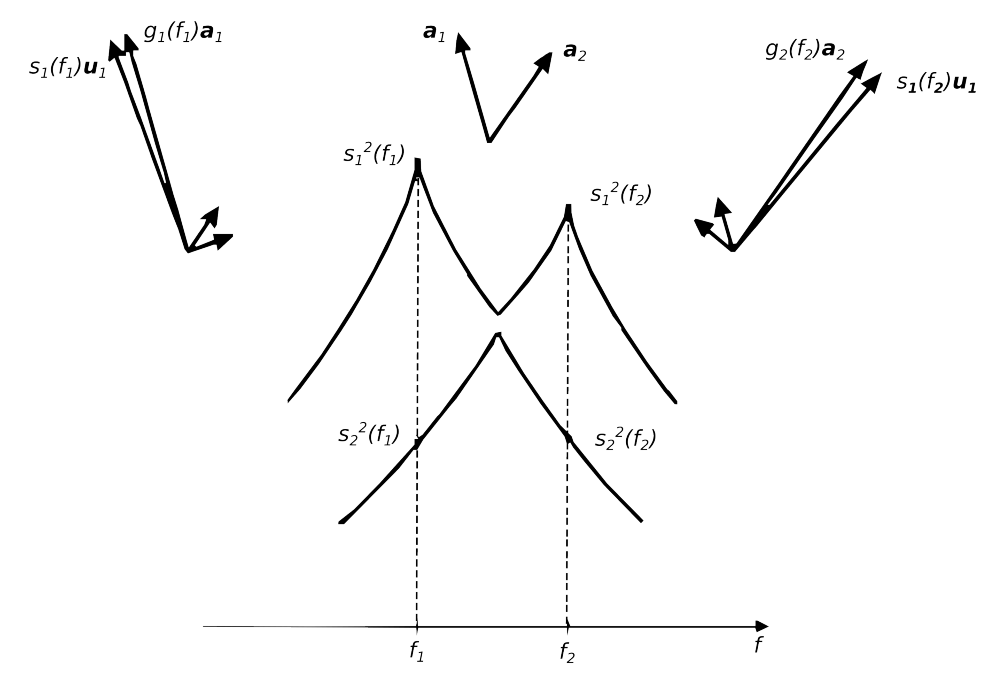


Figure 2.6: Bias from forcing the singular vector to geometrical orthogonality [17].

$$\mathbf{H}_{i} = \begin{bmatrix} \mathbf{R}_{1} & \mathbf{R}_{2} & \cdots & \mathbf{R}_{i} \\ \mathbf{R}_{2} & \mathbf{R}_{3} & \cdots & \mathbf{R}_{i+1} \\ \vdots & \vdots & \ddots & \vdots \\ \mathbf{R}_{i} & \mathbf{R}_{i+1} & \cdots & \mathbf{R}_{2i+1} \end{bmatrix}$$
(2.21)

The block-Hankel matrix  $\mathbf{H}_i$  contains submatrices which are consistent with the different correlation matrices between all measurement channels. 2i corresponds to the maximum number of time lags and i is the number of block rows.

The block-Hankel matrix can be deconstructed into observability matrix  $\mathcal{O}_i$  and controllability matrix  $\mathcal{C}_i$ , which are defined by

$$\mathscr{O}_i = egin{bmatrix} \mathbf{C} \\ \mathbf{C} \mathbf{A} \\ \mathbf{C} \mathbf{A}^2 \\ \vdots \\ \mathbf{C} \mathbf{A}^{i-1} \end{bmatrix} \qquad \mathscr{C}_i = \left[ \mathbf{G} \quad \mathbf{A} \mathbf{G} \quad \cdots \quad \mathbf{A}^{i-1} \mathbf{G} \right] \qquad (2.22)$$

Where the matrices **A** and **C** refer to the discrete state matrix and discrete output matrix, respectively, and matrix **G** contains the stochastic state space model describing the problem.

Further analysis of  $\mathcal{O}_i$  will lead to eigenvalue decomposition of **A** and hereby the eigenvalues and eigenvectors of the system (i.e. modal properties) can be estimated.

#### 2.3 Modal Assurance Criterion

Comparing natural frequencies and damping ratios is a straightforward procedure because the comparison is made between single values. If the difference between two

values is less than a certain threshold value (usually defined by self-experience or standards), then the result is considered satisfactory. However, when comparing mode shapes there are many Degree Of Freedom (DOF)s and therefore a correlation measure should be used.

In this case, the Modal Assurance Criterion (MAC) [17] can be used to compare the experimental mode shape vectors **A** obtained through EMA or OMA, with the mode shape vectors obtained from the FE model **B**. The MAC matrix is defined as

$$\mathbf{MAC} = \frac{\left(\mathbf{A}^{H}\mathbf{B}\right)^{2}}{\left(\mathbf{A}^{H}\mathbf{A}\right)\left(\mathbf{B}^{H}\mathbf{B}\right)}$$
(2.23)

The MAC values will vary between zero and unity. When there is a strong correlation between the FE model and the experimental data, particularly in mode shapes, the MAC values will be close to one. It is important to note that **A** and **B** should be composed only of the same DOFs.

## 2.4 Digital Twin

Creating a digital twin typically begins with the development of a baseline model using general estimates of the physical parameters of the structure. This initial model is then refined using operational data: features are extracted from measurements and compared against the predictions of the model. Often, only a selected set of modal parameters is used for this comparison. If the baseline model does not match the modal parameters extracted from operational data, an update to the baseline model is required.

Typically, the first step towards digital twin is identifying which parameters have the most influence on the modal properties. Sensitivity-based methods can be used to select a set of physical parameters of the model to better reflect the in-situ conditions. The sensitivity analysis is explained in Subsection 2.4.1

Once the most sensitivity parameters are identified, optimization techniques can be used to minimize the difference between experimental and numerical modal parameters. The optimization process is described in Subsection 2.4.2.

#### 2.4.1 Sensitivity analysis

Sensitivity analysis shows how different values of an independent variable affect a dependent variable under a given set of assumptions. In this thesis, sensitivity represents the change in a modal parameter (e.g., natural frequency  $f_i$ ) due to a small change in a model parameter ( $p_i$ ), that is,

$$S_{ij} = \frac{\partial f_i}{\partial p_j} \tag{2.24}$$

A higher value of  $S_{ij}$  means that the parameter  $p_j$  significantly affects mode i. It is common practice to normalize the sensitivity values in order to compare parameters of different units and magnitudes. Normalized sensitivity is defined as

$$\bar{S}_{ij} = \frac{S_{ij}p_j}{f_i} \tag{2.25}$$

Sensitivity analysis is used to perform parameter correlation, allowing the identification of which input parameters have the greatest and least impact on the design, as well as the degree to which their relationships are linear or non-linear. ANSYS DesignXplorer supports both Pearson's linear correlation method [19] and Spearman's rank correlation method [20].

#### 2.4.2 Optimization process

This section will outline the key aspects of the optimization process performed with AN-SYS, which is obtained primarily from *DesignXplorer Optimization Tutorials* [21], unless otherwise noted. First, design of experiments are generated which are subsequently used to build a set of response surfaces. These surrogate models are then used to optimize the response surface with the goal of minimizing the difference between the numerical and experimental modal parameters.

#### **Design of Experiments**

Design of Experiments (DOE) is a technique used by ANSYS, which strategically selects sampling points that maximize the efficiency of exploring the space of random input parameters, ensuring that the necessary information is gathered with as few samples as possible.

ANSYS include many methods to generate experimental design points, for example Central Composite Design, Optimal Space-Filling Design, Box-Behnken Design, etc. More information about it can be found in [21].

#### **Response Surface**

Once the DOE are identified, continuous response surface can be fit to them. Thus, response surfaces can obtain an approximation of the target output variable or parameter at any point without performing a complete solution process. ANSYS DesignXplorer provides several response surfaces types, such as Genetic Aggregation, Full 2nd Order Polynomials, Non-Parametric Regression, Neural Network, etc.

The Genetic Aggregation type solves an iterative genetic algorithm, which aims to find the best response level for each output parameter. The main goal is to achieve the following three main criteria to obtain the best response level:

- High compliance with design points (DOE points)
- · Appropriate cross-validation
- Smoothness (similar to a linear mode)

An example of response Surface optimization can be found in Subsection 5.1.3

#### **Response Surface Optimization**

Response Surface Optimization system obtains its information from its own Response Surface cell (described above). Therefore, its performance depends on the quality of the response surface. ANSYS DesignXplorer use response surface evaluations (such as, Screening, MOGA, NLPQL, and MISQP) rather than real solves.

In order to build a Digital Twin, an appropriate number of natural frequencies are set as optimization objectives. Therefore, a multi-objective optimization design is required, where there is not an absolute optimal solution, but a series of relatively optimal solution sets, namely Pareto solution sets.

The genetic algorithm has strong global optimization ability and is an effective method to solve the multi-objective optimization problem of target conflict. NSGA-II is one of the most widely used genetic algorithms. This method introduces the crowding ranking

criterion and stratifies the population individuals according to the dominant relationship between individuals before the selection operator is executed [22].

It is important to note that there is no good or bad solution; therefore, the designer needs to find the most suitable solution according to his knowledge, judgement and experience.

## 2.5 Damage Identification

The presence of any damage in a structural member might affect the modal properties of the whole structure (i.e. natural frequencies, mode shapes, and/or damping ratios). Detection of damage is performed as follows.

If the Healthy Digital Twin (HDT) is assumed to closely represent the real structure, it can be used to simulate different damage scenarios-varying in both type and severity)-referred to as Damaged Digital Twin (DDT). For each damaged configuration (DDT), the modal properties (i.e., natural frequencies and mode shapes) are extracted and compared to those of the HDT. This comparison is performed using the relative frequency differences and the modal assurance criterion (MAC), which was previously defined in Equation (2.23). The relative frequency difference is defined as

$$\delta_f = \frac{f_{HDT} - f_{DDT}}{f_{HDT}} \tag{2.26}$$

Where  $f_{HDT}$  is the natural frequency of interest of the HDT, whereas  $f_{DDT}$  is the natural frequency of interest of the various DDT. Each damage scenario generates a "training" vector  $\mathbf{x}$ , which is given by

$$\mathbf{x} = [\delta_{f1}, \delta_{f2}, \delta_{f3}, \delta_{MAC1}, \delta_{MAC2}, \delta_{MAC3}]$$
(2.27)

where  $\delta_{MAC}$  is defined as

$$\delta_{MAC} = 1 - MAC \tag{2.28}$$

It is important to note that the "training" vector  $\mathbf{x}$  in Equation (2.27) contains values of  $\delta_f$  and  $\delta_{MAC}$  for all modes of interest (in this case, there are 3 modes of interest for both the three-story frame structure and the scaled jacket). The construction of these vectors forms the "training phase" of the classifier.

In the "test phase", the modal properties of the physical structure (whose damage state is unknown) are obtained experimentally using, for example, OMA. These are compared to the HDT using the same metrics, producing a test vector  $\hat{\mathbf{x}}$ .

Since there are different uncertainties in the identification of the modes, weights are used when computing Euclidean distances. Weights are calculated as

$$\mathbf{w} = \frac{1}{\mathbf{c}\mathbf{v}} \tag{2.29}$$

where **cv** is a vector with the coefficients of variation, which, for three modes of interest, is defined as

$$\mathbf{cv} = \begin{bmatrix} \sigma_{\delta_{f1}}, \frac{\sigma_{\delta_{f2}}}{\mu_{\delta_{f1}}}, \frac{\sigma_{\delta_{f3}}}{\mu_{\delta_{f2}}}, \frac{\sigma_{\delta_{MAC1}}}{\mu_{\delta_{MAC1}}}, \frac{\sigma_{\delta_{MAC2}}}{\mu_{\delta_{MAC2}}}, \frac{\sigma_{\delta_{MAC3}}}{\mu_{\delta_{MAC3}}} \end{bmatrix}$$
(2.30)

where  $\sigma_{\delta_f}$  is the standard deviation of the relative frequency difference for each mode,  $\sigma_{\delta_{MAC}}$  is the standard deviation of  $\delta_{MAC}$  for each mode,  $\mu_{\delta_f}$  is the mean relative frequency difference for each mode and  $\mu_{\delta_{MAC}}$  is the mean of  $\delta_{MAC}$  for each mode. It is important to note that the weights are computed based only on the tests without any damage.

Thus, the Euclidean distance between the test vector  $\hat{\mathbf{x}}$  and each training vector  $\mathbf{x}$  is calculated as

$$d = \sqrt{\sum_{i=1}^{6} w_i (x_i - \hat{x}_i)^2}$$
 (2.31)

Finally, the predicted damage case corresponds to the scenario with the smallest distance. The approach using weights prevents unreliable modes from dominating the distance calculation.

# 3 Design, setup, procedure and analysis

In this chapter, experimental analysis and test setup for both the three-story frame structure and the scaled jacket structure are presented. Furthermore, the design and construction of the scaled jacket is described.

## 3.1 Equipment and software

This section presents a description of the equipment and software used during the tests.

#### **Accelerometers**

Accelerometers are used to detect and record the accelerations that a structure undergoes at a specific mounting point. In this study, the accelerometer is fixed to the structure with wax. The model used is the Brüel & Kjær 4507-B, with detailed product specifications provided in Subsection A.1.1.

To ensure that data quality is not compromised by noise, it is essential to carefully select the location of the accelerometer, avoiding nodal points where vibrational amplitudes are minimal. One of the accelerometers attached to the three-story frame structure is illustrated in Figure 3.1a.

The accelerometer operates on the basis of the piezoelectric effect. As the device experiences accelerations, the inertia causes the mass inside to resist motion, leading to compression or stretching of a spring. This motion generates a force on the piezoelectric crystals, which produces an electrical charge proportional to the acceleration. This charge is then measured and converted into acceleration values.

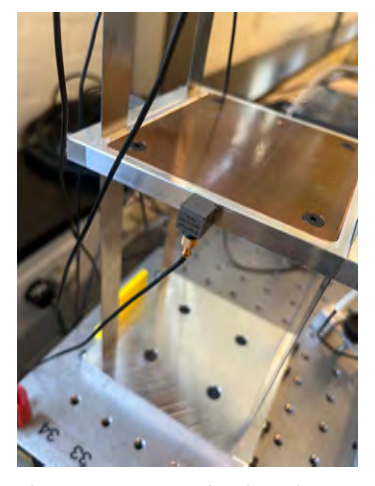
When attaching accelerometers, there are challenges in choosing the right mounting location and ensuring a secure attachment to the test setup. It is important to avoid placing them near nodal points to prevent the collection of weak vibrational data. Moreover, the attachment method must provide a stable connection without interfering with the measurements. In this case, wax is used as adhesive, and a thin layer ensures enough stiffness to prevent the accelerometer structure from affecting the recorded data. Furthermore, coaxial cables attached to accelerometers should not touch the structure, as this could lead to incorrect estimation of the modal parameters.

The accelerometers are connected via cable to an NI-cDAQ-9171 that collects data and transfers them to a laptop via USB.

#### Impact hammer

For this project, an impact hammer (Brüel & Kjær 8206 model) is used, as shown in Figure 3.1b. Detailed product specifications are provided in Subsection A.1.2. The impact hammer works by applying a single impact to the structure when it is stationary. The technique is widely used and recognized in the industry and is preferred in this project because the scaled jacket structure cannot be excited with a shaker or shake table. Therefore, the impact hammer is the preferred method in this case.

The impact hammer set-up includes a force transducer, and the frequency range achievable with the impact hammer depends on the hardness of hammer tip used in the experiment. A harder tip will result in a broader excitation frequency range. To ensure that all modes of interest are excited within the desired frequency range, the appropriate tip must be chosen. If a tip that is too soft is used, it will fail to adequately excite all modes, leading







(b) Impact hammer.

Figure 3.1: Accelerometers and impact hammer used during the tests

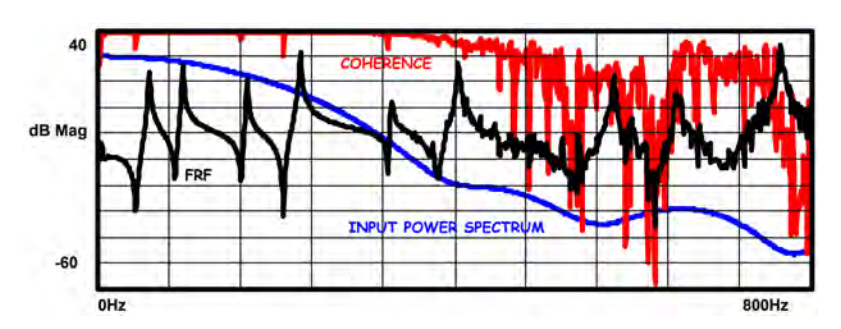


Figure 3.2: Frequency Response Function with a wrong hammer tip [23].

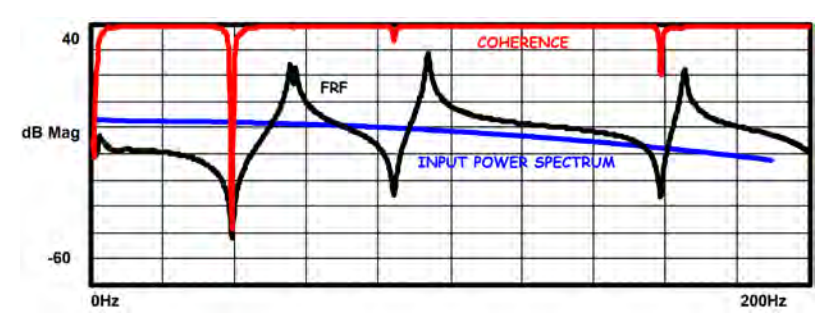


Figure 3.3: Frequency Response Function with an adequate hammer tip [23].

to poor measurement quality. This can be observed in Figure 3.2, where the power spectrum does not excite the full frequency range. Due to this, the coherence and frequency response function degrade across the latter half of the frequency range.

A good impact test typically aims to produce a relatively flat and well-distributed input excitation force. When the correct hammer tip is chosen, the frequency response function improves significantly, as reflected by an enhanced coherence function (Figure 3.3). Selecting the appropriate tip is therefore vital to ensure all relevant modes are excited and the frequency response measurement is reliable.

Although the magnitude of the impact is not critical for frequency analysis, it must be sufficient to achieve an adequate signal-to-noise ratio without inducing significant nonlinear

behavior in the structure. Consistency in the placement and orientation of the impacts is vital, and care must be taken to avoid double unintentional impacts, since it would modify the free response of the structure.

Another important consideration in impact testing is the use of a proper impact window. For lightly damped structures (such as the three-story frame structure), the response to the impact will not naturally decay to zero within the measurement interval. This incomplete decay results in a digital signal processing issue known as leakage. To mitigate leakage, a window is applied to the data, which ensures that the data aligns more closely with the periodicity requirements of the methods, thus reducing the distortions caused by leakage. The most commonly used window for impact excitation measurements is the exponentially decaying window.

While windows help reduce leakage, they can also introduce some distortion into the data, i.e. artificial damping. To account for this effect, a corrected damping ratio can be obtained by incorporating the time constant of the applied exponential window, as described in [24]:

$$\zeta_{cor} = \zeta - \frac{1}{\tau_w \omega_n} \tag{3.1}$$

where  $\zeta$  is the artificial damping ratio due to the exponential window,  $\omega_n$  is the natural angular frequency of the mode, and  $\tau_w$  is the time constant, which defined as

$$\tau_w = -\frac{T}{\ln(x)} \tag{3.2}$$

where T is the period (length of the window) and x is the decay of its amplitude within the capture duration.

#### **Data Logging Software and Data Processing**

Data processing is carried out in Python. The data obtained with FlexLogger are saved in "tdms" format, which is read with a custom function called "read\_TDMS\_Modified". For more information, see Section A.7. In EMA, the auto-spectral and cross-spectral density functions are obtained by Welch's method included in SciPy [25], and the poles are computed using the Least-Squares Complex frequency domain method (LSCF) included in SDyPy [26]. For more information, please refer to the script "EMA-Hammer-3story" in Section A.7. On the other hand, pyOMA2 is used in the OMA-tests, as it is an open source Python module [27]. The Complex Mode Indicator Function (CMIF) is used to identify modes in the frequency domain data using the results from FDD. Modal parameters are extracted using Covariance-driven Stochastic Subspace Identification (SSI-Cov), in which stability diagrams are plotted. The stability diagram helps visualize the stability of identified poles across different model orders, making it easier to separate physical poles from spurious ones. For more information, please refer to the script "OMA\_3story" or "OMA\_Jacket" in Section A.7. A description of all the scripts used in the project can be seen in Section A.7.

# 3.2 Three-story Frame Structure

An experimental test with a three-story frame structure was used to test modal parameter estimation methods (i.e. EMA and OMA). Figure 3.4 shows the structure in the laboratory and Figure 3.5 shows a simplified drawing, in which the floors are rectangular (110 x 124 x 10) mm, constructed from aluminum with copper plates of 2 mm thick at the top and bottom. The mass of each floor is 0.48 kg and the columns are made of four steel rulers



Figure 3.4: three-story frame structure in the laboratory.

that are fixed to each floor and their dimensions are  $(150 \times 18 \times 0.5)$  mm. Moreover, the structure has a base plate that is attached to an optical table using 4 screws. Therefore, it is considered that the structure is fully fixed to the optical table.

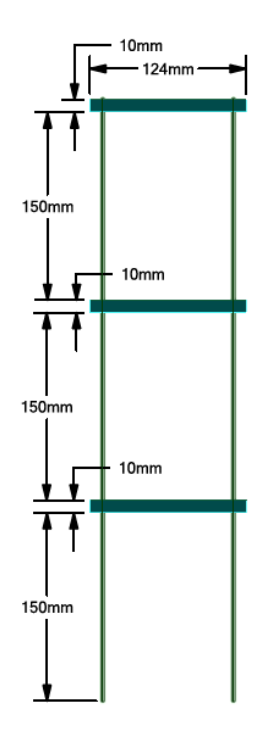
There are 6 accelerometers placed at the floor levels (two accelerometers on each floor), which are described in Section 3.1. There are 3 accelerometers in the longitudinal direction (less stiff direction) and 3 accelerometers in the transverse direction (stiffer direction).

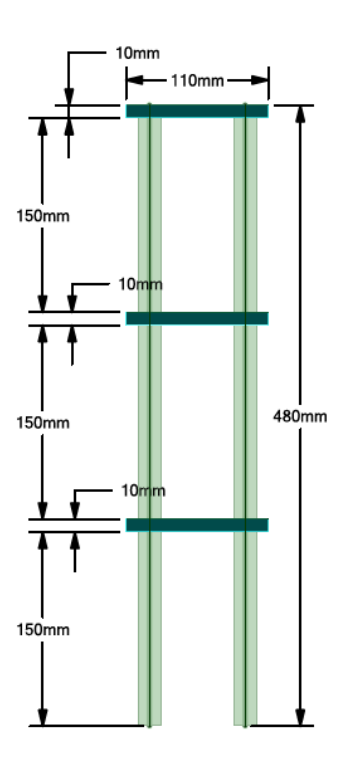
An impact hammer with a rubber tip is used to excite the structure, which is described in Section 3.1. For EMA, the structure is hit in a single location approximately every 20 seconds for 3 minutes. Then, this procedure is repeated for every floor in both directions. On the other hand, for OMA, the structure is randomly hit for 8 minutes, with the objective of simulating a random input which should be able to excite all modes of interest. In both cases, the sampling frequency  $f_s$  is set to 1066 Hz.

Additionally, before the actual identification is performed with OMA, signal processing techniques are used, including decimation, filtering, and construction of the SD matrix. It is recommended that the natural frequencies of the modes of interest lay within 10%-90% of the Nyquist frequency. In this case, since the frequencies of interest range from 1 Hz to 10 Hz, the signals are decimated by a factor of 32, and thus the Nyquist frequency  $f_v$  is reduced from 533 Hz to 16.6 Hz. The SD matrix is estimated by using Periodogram method with 50% overlap, and the number of data points in each segment is set to N = 2048.

#### 3.2.1 Damages

The different "damages" are represented by a set of extra masses whose mass is 38 grams and which are attached to the structure at different locations. 38 grams represents 8% of the floor's weight. Table 3.1 summarizes the different cases and locations, while Cases 1 and 5 are illustrated in Figure 3.6.





- (a) Longitudinal (less stiff) direction.
- (b) Transverse (stiffer) direction.

Figure 3.5: Simplified drawing of three-story frame

		Case 1	Case 2	Case 3	Case 4	Case 5	Case 6	Case 7
Location	1st floor	Х			Χ	Х		X
Location	2nd floor		Χ		Χ		Χ	Χ
of the mass	3rd floor			Χ		Χ	Χ	Χ

Table 3.1: Location of the mass for different cases. The "X" represents if there is a 38g mass on the specific floor or not.

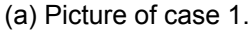
### 3.3 Scaled Jacket Structure

The jacket foundation of a 20 MW wind turbine proposed by Ramboll is fully described in [28], while Appendix A.2 contains the information used to design the scaled jacket structure. Considering that the structure has to fit in a cold chamber that is going to be built in the future, it is decided to scale it down to 1:50.

Steel jacket foundations are large, complex structures that need to be both strong and cost-effective, and since steel is a relatively expensive material, it makes sense to optimize its usage to ensure the structure is as efficient as possible. On the other hand, it is not feasible for the workshop to have a lot of different cross-sections that change several times on a single element. Therefore, the scaled jacket structure has been simplified by considering only two cross-sections: steel precision tubes of 50x1,5mm for the legs and steel precision tubes 12,7x1mm for the braces. Additionally, the transition piece has been simplified as a solid steel plate with cross-section 15x160mm.

A 3D CAD model is presented in Figure 3.7, while the manufactured scaled jacket is visualized in Figure 3.10. The fabrication of the mock-up is carried out at DTU Construct's workshop by Johnny Sølvtorp and under the leadership of Jan Frank Pedersen. A 5-mm







(b) Picture of case 5.

Figure 3.6: Masses attached to the three-story frame structure.

thick steel base plate is used to restrain deformations in X and Y directions, and 4 pads made of solid soft neoprene are placed below the legs, as shown in Figure 3.8. Each pad is  $(100 \times 100 \times 7)$ mm. The drawings are summarized in Figure 3.9, and the complete set of drawings is available in Section A.3. It is important to note that the steel base plate is not shown in the drawings.

Since one of the modes of interest is the torsional mode, it is important to capture the accelerations in the upper part of the legs. However, the transition piece has plane faces, where it is easier to attach an accelerometer (and the location is still close enough to the leg). Therefore, there are 4 accelerometers placed in the transition piece. Additionally, there are 2 accelerometers placed in the legs at approximately half height of the structure, in order to capture the first-order bending modes. The location and names of the accelerometers are shown in Figure 3.10.

On the same basis as in the three-story frame structure, an impact hammer with a rubber tip is used to excite the structure. For OMA, the structure is randomly hit for 3 minutes, generating a fairly random input. The sampling frequency  $f_s$  is set to 1066 Hz.

For the scaled jacket, the frequencies of interest range from 10 to 200 Hz. Since there is no single decimation factor that covers this range appropriately, a factor of 2 is chosen as a compromise. Thus, the Nyquist frequency  $f_v$  is reduced from 533 Hz to 266.5 Hz. The SD matrix is estimated by using Periodogram method with 50% overlap, and the number of data points in each segment is set to N =2048. More information about the script can be found in  $OMA\_Jacket$  in Section A.7.

#### 3.3.1 Damages

In [29], Ramboll provides a general overview of common structural failures modes of offshore structures on the Norwegian Continental Shelf. It is observed that 90% of the reported incidents are classified by steel, in which 85% occur on jackets. Therefore, it is noted that offshore jacket foundations are prone to suffer damage. However, there are some damages that have a low probability of prediction, such as cracking (through

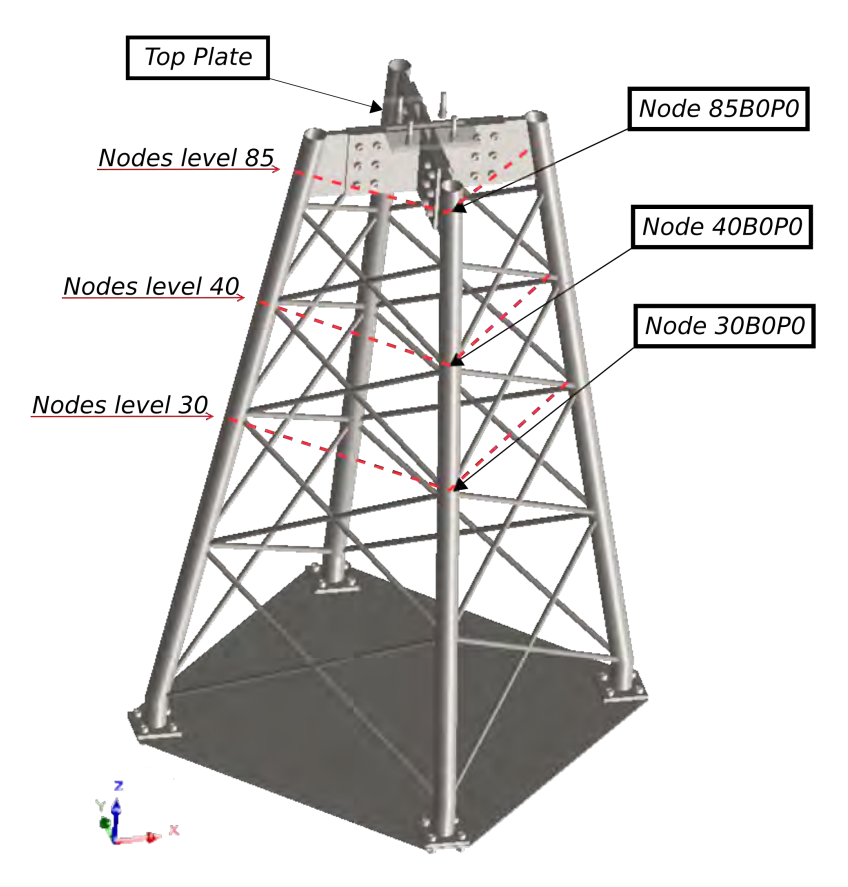


Figure 3.7: 3D CAD model of scaled jacket.



Figure 3.8: Soft neoprene pads placed below the legs

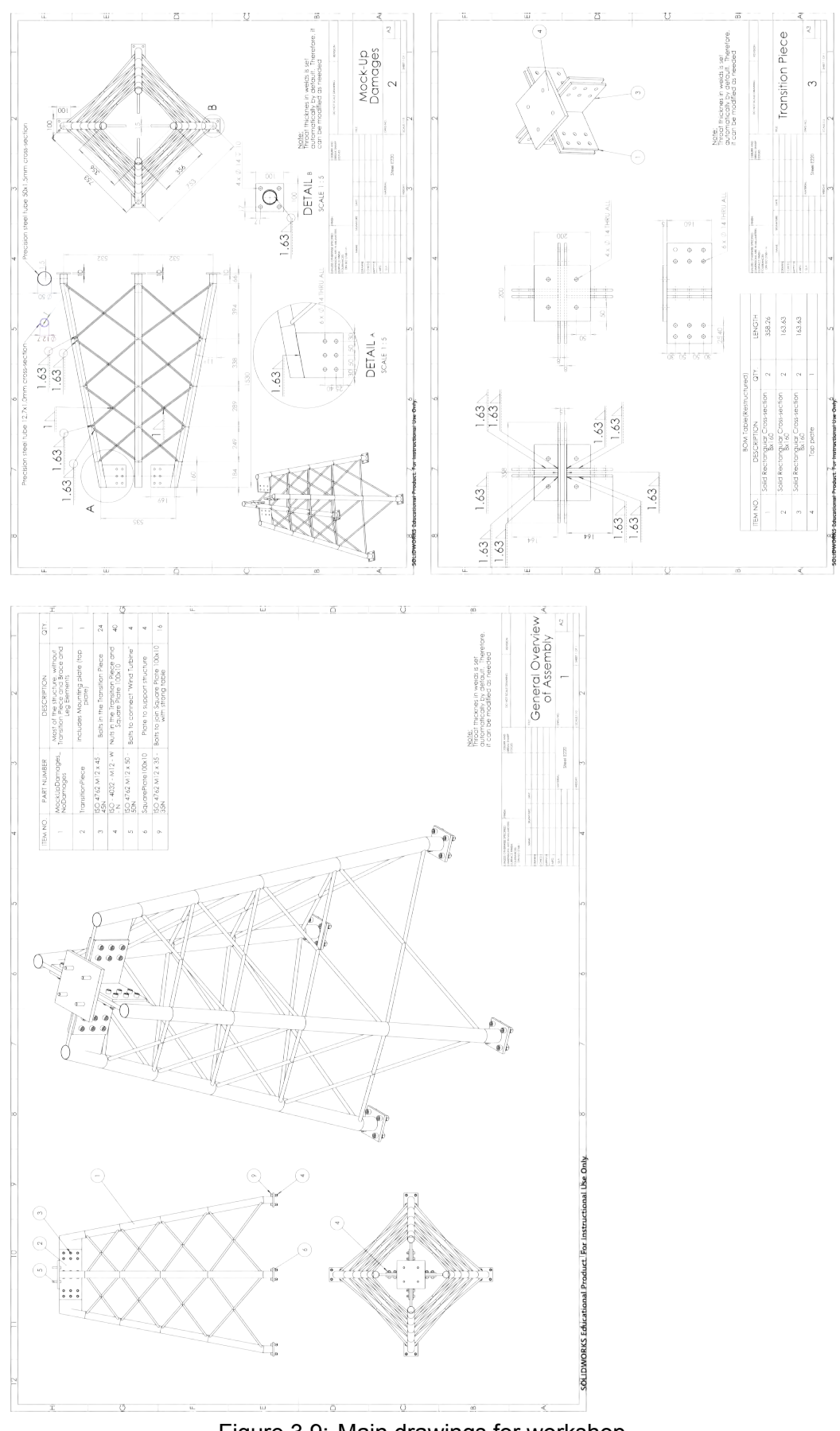
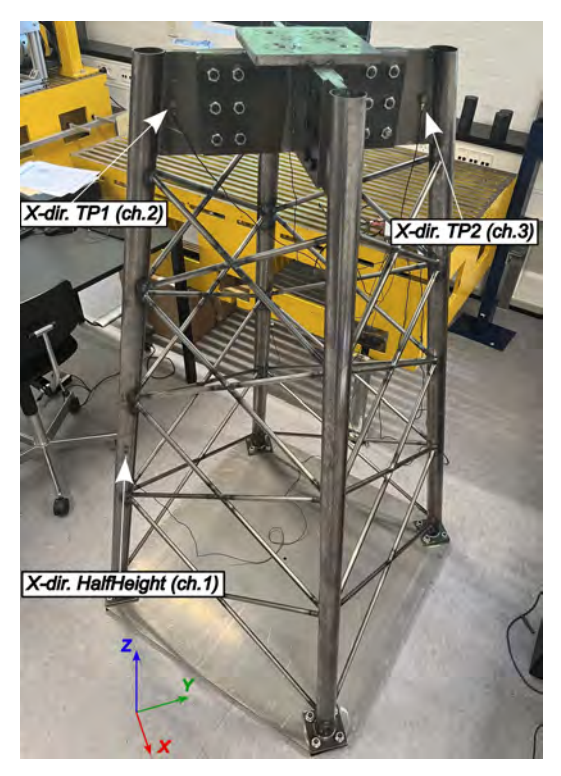
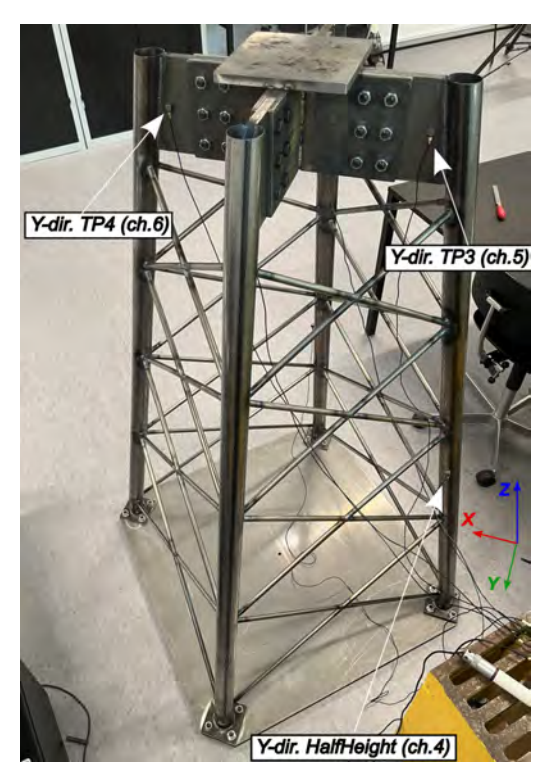


Figure 3.9: Main drawings for workshop.





(a) X-direction.

(b) Y-direction.

Figure 3.10: Location and names of accelerometers in the scaled jacket structure.

		Case 1	Case 2	Case 3	Case 4	Case 5	Case 6	Case 7
	Top Plate	6.72 kg						
	Nodes level 30		5.04 kg					
Location	Nodes level 40			5.04 kg				
Location	Nodes level 85				5.04 kg			
of magnets	Node 30B0P0				_	5.04 kg		
	Node 40B0P0						5.04 kg	
	Node 85B0P0							5.04 kg

Table 3.2: Extra masses (ferrite magnets) added to the scaled jacket structure.

thickness), and dents and bows. Missing members and scour in the foundation have a medium-to-high probability of prediction, and therefore, they could be investigated in future work.

Due to time constraints, only extra masses are added at different locations in the jacket structure. Following the same concept as in the three-story frame structure, ferrite magnets are used, whose mass is 210 grams, and they are packed together to get larger masses. Figure 3.7 shows the names and locations of the nodes where the masses are attached. Table 3.2 summarizes the different cases in which, for example, "Nodes level 30" means that 5.04 kg are distributed in all the nodes at level 30 (i.e. 1.26 kg on each node). On the other hand, for example "30B0P0" means that 5.04 kg are concentrated in that single node. 5.04 kilograms represents 10.4% of the total weight of the structure. Cases 1,2 and 5 are illustrated in Figure 3.11.

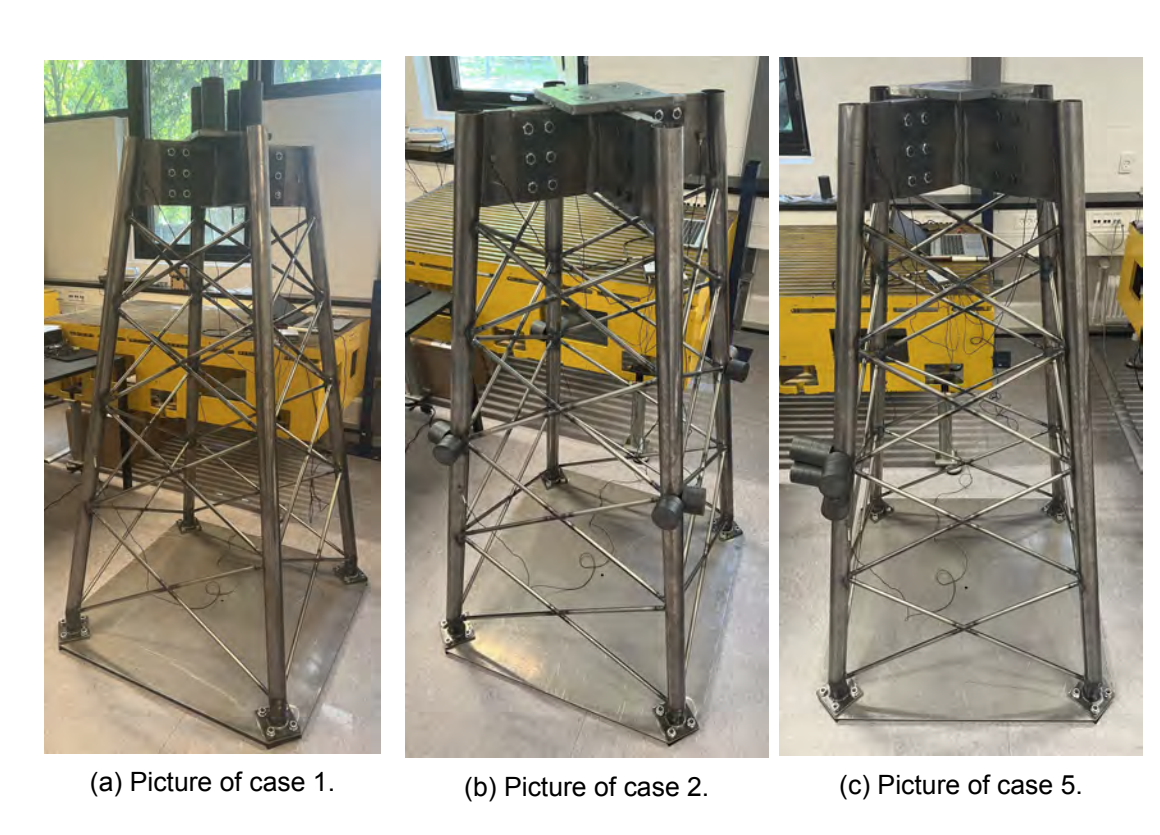


Figure 3.11: Masses (ferrite magnets) attached to the scaled jacket structure.

# 4 Finite Element Model

Finite element models are performed to obtain knowledge about the dynamic properties of the experimental model presented in Chapter 3. FE results can be compared with EMA and OMA to validate the numerical model and, if discrepancies exist, Finite Element Model Updating (FEMU) using experimental data can be performed to improve its accuracy. Then, a validated FE model can be used to detect structural changes or damage by comparing the measured modal parameters over time. Additionally, FE models help determine the best location for excitation with the impact hammer and where the accelerometers should be placed. Thus, the efficiency and accuracy of modal testing is improved. This chapter describes some properties of the FE model of the three-story frame structure and the scaled jacket structure. Both FE models have been developed in ANSYS.

## 4.1 Three-story Frame Structure

In ANSYS, a model of the three-story frame structure is created. The columns are represented by BEAM188 elements, and they are divided by 10mm long elements, resulting in 16 elements per column. Moreover, the floors are represented by SHELL181 elements, with a meshing of size 10mm, resulting in 168 nodes per floor. The model and meshing are shown in Figure 4.1. The most relevant material properties are presented in Table 4.1.

The connection between columns and base plate is considered fully fixed, while the connection between columns and floors is also considered fully fixed at the shell elements (located in mid-plane of the floor).

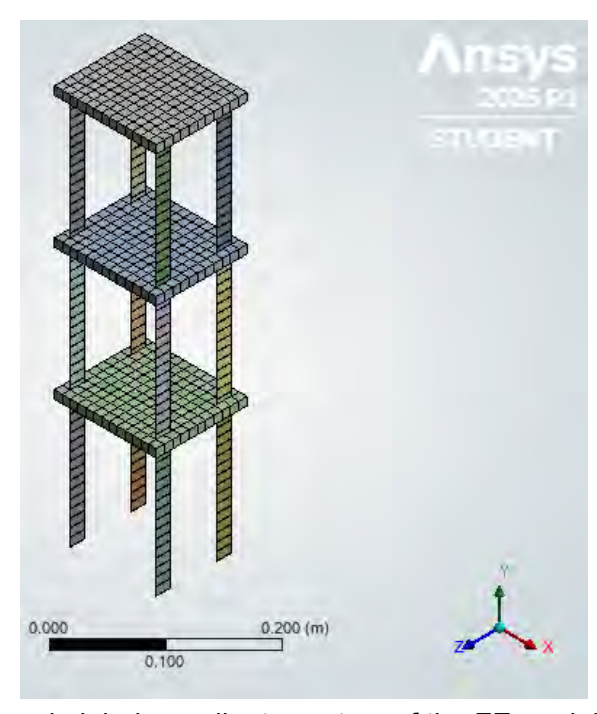


Figure 4.1: Meshing and global coordinate system of the FE model of three-story frame.

Element	Element Type	Density $[kg/m^3]$	Young's modulus [GPa]
Columns	BEAM188	7870	200
Floors	SHELL181	3520	68.95

Table 4.1: Material properties of FE model of three-story frame.

#### 4.1.1 Geometric Stiffness

Since the columns of the frame structure are quite slender and have a low modulus of inertia, the modal properties of the real structure can vary greatly from a traditional FE model. In slender elements, when compression loads are applied, the structure deforms in a way that reduces its effective stiffness. Geometric stiffness analysis is a refined approach that is used to address this issue.

In geometric stiffness analysis, the model accounts for the non-linear, large displacement effects, which results in a more accurate representation of how the structure behaves under compressive loading. As a result, the analysis often leads to a lower stiffness prediction for the system, and therefore to lower natural frequencies in modal analysis. More about geometric stiffness can be read in [30].

In this report, geometric stiffness analysis is used to adjust the FE model of the frame structure, ensuring that the predicted modes are closer to the results obtained in Section 3.2. The results of the FE model are presented in Subsection 6.1.2.

## 4.2 Scaled Jacket Structure

The FE model of the jacket structure is also created in ANSYS. The legs and braces of the jacket structure are represented by BEAM188 elements, and they are divided by elements of 100mm long, resulting in a total of 308 elements. Moreover, the transition piece and the steel base plate is represented by SOLID186 elements, with a meshing using hexahedron and tetrahedron cell shapes, resulting in 1974 elements in total.

The steel base plate is considered to restrain displacements in the X and Y directions, while the neoprene pads work as a spring in the Z direction, whose stiffness is controlled by elastic foundation stiffness. Furthermore, rotations at the supports are driven by the bending stiffness of the steel plate. Finally, the connection between the legs and the transition piece is considered fully fixed.

The model and meshing are shown in Figure 4.2 and the most relevant material properties are presented in Table 4.2.

#### 4.2.1 Geometric Stiffness

In this work, no structure has been placed on top of the scaled jacket, and therefore geometric stiffness does not play a major role in modal analysis. However, geometric

Floment	Floment Type	Density	Young's modulus	Foundation Stiffness
Element	Element Type	$[kg/m^3]$	[GPa]	$[MN/m^3]$
Braces	BEAM188	7870	205	-
Legs	BEAM188	7870	205	-
Transition piece	SOLID186	7870	205	-
Neoprene pads	Elastic Support	-	-	150

Table 4.2: Material properties of FE model of scaled jacket.

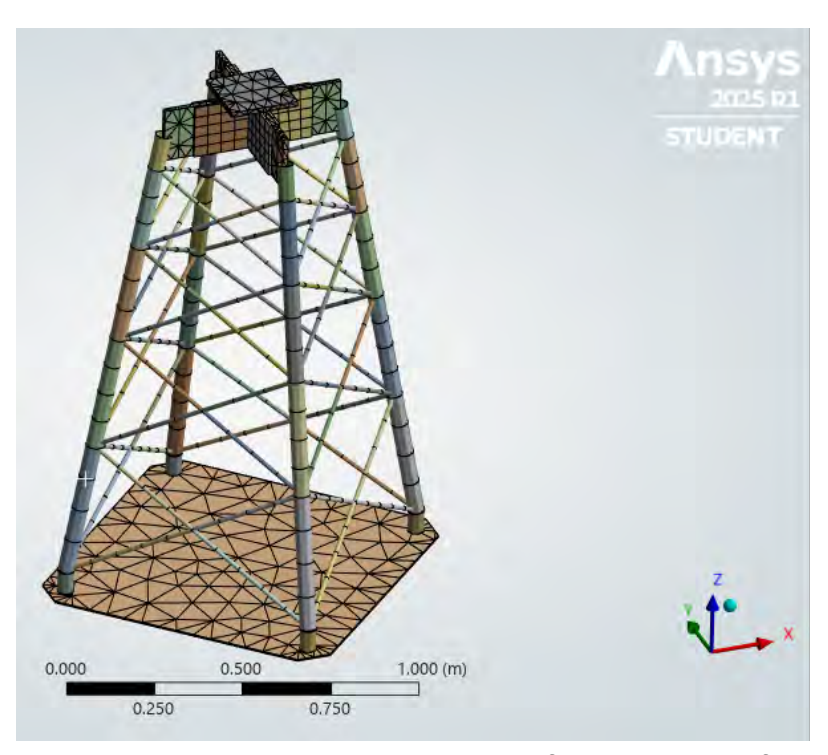


Figure 4.2: Meshing and global coordinate system of the FE model of scaled jacket.

stiffness has been considered for the sake of completeness, and the results of the FE model are presented in Subsection 6.2.2.

# 5 Digital Twin and Damage Detection

This chapter presents the methodology for developing and validating digital twins for the three-story frame structure and the scaled jacket structure. The theoretical background is presented in Section 2.4.

The primary objective is to calibrate the numerical FE models so that their modal characteristics align with experimentally measured frequencies and mode shapes, allowing the models to serve as high-fidelity digital twins for structural health monitoring and damage detection.

Once calibrated, the resulting DTs are used to simulate various damage scenarios by introducing known perturbations (e.g., added mass) to different locations. By comparing the modal features of the Healthy Digital Twin (HDT) and Damaged Digital Twins (DDT), damage is identified through Euclidean distance metrics. The process is applied first to the three-story frame structure and is subsequently repeated for the scaled jacket structure, demonstrating the versatility and robustness of the approach.

## **5.1 Three-story Frame Structure**

In this case, the goal of the optimization process is to match the first three natural frequencies of the FE model with the experimental ones.

As presented in Section 2.4, the first step towards DT is identifying the parameters with the most influence on the modal properties, namely, a sensitivity analysis. Afterwards, optimization techniques are performed.

## 5.1.1 Sensitivity Analysis

The Spearman's rank correlation method provided by ANSYS DesignXplorer is used in the parameter correlation analysis. Following basic knowledge of dynamics, the density and Young's modulus of steel and aluminum/copper are included in the correlation analysis.

Table 5.1 shows the correlation degree of each parameter to the objective function. Positive values represents positive correlation, whereas negative values represents negative correlation.

Figure 5.1 depicts the sensitivity chart, in which the degree of influence of each input parameter on the output parameter can be seen. As expected, the density of aluminum/copper (material of the floors) is inversely proportional to the natural frequencies, whereas

Sensitivities								
Name	P4: Mode 1. Freq.	P9: Mode 2. Freq.	P13: Mode 3. Freq.					
P1: Density of Aluminum/Copper	-0.273	-0.360	-0.353					
P21: Young's modulus 1st Floor	0.861	0.579	0.000					
P22: Young's modulus 2nd Floor	0.373	0.000	0.689					
P23: Young's modulus 3rd Floor	0.000	0.651	0.591					
P23: Young's modulus Alum./Copper	0.000	0.000	0.000					
P25: Density Steel 1st Floor	0.000	0.000	0.000					
P26: Density Steel 2nd Floor	0.000	0.000	0.000					
P27: Density Steel 3rd Floor	0.000	0.000	0.000					

Table 5.1: Parameter correlation for three-story frame structure.

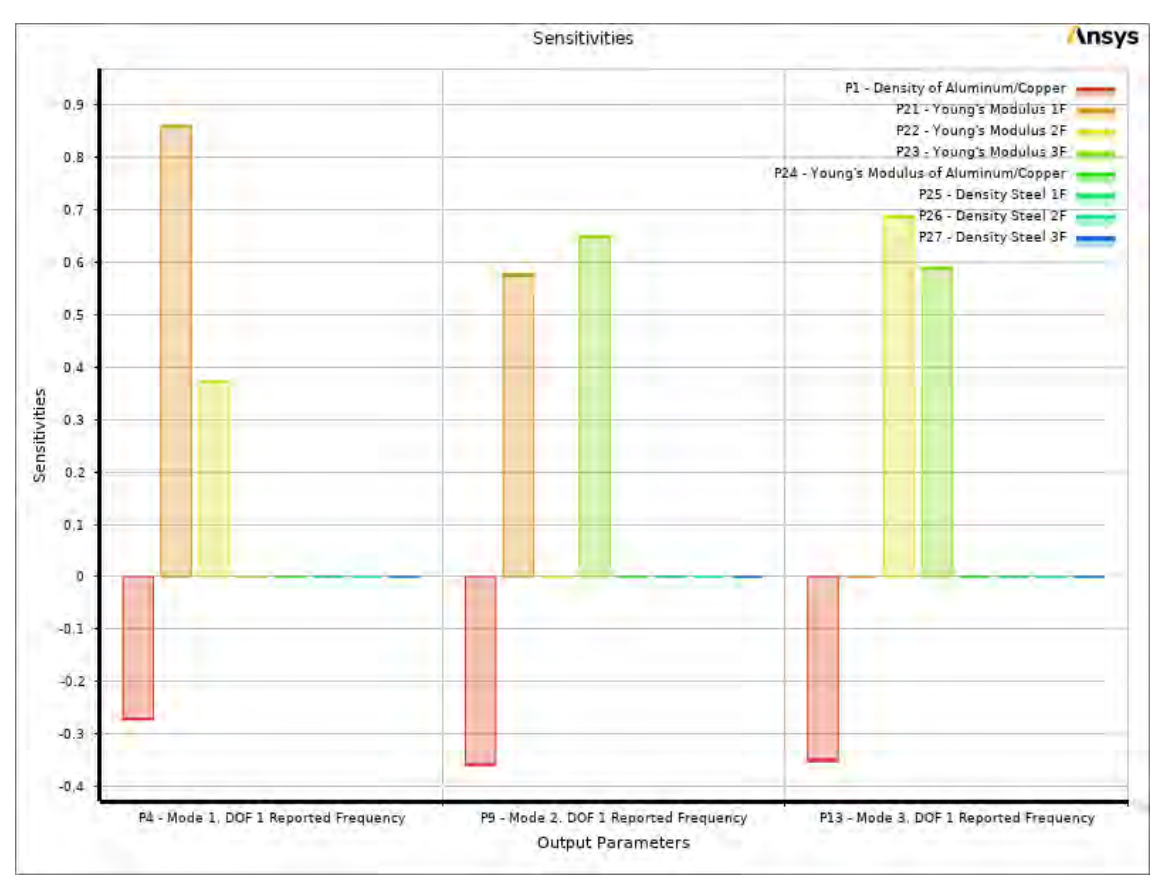


Figure 5.1: Parameter sensitivity chart for three-story frame structure.

Variable	P21: Young's mod. 1st F	P22: Young's mod. 2nd F	P23: Young's mod. 3rd F
	[GPa]	[GPa]	[GPa]
Initial value	200	200	200
Lower bound	180	180	180
Upper bound	220	220	220

Table 5.2: Value range of design variable for three-story frame structure.

the density of the rulers has almost no influence due to its small cross-section area. Moreover, the Young's modulus of the aluminum/copper has no influence on the natural frequencies, whereas the Young's modulus of the rules is proportional to the natural frequencies. Based on the comprehensive analysis of Table 5.1 and Figure 5.1, and considering that the density of aluminum/copper is known (because the mass of the floors have been measured), the Young's modulus of the steel in each floor are finally selected as design variables of this optimization design. The ranges of variation of each design variable are shown in Table 5.2.

### 5.1.2 Generation of experimental design points

In this design, Central Composite Design is adopted. There are three design variables, and 15 sets of design points are generated by the Central Composite method. Table 5.3 shows some of the generated experimental points.

## **5.1.3 Response Surface**

Genetic Agreggation is adopted in this design, which is used to generate many response surfaces. The response surface model constructed by the Young's modulus of the rulers

Order	P21	P22	P23	P4: f <sub>1</sub>	P9: f <sub>2</sub>	P13: f <sub>3</sub>
	[GPa]	[GPa]	[GPa]	[Hz]	[Hz]	[Hz]
1	200	200	200	1.836	5.340	7.822
2	180	200	200	1.756	5.216	7.786
3	220	200	200	1.904	5.460	7.862
13	216.3	183.7	216.3	1.864	5.488	7.830
14	183.7	216.3	216.3	1.802	5.402	8.128
15	216.3	216.3	216.3	1.929	5.595	8.185

Table 5.3: Experimental design points for three-story frame structure.

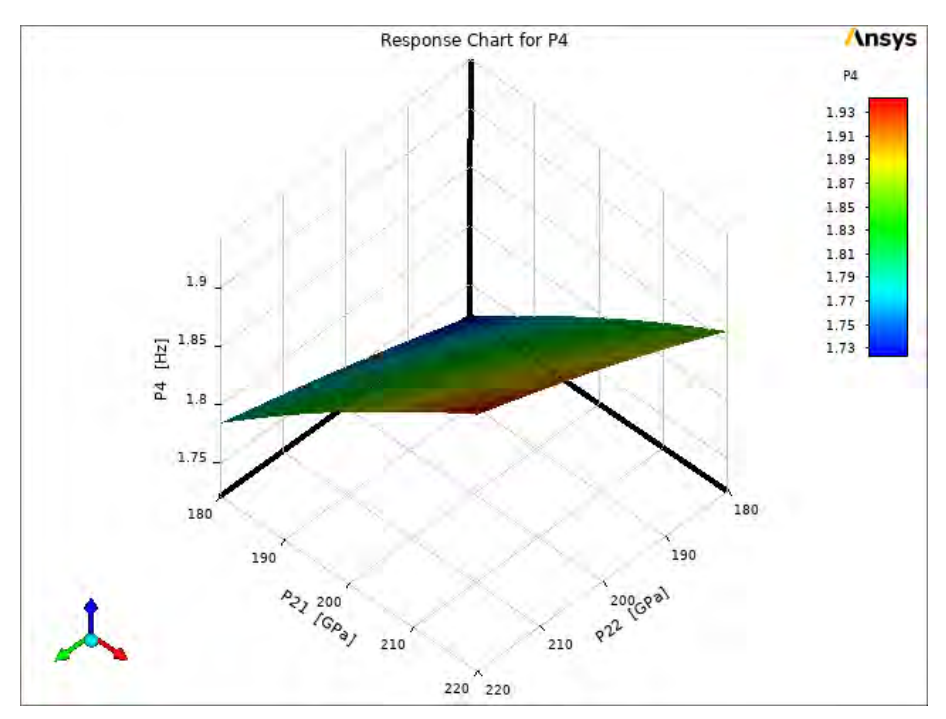


Figure 5.2: First-frequency response surface. P4 is the natural frequency for the first mode, P21 is the Young's modulus of the rulers in first floor, and P22 is the Young's modulus of the rulers in second floor.

in the first floor (P21), Young's modulus of the rulers in the second floor (P22), and the first natural frequency (P4) is shown as an example in Figure 5.2.

## 5.1.4 Response Surface Optimization

The goal of the optimization process is to match the first three natural frequencies of the FE model with the experimental frequencies, which are obtained through EMA or OMA.

In this case, NSGA-II is used and the result of the optimization is presented in Subsection 6.1.3.

## 5.1.5 Damage Detection

The different "damages" are presented and shown in Subsection 3.2.1. Table 5.4 summarizes the different cases and locations, and the relative frequency difference of the first three frequencies. It can be seen that the different damages produce an average relative frequency difference of 2.5%.

As described in Section 2.5, the HDT and the DDT are compared to each other. The first

		Case 1	Case 2	Case 3	Case 4	Case 5	Case 6	Case 7
Location	1st floor	Х			Χ	Х		Χ
of the mass	2nd floor		Χ		Χ		Χ	Χ
or the mass	3rd floor			Χ		Χ	Χ	Χ
Rel. freq.	1st freq.	0.77	1.72	2.27	2.47	3.00	3.90	4.62
difference	2nd freq.	2.36	0.39	1.63	2.71	3.94	2.06	4.31
[%]	3rd freq.	0.87	2.28	0.96	3.18	1.87	3.24	4.18

Table 5.4: Location of the mass for different cases and its relative frequency difference. The "X" represents if there is a 38g mass on the specific floor or not. The relative frequency difference is calculated as per Equation (2.26).

$\delta_{f1}$	$\delta_{f2}$	$\delta_{f3}$	$\delta_{MAC1}$	$\delta_{MAC2}$	$\delta_{MAC3}$
0	0	0	0	0	0
0.00768	0.02363	0.00869	0.00002	0.00124	0.00279
0.01722	0.00391	0.02284	0.00001	0.00014	0.00148
0.02271	0.01635	0.00958	0.00002	0.00133	0.00137
0.02473	0.02706	0.03183	0.00004	0.00165	0.00204
0.03000	0.03942	0.01866	0.00001	0.00020	0.00170
0.03903	0.02060	0.03240	0.00000	0.00087	0.00258
0.04616	0.04313	0.04183	0.00001	0.00005	0.00004
	0.00768 0.01722 0.02271 0.02473 0.03000 0.03903	0 0 0.00768 0.02363 0.01722 0.00391 0.02271 0.01635 0.02473 0.02706 0.03000 0.03942 0.03903 0.02060	0         0         0           0.00768         0.02363         0.00869           0.01722         0.00391         0.02284           0.02271         0.01635         0.00958           0.02473         0.02706         0.03183           0.03000         0.03942         0.01866           0.03903         0.02060         0.03240	0         0         0         0           0.00768         0.02363         0.00869         0.00002           0.01722         0.00391         0.02284         0.00001           0.02271         0.01635         0.00958         0.00002           0.02473         0.02706         0.03183         0.00004           0.03000         0.03942         0.01866         0.00001           0.03903         0.02060         0.03240         0.00000	0         0         0         0         0           0.00768         0.02363         0.00869         0.00002         0.00124           0.01722         0.00391         0.02284         0.00001         0.00014           0.02271         0.01635         0.00958         0.00002         0.00133           0.02473         0.02706         0.03183         0.00004         0.00165           0.03000         0.03942         0.01866         0.00001         0.00020           0.03903         0.02060         0.03240         0.00000         0.00087

Table 5.5: Relative frequency differences and  $\delta_{MAC}$  values of training vectors for three-story frame structure. Relative frequency differences are calculated with Equation (2.26).

	$\delta_{f1}$	$\delta_{f2}$	$\delta_{f3}$	$\delta_{MAC1}$	$\delta_{MAC2}$	$\delta_{MAC3}$
HDT vs Test	0.001742	0.020739	0.000181	0.004767	0.000155	0.002551

Table 5.6: Relative frequency differences and  $\delta_{MAC}$  values of test vector (example) for three-story frame structure. Relative frequency differences are calculated with Eq. (2.26).

three frequencies and mode shapes of the HDT and DDTs can be seen in Subsubsection A.4.1, while the relative frequency difference  $\delta_f$  and  $\delta_{MAC}$  values (that is, training vectors) are shown in Table 5.5.

The first three frequencies and mode shapes of all the tests performed using EMA and OMA can be seen in Subsubsection A.4.1. As an example, the procedure for one of the tests is described, whose state is supposed to be unknown. However, it is already known that it is Case 1. The relative frequency difference and  $\delta_{MAC}$  values (that is, test vector) are shown in Table 5.6.

Based on the undamaged tests, the weights are calculated according to Equation (2.29), and the values are presented in Table 5.7. It can be observed that all the features contribute roughly equally to the classifier, which means that there is no characteristic that dominates the classifier.

	$\delta_{f1}$	$\delta_{f2}$	$\delta_{f3}$	$\delta_{MAC1}$	$\delta_{MAC2}$	$\delta_{MAC3}$
$\overline{w}$	0.236	0.419	0.344	0.205	0.302	0.493

Table 5.7: Weights applied to relative frequency differences and  $\delta_{MAC}$  values of three-story frame structure.

	HDT	Case 1	Case 2	Case 3	Case 4	Case 5	Case 6	Case 7
Euclidean dis.	0.0137	0.0065	0.0189	0.0122	0.0222	0.0214	0.0263	0.0358

Table 5.8: Euclidean distances between training vectors and test vector of three-story frame structure.

Sensitivities									
Name	P5: Freq. Mode 1	P6: Freq. Mode 2	P10: Freq. Mode 12						
P1: Young's modulus Braces	0.012	0.012	0.860						
P2: Young's modulus Legs	0.012	0.012	0.076						
P3: Young's modulus TP	0.001	0.001	0.072						
P4: Foundation Stiffness	0.985	0.985	0.001						

Table 5.9: Parameter correlation for scaled jacket structure. Mode 12 is a torsional mode.

The Euclidean distances calculated with Equation (2.31) are shown in Table 5.8. It can be seen that the smallest distance corresponds to Case 1, and therefore the damage is predicted as Case 1.

The results of all the tests in the three-story frame structure are presented in Subsection 6.1.4.

## 5.2 Scaled Jacket Structure

The same procedure as in Section 5.1 is repeated for the scaled jacket structure. Therefore, some information has been omitted in this section. If the reader would like to know about the entire process, please refer to Section 5.1.

### 5.2.1 Sensitivity Analysis

The Spearman's rank correlation method is also used during the parameter correlation analysis, where the Young's modulus of the braces, legs, and transition piece are included in the correlation analysis, as well as the foundation stiffness of the neoprene pads (elastic support). Note that in this case, the density of the braces, legs, and TP have not been included, since they can be easily measured in the laboratory, and therefore there is no uncertainty on the mass of the structure.

Table 5.9 shows the degree of correlation of each parameter with the objective function, and Figure 5.3 depicts the local sensitivity chart. It can be seen that the Young's modulus of braces and legs is proportional to the first and second frequencies, but only with a low influence compared to the foundation stiffness of the neoprene pads, which drives the first two natural frequencies. On the other hand, the foundation stiffness of the pads does not play a role in the torsional frequency, whereas the Young's modulus of the braces has the most influence on the torsional frequency, with a low contribution from the Young's modulus of the legs and transition piece.

However, it must be noted that a drawback of performing a sensitivity analysis using AN-SYS is the fact that it is not possible to set a type of mode as a parameter but a specific mode number. This means that, for example, if the input parameters change so that mode 12 is not the torsional mode anymore, then some bias is introduced in the analysis. This could be solved by adding more output parameters that keep track of the mode shapes. However, this has not been done in the present analysis.

Based on a comprehensive analysis of Table 5.9 and Figure 5.3, and considering that the Young's modulus of the transition piece has a low influence on the analysis, the Young's

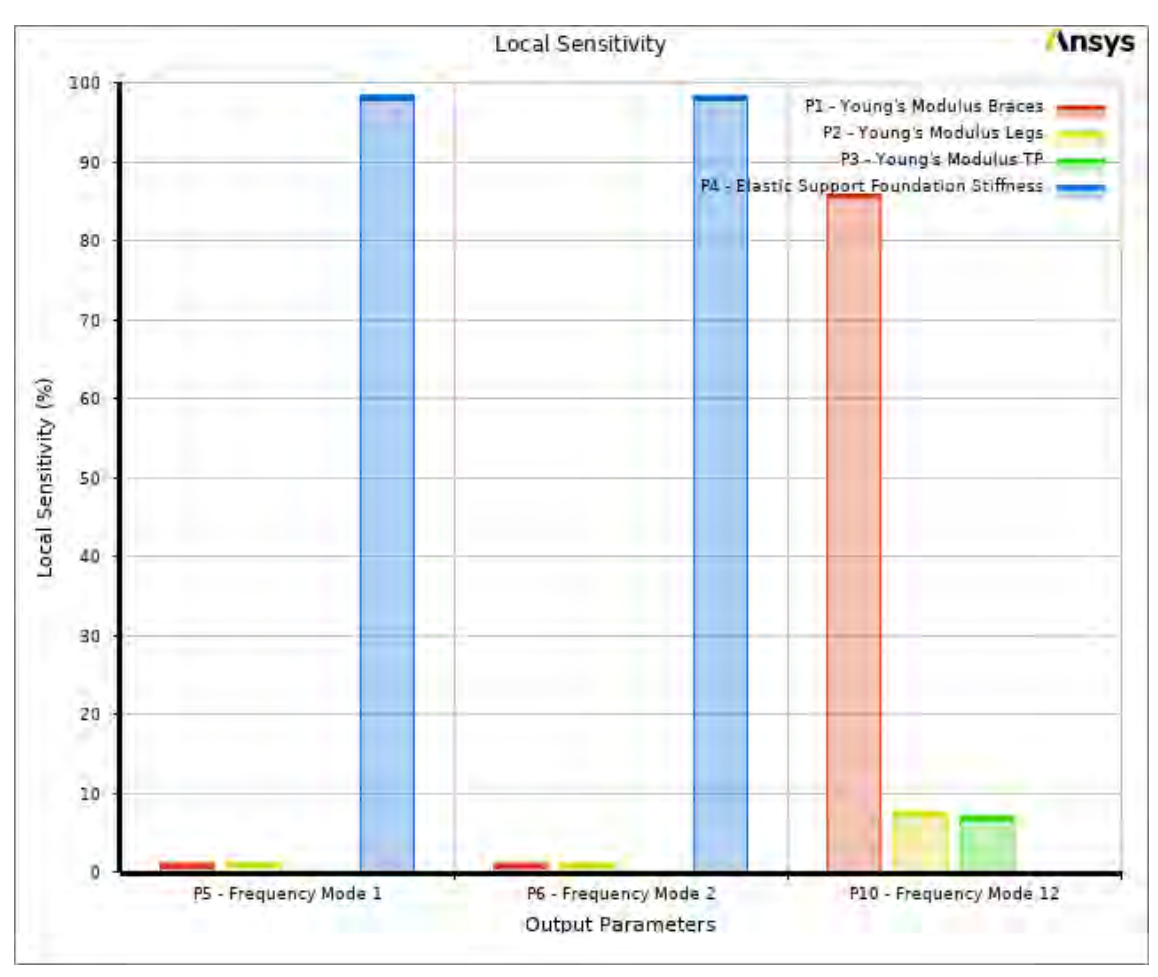


Figure 5.3: Parameter sensitivity chart for scaled jacket structure. Mode 12 is a torsional mode.

Variable	P1: Young's modulus braces	P2: Young's modulus legs	P3: Foundation stiffness
	[GPa]	[GPa]	[MN/m <sup>3</sup> ]
Initial value	205	205	150
Lower bound	160	160	100
Upper bound	230	230	200

Table 5.10: Value range of design variables for scaled jacket structure.

modulus of braces and legs and foundation stiffness of neoprene pads are selected as design variables. The ranges of variation of each design variable are shown in Table 5.10.

## 5.2.2 Generation of experimental design points

Central Composite Design method is also adopted in this case. There are three design variables, and fifteen sets of design points are generated by the aforementioned method. Table 5.11 shows some of the experimental points generated.

### 5.2.3 Response Surface

An example of a response surface is shown in Figure 5.4, which is generated using Genetic Agreggation, and is constructed by the Young's modulus of braces (P1), the foundation stiffness of the pads (P3), and the first natural frequency (P4).

Order			P3: F. Stiffness	<b>P4</b> : $f_1$	P5: f <sub>2</sub>	P6: f <sub>12</sub>
	[GPa]	[GPa]	$[MN/m^3]$	[Hz]	[Hz]	[Hz]
1	195	195	150	15.830	15.833	145.91
2	160	195	150	15.792	15.795	133.41
3	230	195	150	15.856	15.859	157.05
7	233.46	166.54	190.65	17.719	17.724	153.70
8	166.54	223.46	190.65	17.724	17.728	136.61
9	223.46	223.46	190.65	17.797	17.801	156.12

Table 5.11: Experimental design points for scaled jacket structure.

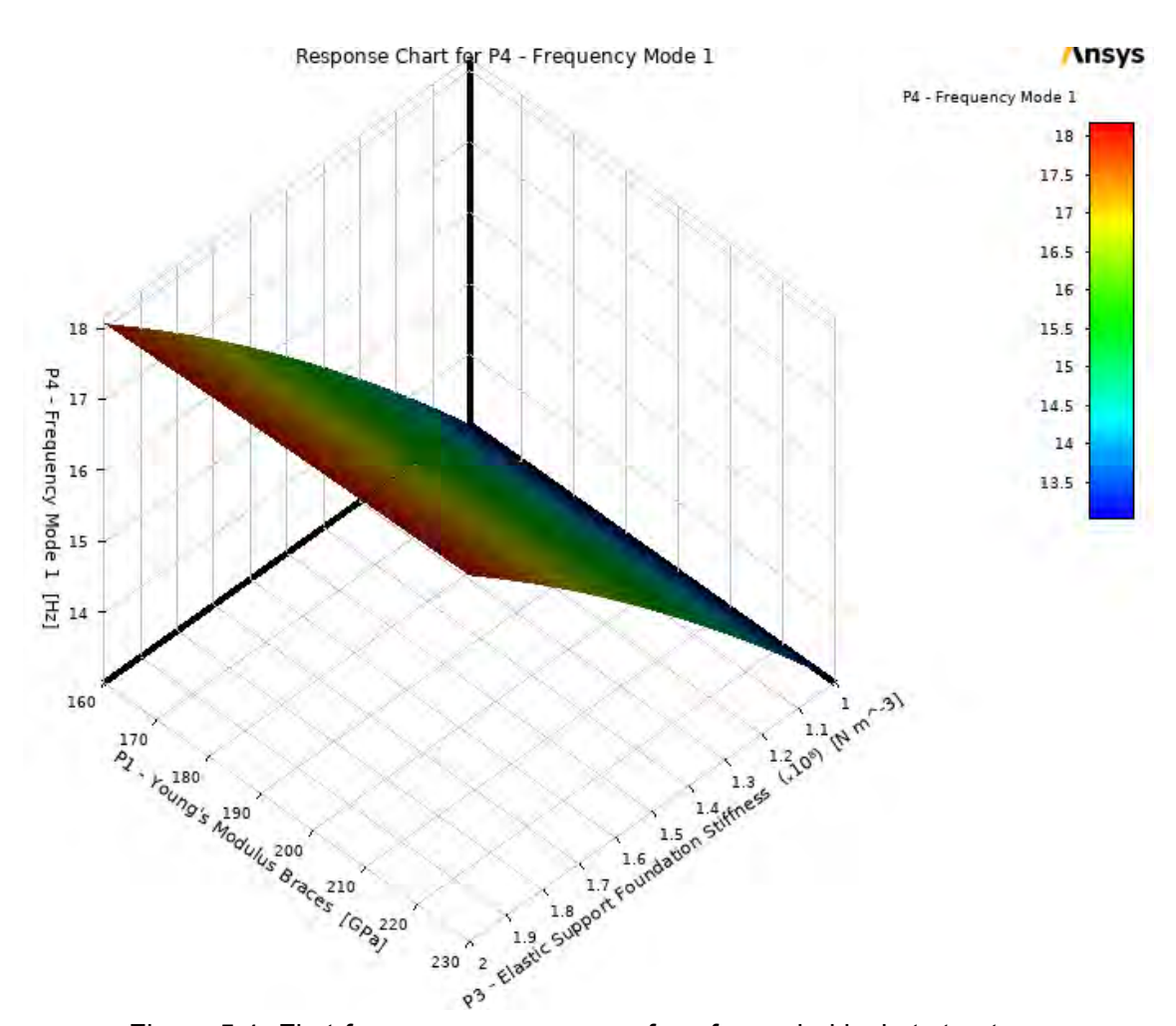


Figure 5.4: First-frequency response surface for scaled jacket structure.

## 5.2.4 Response Surface Optimization

The goal of optimization is to match the first two natural frequencies (bending modes) and the torsional frequency of the FE model with the experimental frequencies, which are obtained using OMA.

In this case, NSGAII is used and the result of the optimization is presented in Subsection 6.2.3.

## 5.2.5 Damage Detection

The different "damages" are presented and shown in Subsection 3.3.1. Table 5.12 summarizes the different cases and locations, and the relative frequency differences of the first two modes (bending modes) and torsional mode. It can be seen that the different damages produce an average relative frequency difference of 6.3%.

Frequencies and mode shapes of the HDT and DDTs of the scaled jacket structure can be seen in Subsubsection A.4.2, while the change in frequency and MAC values (i.e., training vectors) are displayed in Table 5.13.

The frequencies of the two bending and torsional modes with their corresponding mode shapes of all the tests performed using OMA can be seen in Subsubsection A.4.2. The general procedure is described in Section 2.5, while an example is presented for the three-story frame structure in Subsection 5.1.5.

Based on the undamaged tests, the weights are calculated according to Equation (2.29) and the values are presented in Table 5.14. It can be observed that the weight corresponding to  $\delta_{MAC_T}$  dominates the MAC-based contributions, suggesting that the classifier may

		Case 1	Case 2	Case 3	Case 4	Case 5	Case 6	Case 7
	Top Plate	6.72 kg						
Location of magnets	Nodes level 30		5.04 kg					
	Nodes level 40			5.04 kg				
	Nodes level 85				5.04 kg			
	Node 30B0P0					5.04 kg		
	Node 40B0P0					_	5.04 kg	
	Node 85B0P0							5.04 kg
Rel. freq.	X-direction freq.	8.45	2.11	3.59	5.91	1.90	3.45	6.44
difference	Y-direction freq.	8.44	2.11	3.59	5.91	2.32	3.74	6.58
[%]	Torsional freq.	2.37	6.90	9.51	13.06	8.99	10.50	16.06

Table 5.12: Location of the mass for different cases and its relative frequency difference. The relative frequency difference is calculated as per Equation (2.26).

	$\delta_{f_X}$	$\delta_{f_Y}$	$\delta_{f_T}$	$\delta_{MAC_X}$	$\delta_{MAC_Y}$	$\delta_{MAC_T}$
HDT vs HDT	0	0	0	0	0	0
HDT vs Case 1	0.08448	0.08442	0.02367	0.00005	0.00004	0.00012
HDT vs Case 2	0.02108	0.02109	0.06905	0.00001	0.00001	0.00340
HDT vs Case 3	0.03587	0.03588	0.09510	0.00000	0.00000	0.00083
HDT vs Case 4	0.05908	0.05909	0.13060	0.00000	0.00000	0.00089
HDT vs Case 5	0.01904	0.02321	0.08992	0.01358	0.01347	0.02266
HDT vs Case 6	0.03451	0.03739	0.10497	0.01334	0.01316	0.00695
HDT vs Case 7	0.06439	0.06584	0.16064	0.00786	0.00771	0.01255

Table 5.13: Relative frequency differences and  $\delta_{MAC}$  values of training vectors for scaled jacket structure. Relative frequency differences are calculated with Equation (2.26).

					$\delta_{MAC_Y}$	
$\overline{w}$	0.544	0.168	0.288	0.066	0.071	0.862

Table 5.14: Weights applied to relative frequency differences and  $\delta_{MAC}$  values of scaled jacket structure.

be over-relying on a single mode in terms of MAC values.

The results of all the tests on the scaled jacket are presented in Subsection 6.2.4.

# 6 Results

The setup of the experiments and procedures are described in Chapter 3. The finite element models are presented in Chapter 4, and the digital twin and damage detection method are described in Chapter 5. In the present chapter, all the results of the aforementioned sections are presented.

## **6.1 Three-story Frame Structure**

This section presents the results of EMA, OMA, FE model, digital twin and the damage detection method for the three-story frame structure.

#### 6.1.1 EMA and OMA

This subsection shows the primary experimental findings using two different methods: EMA and OMA.

#### **EMA**

Figure 6.1 presents the Frequency Response Functions (FRF) from the impact hammer test using EMA hitting the structure on the third floor, which corresponds to the third DOF. Specifically, the PSD of the input (impact hammer) is displayed in Figure 6.1a, while Figure 6.1b, 6.1c, and 6.1d correspond to FRFs and coherence of the output of the 1st, 2nd and 3rd floor, respectively.

From the frequency spectrum in Figure 6.1, three prominent peaks can be identified approximately at frequencies 1.79 Hz, 5.28 Hz, and 7.76 Hz. These peaks align with areas of relatively high coherence. However, low coherence values are observed at frequencies less than 1 Hz for signal 1. This may be caused by the low receptance of the input in that frequency band.

Furthermore, mode shapes and damping ratios derived from experimental methods - using the SDyPy module - are presented in Table 6.1 and the former are depicted in Figure 6.2. In this case, the mode shapes are normalized using unity normalization (that is, the mode shape is scaled so that its largest component has a magnitude of 1).

#### OMA

To estimate the modal parameters using OMA, it is chosen to use the FDD and SSI-Cov which are presented in Subsection 2.2.3, and Subsection 2.2.4, respectively. Signal processing techniques, such as decimation, filtering and construction of the SD matrix are described in Section 3.2

Figure 6.3 shows: (a) time history, (a) normalized auto-correlation function, (c) probability density function, (d) power spectral density, and (e) normal probability plot of the first output response. It can be seen that the excitation is fairly random and the shape of the

Floor	$f_1$ $[Hz]$	$f_2$ $[Hz]$	$f_3$ $[Hz]$	ζ <sub>1</sub> [%]	$\zeta_2$ [%]	ζ <sub>3</sub> [%]	$u_1$	$u_2$	$u_3$
$\overline{m_1}$							0.41	1	-0.65
$m_2$	1.79	5.28	7.76	1.20	0.15	0.40	0.87	0.31	1
$m_3$							1	-0.74	-0.47

Table 6.1: First three natural frequencies, damping ratio and mode shapes of three-story frame structure obtained using EMA.

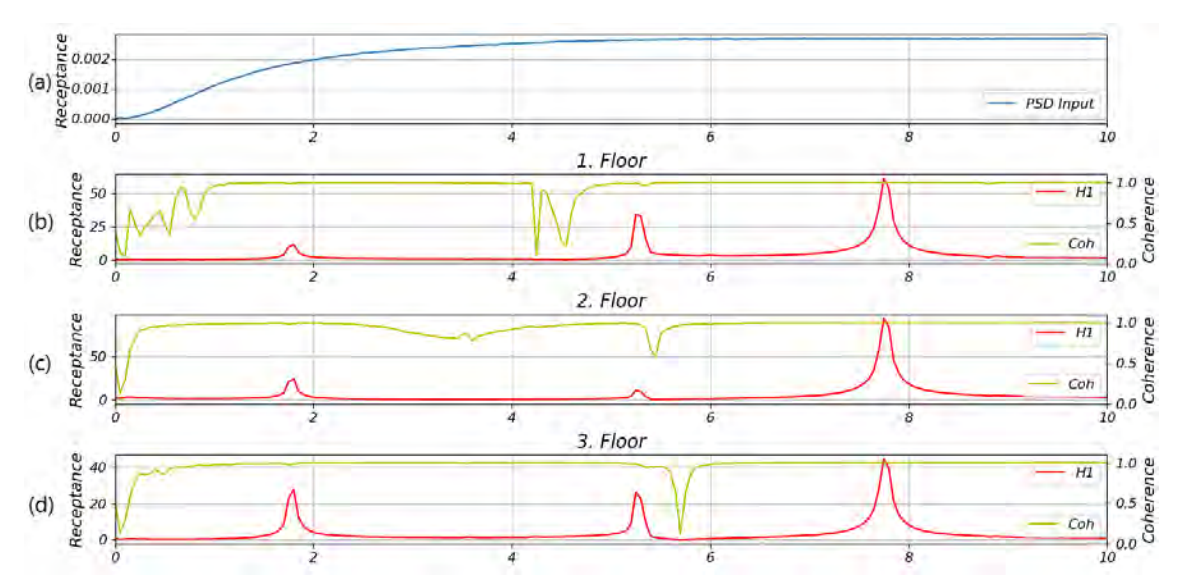


Figure 6.1: (a) shows the PSD of the input. (b), (c) and (d) shows the FRFs and coherence of the output in 1st, 2nd and 3rd floor.

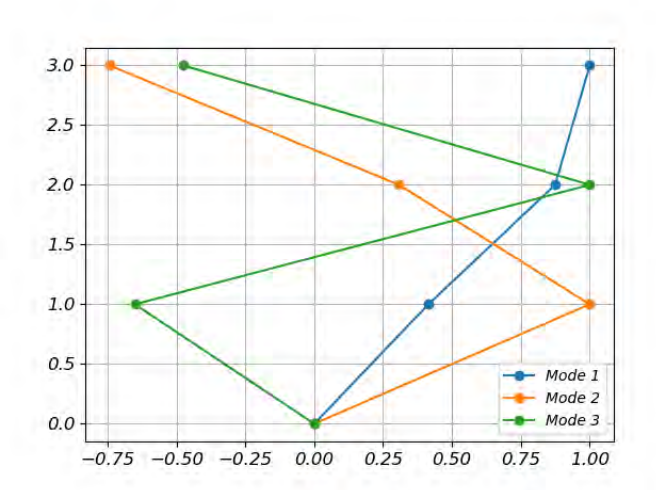


Figure 6.2: Mode shapes obtained with EMA in three-story frame structure.

Probability Density Function (PDF) looks closer to a Gaussian shape centered around 0, but with a sharper peak. The singular value plots of the SD matrices are shown in Figure 6.4, in which there are three clear peaks that correspond to the first three expected modes.

Natural frequencies, damping ratios, and mode shapes are estimated using OMA and shown in Table 6.2. Moreover, Figure 6.5 depicts the mode shapes for the first three modes using OMA.

When comparing the results obtained with EMA and OMA, it can be seen that the natural frequencies deviate up to 0.64%, which is explained by the uncertainty of the methods. Moreover, MAC values are close to unity (0.999). However, the estimation of damping ratios shows a significant inaccuracy, with relative deviations ranging from 55.5% to 81.2%, making it not suitable as a parameter for damage detection. This outcome is not surprising, as the determination of damping ratios using OMA tends to be more complex than

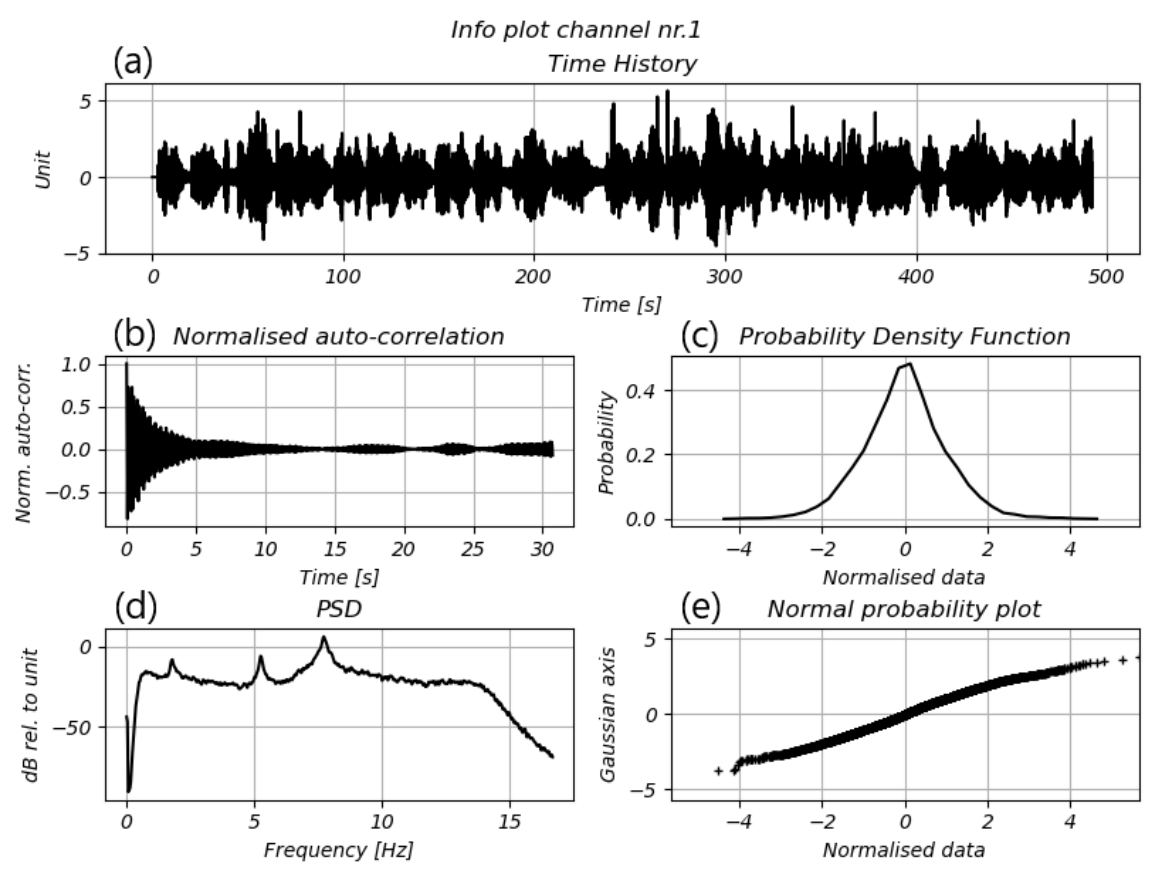


Figure 6.3: Info plot for measurement channel nr. 1 of three-story frame structure.

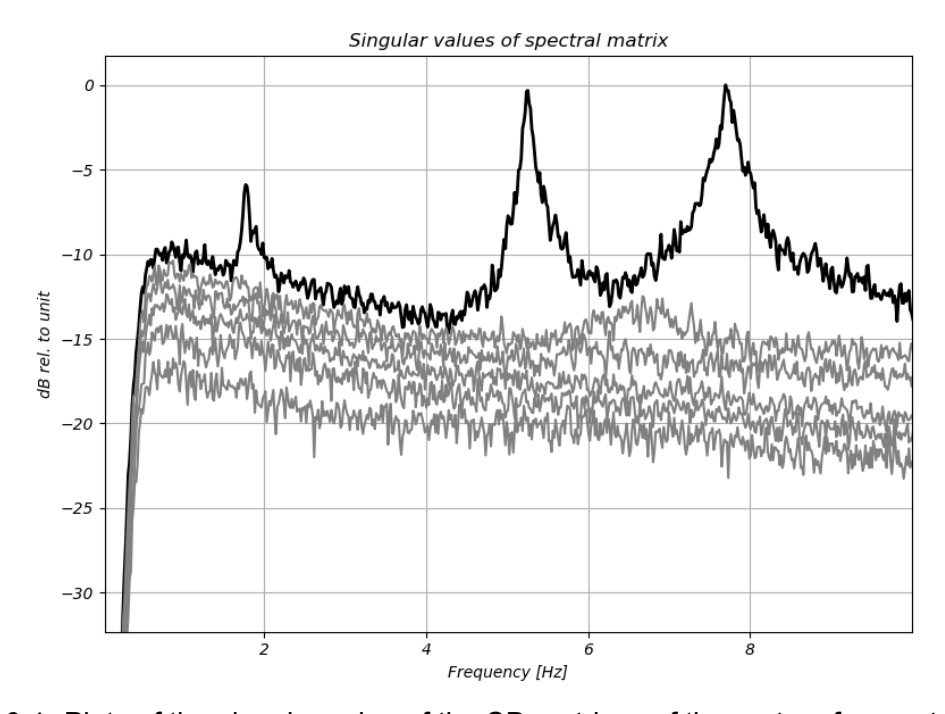


Figure 6.4: Plots of the singular value of the SD matrices of three-story frame structure.

Floor	$f_1$ $[Hz]$	$f_2\\[Hz]$	$f_3$ $[Hz]$	ζ <sub>1</sub> [%]	$\zeta_2$ [%]	ζ <sub>3</sub> [%]	$u_1$	$u_2$	$u_3$
$\overline{m_1}$							0.45	1	-0.64
$m_2$	1.78	5.25	7.73	3.0	8.0	0.9	0.91	0.29	1
$m_3$							1	-0.73	-0.48

Table 6.2: First three natural frequencies, damping ratio and mode shapes of three-story frame structure obtained with OMA.

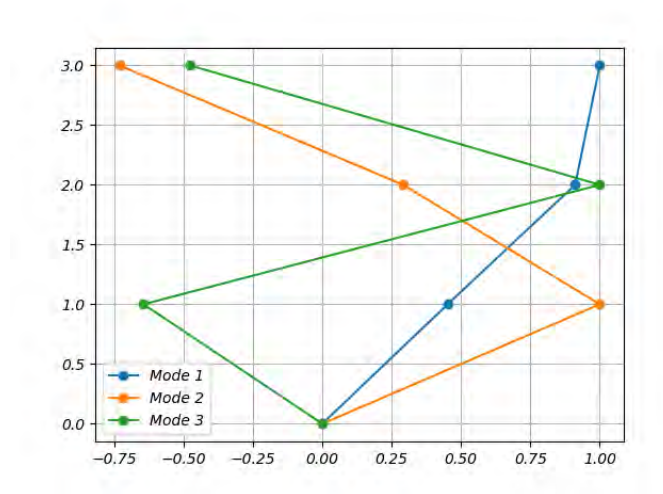


Figure 6.5: Mode shapes obtained with OMA in three-story frame structure.

	$f_1$ [Hz]	$f_2$ [Hz]	$f_3$ [Hz]	$u_1$	$u_2$	$u_3$
$\overline{m_1}$				-0.49	1.08	0.73
$m_2$	1.84	5.34	7.82	-0.84	0.32	-1.07
$m_3$				-1.00	-0.83	0.56

Table 6.3: First three natural frequencies and mode shapes of three-story frame structure obtained from FE model.

identifying natural frequencies or mode shapes. A key reason for this difficulty lies in the limitations of signal processing methods, which struggle to effectively mitigate random and systematic errors in the data. Moreover, OMA relies on the assumption that the excitation force is both random and uncorrelated (an assumption that is hard to fulfill when an impact hammer is used to excite the structure).

#### 6.1.2 Finite Element Model

The natural frequencies and modes shapes of the first three modes for the FE model are presented in Table 6.3, and the latter are illustrated in Figure 6.6. ANSYS normalizes the mode shapes using mass normalization (i.e., the mode shape is scaled so that the modal mass is 1).

Table 6.4 presents the difference between considering geometric stiffness or not. In this case, since the columns have a low modulus of inertia, the relative differences in frequency are 11.5%, 8.5%, and 7.6% for the first, second, and third frequencies. Therefore, geometric stiffness should never be ignored in columns with a low modulus of inertia.

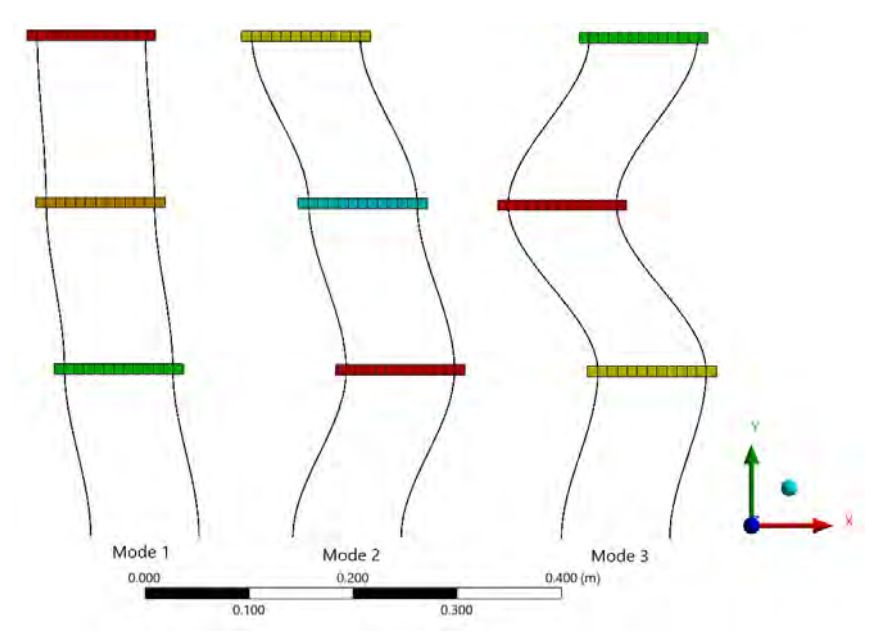


Figure 6.6: Mode shapes of three-story frame structure obtained from FE model.

	$f_1$	$f_2$	$f_3$
	[Hz]	[Hz]	[Hz]
Geometric stiffness OFF			
Geometric stiffness ON	1.84	5.34	7.82
Difference [%]	11.5	8.5	7.6

Table 6.4: Change in natural frequencies when considering geometric stiffness in three-story frame structure. The difference is set as  $\delta_f = (f_{OFF} - f_{ON})/f_{OFF}$ .

Nine experiments were conducted using EMA and OMA, and they are compared with the FE model. Figure 6.7 presents box plots with the difference in the first three natural frequencies and MAC values between EMA and FEM, while Figure 6.8 shows the same between OMA and FEM. Since the difference in the first frequency is around 3% and the lowest MAC value on the diagonal is 0.985, it is clear that a FEM update is needed.

## 6.1.3 Digital Twin

In this case, the goal of the optimization process is to match the first three natural frequencies of the FE model with the experimental frequencies (which are calculated as the average of all the OMA tests). Therefore, the objectives are the natural frequencies 1.78 Hz, 5.25 Hz and 7.73 Hz for the first, second, and third vibration modes, respectively.

Taking into account the procedure presented in Section 5.1, the selected candidate point and its corresponding design variables are shown in Table 6.5. As mentioned in Section 4.1, the supports are assumed to be fully fixed, and the column-to-floor connections are modeled as rigid. This assumption is known to be somewhat inaccurate, which is why the Young's modulus of the columns are reduced during the model update process.

If the same box plots as in Subsection 6.1.2 are plotted (Figure 6.9), it can be seen that the overall performance of the FEM has been improved and is now called Healthy Digital Twin (HDT).

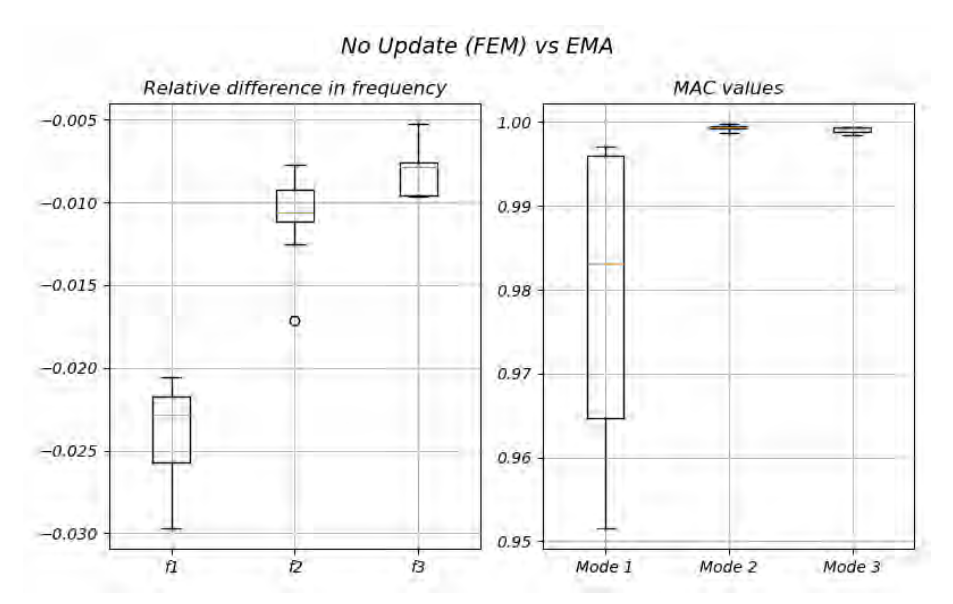


Figure 6.7: Box plots with comparison between FEM and EMA in three-story frame structure.

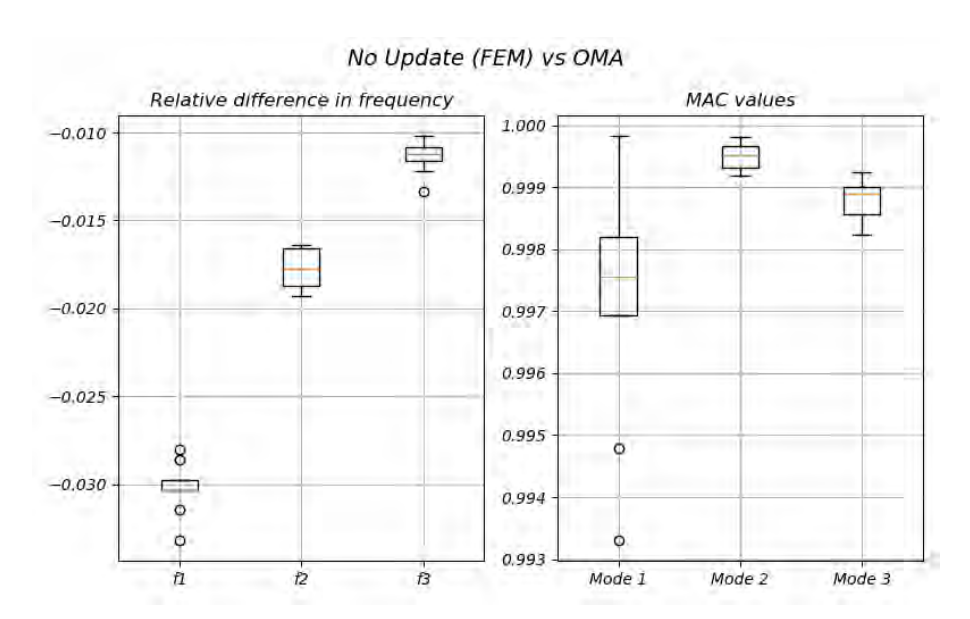


Figure 6.8: Box plots with comparison between FEM and OMA in three-story frame structure.

## 6.1.4 Damage Detection

The procedure behind the damage detection method is presented in Subsection 5.1.5. Since there are many tests that are classified, a confusion matrix is used, which helps to assess the classification model performance by comparing predicted values against actual values for a dataset. Figures 6.10 and 6.11 show the confusion matrix using EMA and OMA, respectively.

The classes in the confusion matrix have been ordered such that those that are more similar to each other in terms of euclidean distance (Equation (2.31)) are positioned adjacently. This ordering facilitates the identification of confusion patterns, for example in Figure 6.11, where misclassifications occur because the two "damages" are similar to

	P21:	P22:	P23:	P4:	P9:	P13:
	Y. mod. 1F	Y. mod. 2F	Y. mod. 3F	$f_1$	$f_2$	$f_3$
	[GPa]	[GPa]	[GPa]	[Hz]	[Hz]	[Hz]
No Updated FEM	200	200	200	1.84	5.34	7.82
Digital Twin	188.7	194.7	199.1	1.78	5.25	7.73

Table 6.5: Optimization result in three-story frame structure.

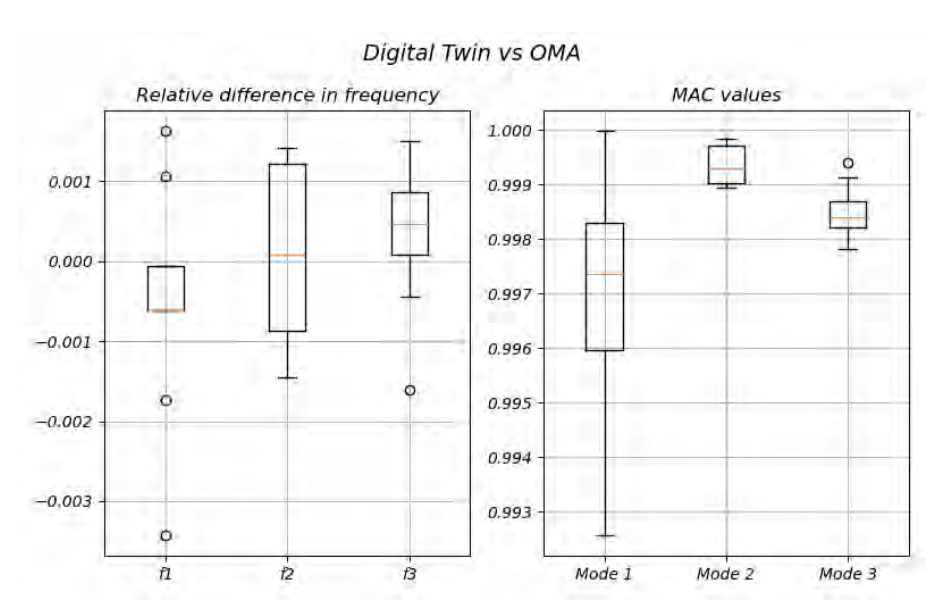


Figure 6.9: Box plots with comparison between HDT and OMA in three-story frame structure.

each other and the digital twin is not capable of distinguishing them.

The similarity between each damaged case can be determined by multiplying each column in Table 6.4 by its corresponding weight (Table 5.7), adding them all and calculating the difference between adjacent cases. This is done in Table 6.6, and it can be seen that "Case 2" is more similar to the HDT than "Case 1", and therefore, they are swapped in the confusion matrix. This is useful for understanding why some tests are misclassified: as long as the predicted values are close to the diagonal, the misclassification occurs because the predicted case is the most similar to the correct one.

The accuracy of the method for EMA is 97%, while for OMA is 93.3%. Note that this accuracy belongs to a "damage" (mass) that produces an average relative frequency difference of 2.5%. Moreover, it is important to note that there are no misclassifications between damaged and undamaged states. Therefore, if the state is predicted to be undamaged,

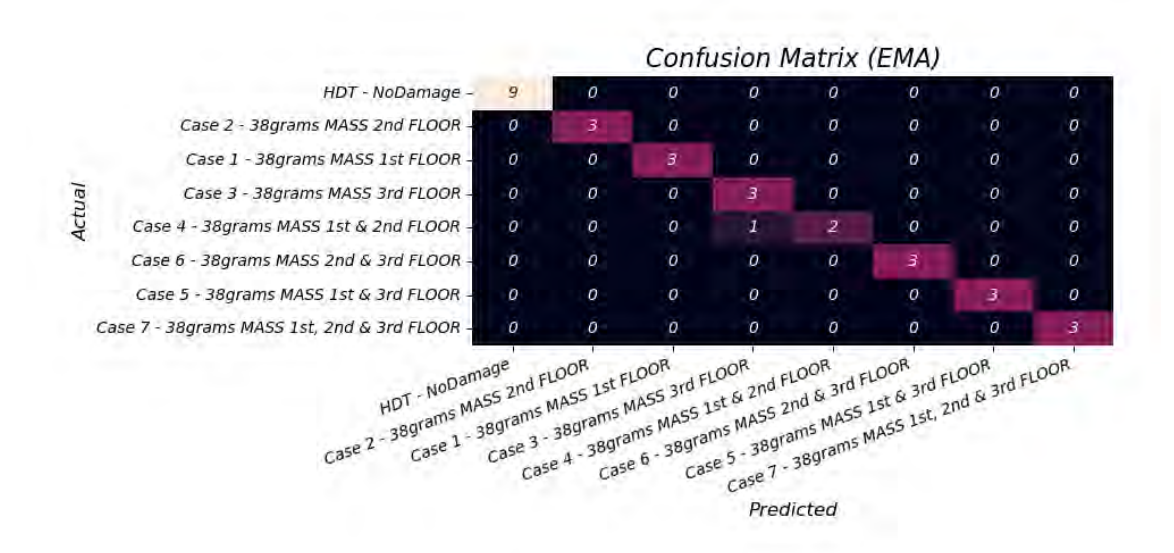


Figure 6.10: Confusion Matrix using EMA in three-story frame structure.

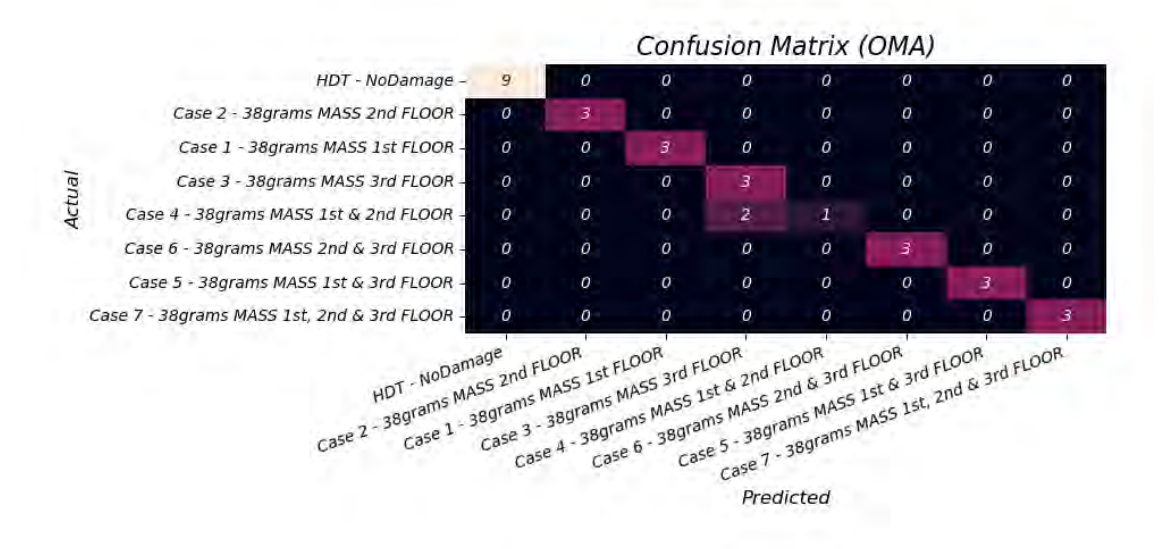


Figure 6.11: Confusion Matrix using OMA in three-story frame structure.

	$w_{\delta_f} \cdot \delta_f + w_{\delta_{MAC}} \cdot \delta_{MAC}$	Similarity		
HDT vs HDT	0.0000	0.0165	-	
HDT vs Case 1	0.0165	0.0103	-0.0021	
HDT vs Case 2	0.0143	0.0022	-0.0021	
HDT vs Case 3	0.0166	0.0022	0.0131	
HDT vs Case 4	0.0297	0.0013	0.0131	
HDT vs Case 5	0.0309	0.0013	-0.0004	
HDT vs Case 6	0.0306	0.0129	-0.0004	
HDT vs Case 7	0.0434	0.0129	-	

Table 6.6: Similarity between adjacent cases in three-story frame structure.

it is correct 100% of the time.

In this thesis, robustness refers to the classifier's ability to:

- Maintain high accuracy across different scenarios,
- Handle measurement variability, noisy data, or non-uniform data quality,
- Still make correct predictions even if some features are weak or misleading.

One way to evaluate robustness is to analyze the effect of weights. The impact of feature weighting is evaluated by comparing the classification accuracy with and without applying inverse coefficient of variation weights. For the three-story frame structure using OMA, the accuracy dropped slightly from 93.3% to 90% when weights were not applied (the confusion matrix for the method using no weights is shown in Subsection A.6.1). This suggests that the method is naturally robust (less sensitive to weighting) in simple structures.

### 6.2 Scaled Jacket Structure

This section presents the results of OMA, FE model, digital twin and the damage detection method for the scaled jacket structure. In this case, EMA is not presented in the results section because it is not really applicable to large structures. Nevertheless, EMA tests are still performed and they serve as comparison with OMA.

#### 6.2.1 OMA

FDD and SSI-Cov identification methods are also used to estimate the modal parameters. Signal processing techniques, such as decimation, filtering and construction of the SD matrix are described in Section 3.3.

Figure 6.12 shows: (a) time history, (b) normalized auto-correlation function, (c) probability density function, (d) power spectral density, and (e) normal probability plot of output response number 2. It can be seen that the excitation is fairly random; however, the PSD is sharply peaked at zero and it resembles more a Laplace distribution. The fact that the PSD is not Gaussian could introduce some bias in mode extraction; nevertheless, this seems to have a low influence on the results. The singular value plots of the SD matrices are shown in Figure 6.13. It can be seen that a reasonable number of singular values are well separated from the noise floor, which is a good sign in modal identification, since it avoids some problems such as modes disappearing because of low excitation, closely spaced modes that are not so well defined, and modes appearing where do not belong.

Natural frequencies, damping ratios, and mode shapes obtained with OMA are estimated on the basis of the previous paragraph, and can be seen in Table 6.7. Moreover, Figure 6.14 shows the mode shapes for the two bending modes and the torsional mode

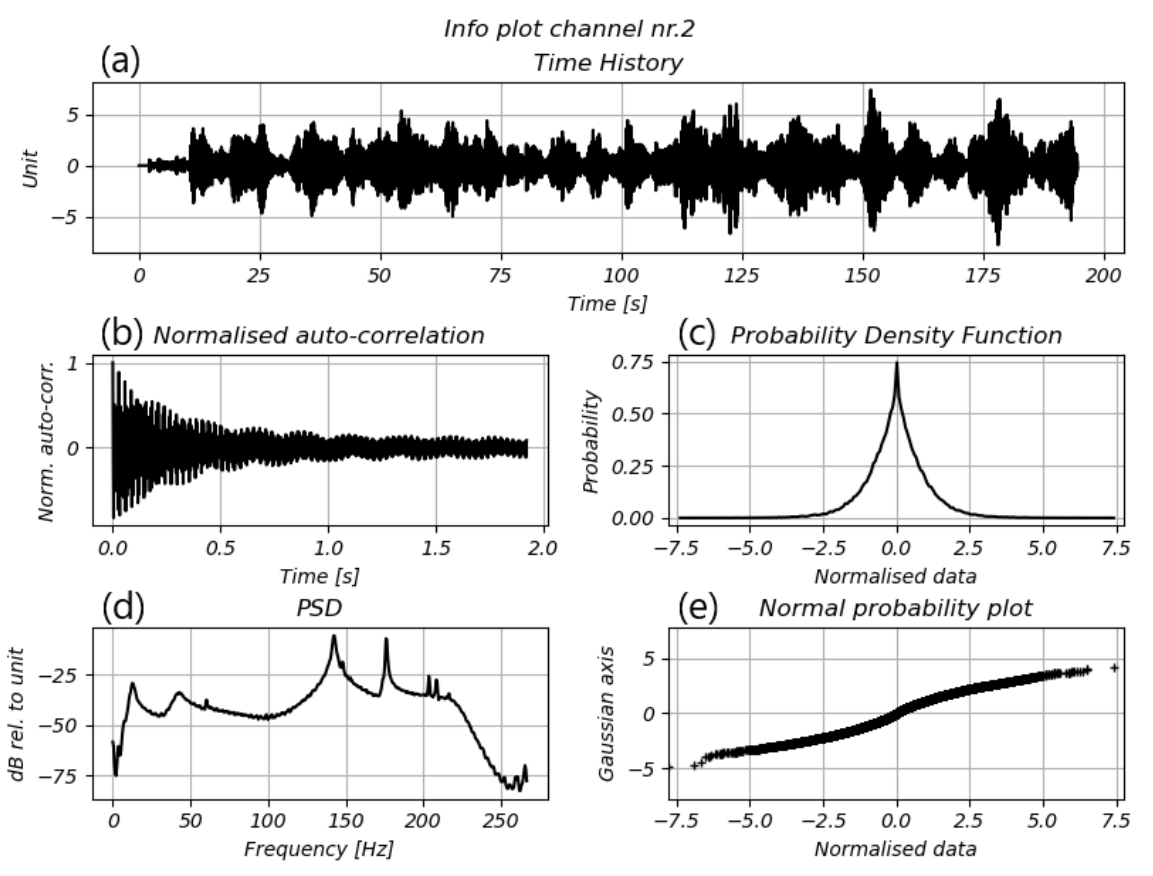


Figure 6.12: Info plot for measurement channel nr. 2 of scaled jacket structure.

obtained with OMA. The names and location of the accelerometers can be seen in Figure 3.10.

### 6.2.2 Finite Element Model

The natural frequencies and modes shapes of the first two modes (bending modes) and torsional mode for the FE model are presented in Table 6.8. The mode shapes are illustrated in Figure 6.15. ANSYS normalize the mode shapes using mass normalization (i.e. the mode shape is scaled so that the modal mass is 1).

Table 6.9 presents the difference between considering geometric stiffness or not. In this case, since there is no structure on top of the jacket foundation, geometric stiffness does not play a role in modal analysis. However, it is still considered for the sake of completeness.

$f_X$ $[Hz]$	$f_Y \ [Hz]$	$f_T \\ [Hz]$	$\zeta_X$ [%]	$\zeta_Y \ [\%]$	$\zeta_T$ [%]	Location of acc.	$u_X$	$u_Y$	$u_T$
						X-dir. HalfHeight (ch.1)	0.59	-0.08	0.47
		13.29 142.60		7.5	5 0.4	X-dir. TP1 (ch.2)	1	-0.09	0.91
10.60	12.20		7.5			X-dir. TP2 (ch.3)	1	-0.11	-0.90
12.68	13.29		7.5			Y-dir. HalfHeight (ch.4)	0.03	0.54	-0.48
						Y-dir. TP3 (ch.5)	0.05	0.96	-0.98
						Y-dir. TP4 (ch.6)	0.05	1	1

Table 6.7: Frequencies, damping ratio and mode shapes of scaled jacket structure obtained with OMA.

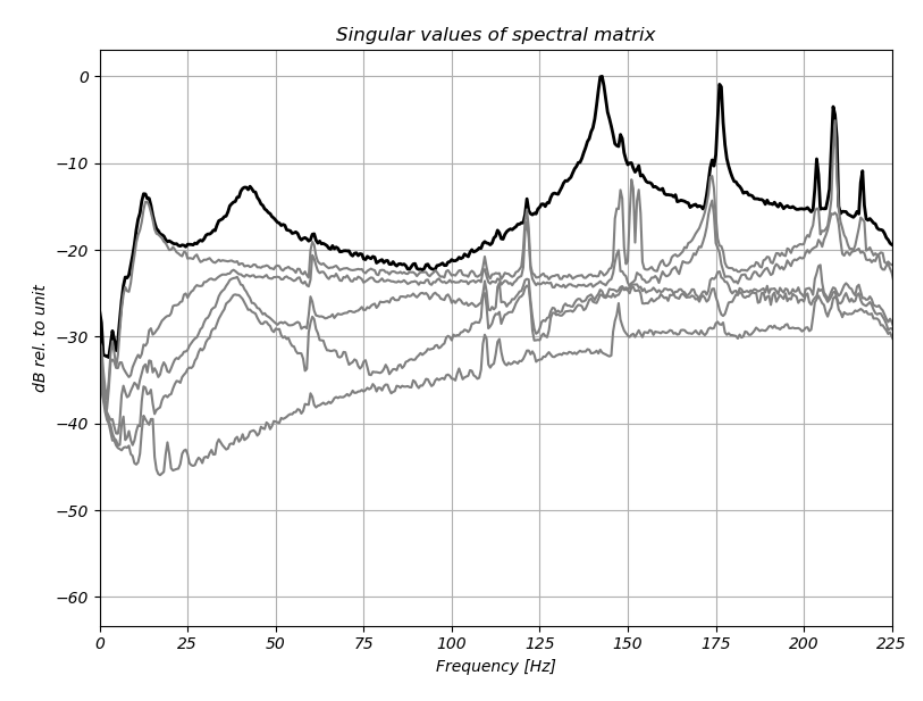


Figure 6.13: Plots of the singular value of the SD matrices of scaled jacket structure.

$\frac{f_X}{[Hz]}$	$\begin{array}{c} f_Y \\ [Hz] \end{array}$	$f_T \\ [Hz]$	Location of acc.	$u_X$	$u_Y$	$u_T$
15.85	15.85	154.34	X-dir. HalfHeight (ch.1)	-0.068	0.009	-0.135
			X-dir. TP1 (ch.2)	-0.16	0.02	-0.25
			X-dir. TP2 (ch.3)	-0.16	0.02	0.24
			Y-dir. HalfHeight (ch.4)	0.01	0.07	0.14
			Y-dir. TP3 (ch.5)	0.02	0.16	0.25
			Y-dir. TP4 (ch.6)	0.02	0.16	-0.25

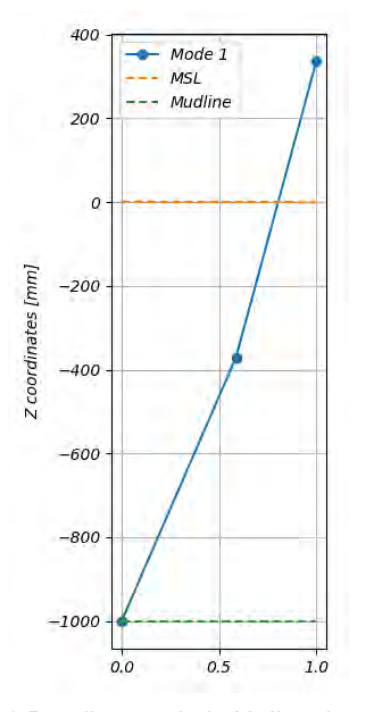
Table 6.8: Modal properties of first two bending modes, and torsional modes of the jacket structure's FE model.

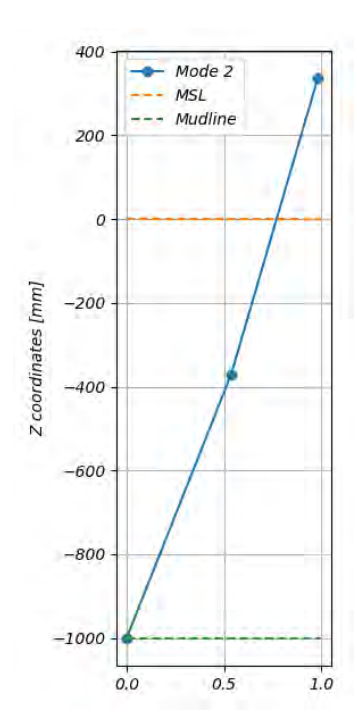
Nine experiments were conducted for OMA and they are compared with the FE model. Figure 6.16 presents box plots with the relative difference in natural frequencies and MAC values between OMA and FE model. Since the difference in frequency of the bending mode in X-direction is around 25% and the lowest MAC value on the diagonal is 0.91, it is clear that a FEM update is needed.

## 6.2.3 Digital Twin

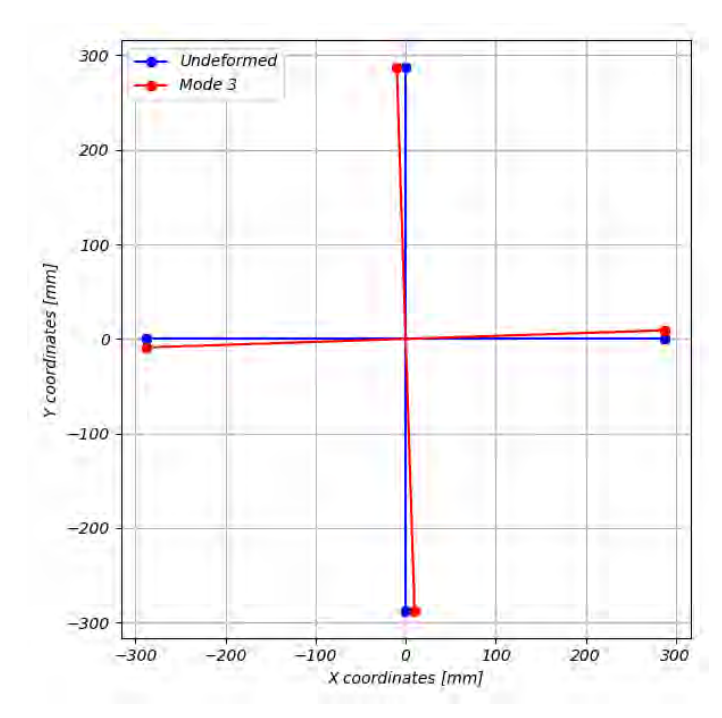
In this case, the goal of the optimization process is to match the first two natural frequencies (bending modes) and the torsional frequency of the FE model with the experimental frequencies (which are calculated as the average of all the OMA tests). Therefore, the objectives are the natural frequencies 12.68 Hz, 13.29 Hz, and 142.61 Hz, which correspond to the bending modes in X and Y directions, and the torsional mode, respectively.

Based on the procedure presented in Section 5.2, the selected candidate point and its design variables are shown in Table 6.10. The joints in the FE model are assumed to be fully rigid, which does not reflect the real behavior due to weld flexibility and fabrication imperfections. To account for this, the Young's modulus of the braces is reduced from 205



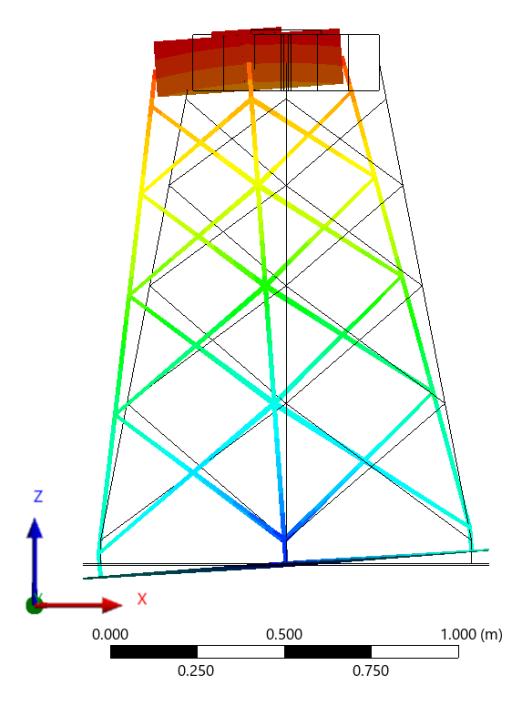


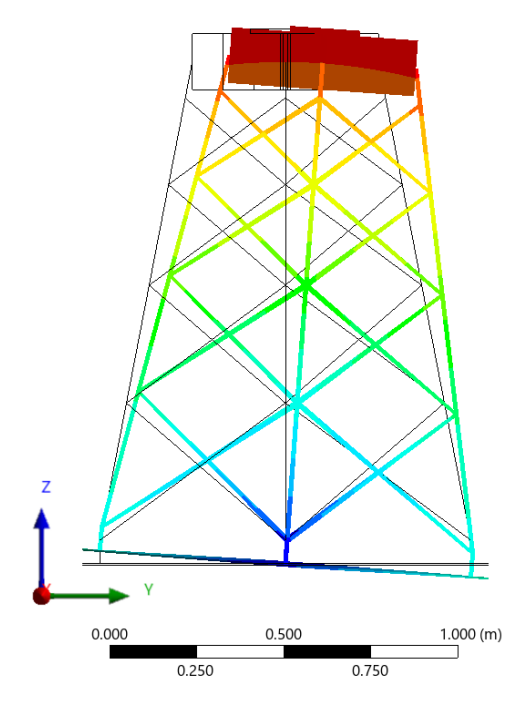
- (a) Bending mode in X-direction.
- (b) Bending mode in Y-direction.



(c) Torsional mode. Top view.

Figure 6.14: Mode shapes obtained with OMA in scaled jacket structure.





(a) Bending mode in X-direction.

(b) Bending mode in Y-direction.

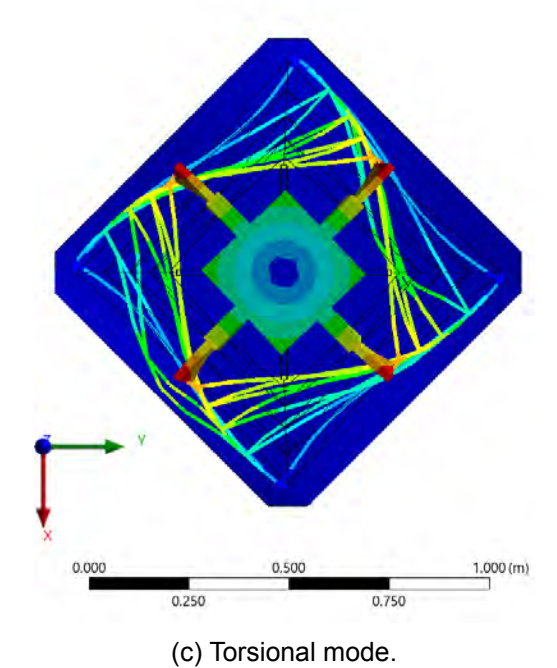


Figure 6.15: Mode shapes from FE model of scaled jacket structure

	$f_X$	$f_Y$	$f_T$
	[Hz]	[Hz]	[Hz]
Geometrical stiffening OFF	15.855	15.852	154.34
Geometrical stiffening ON	15.850	15.847	154.34
Difference [%]	0.03	0.03	0.00

Table 6.9: Change in natural frequencies when considering geometric stiffness in scaled jacket structure. The difference is set as  $\delta_f = (f_{OFF} - f_{ON})/f_{OFF}$ .

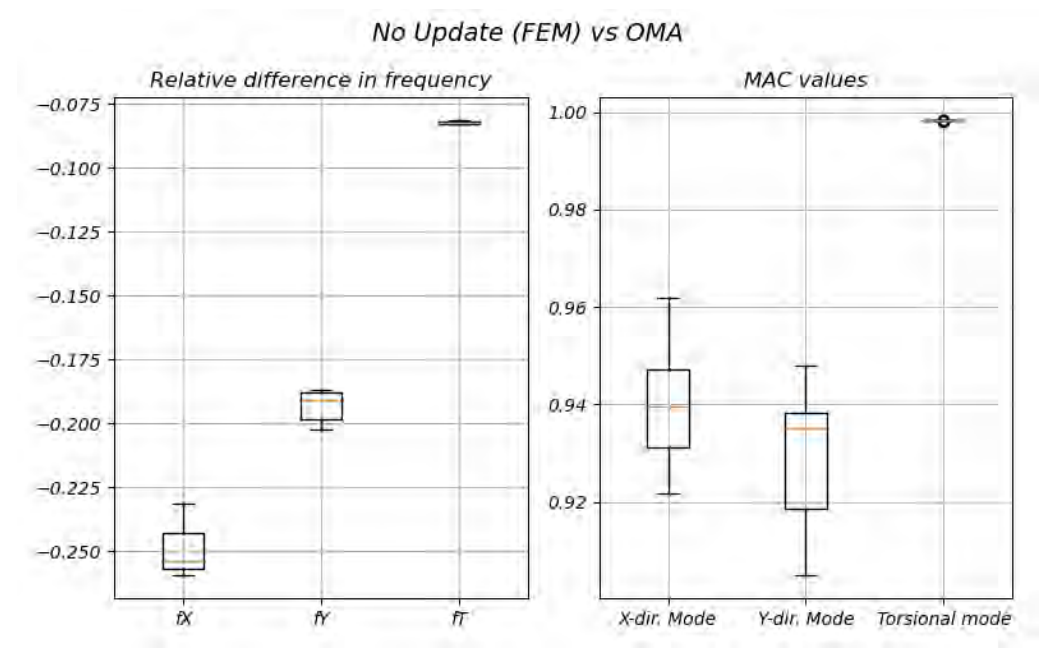


Figure 6.16: Box plots with comparison between FEM and OMA in scaled jacket structure.

	Young's modulus brace	Young's modulus leg	Foundation Stiffness	$f_X$	$f_Y$	$f_T$
	[GPa]	[GPa]	$[MN/m^3]$	[Hz]	[Hz]	[Hz]
No Updated FEM	205	205	150	15.850	15.847	154.34
Digital Twin	169.28	204.21	102.66	13.186	13.184	142.80

Table 6.10: Optimization result in scaled jacket structure.

GPa to 169.3 GPa. Additionally, the foundation stiffness of the neoprene rubber is set to 102.66 MN/m<sup>3</sup>. When multiplied by the neoprene thickness (7mm), this corresponds to a Young's modulus of approximately 0.71 MPa, which is representative of soft neoprene.

If the same box plots as in Subsection 6.2.2 are plotted (Figure 6.17), it can be seen that the overall performance of the FEM of the scaled jacket has been improved and now is called Healthy Digital Twin HDT. Nevertheless, the overall performance of the update in the scaled jacket is not as good as it is in the three-story frame structure due to several reasons. First, a jacket structure is a more complex structure with not clearly defined boundary conditions, which increases the uncertainties in the FE model. Moreover, the construction process and welding of the scaled jacket introduce a lot of imperfections that are difficult to measure and model. Last but not least, the fact that the first two bending modes are closely spaced introduces some uncertainty in modal identification.

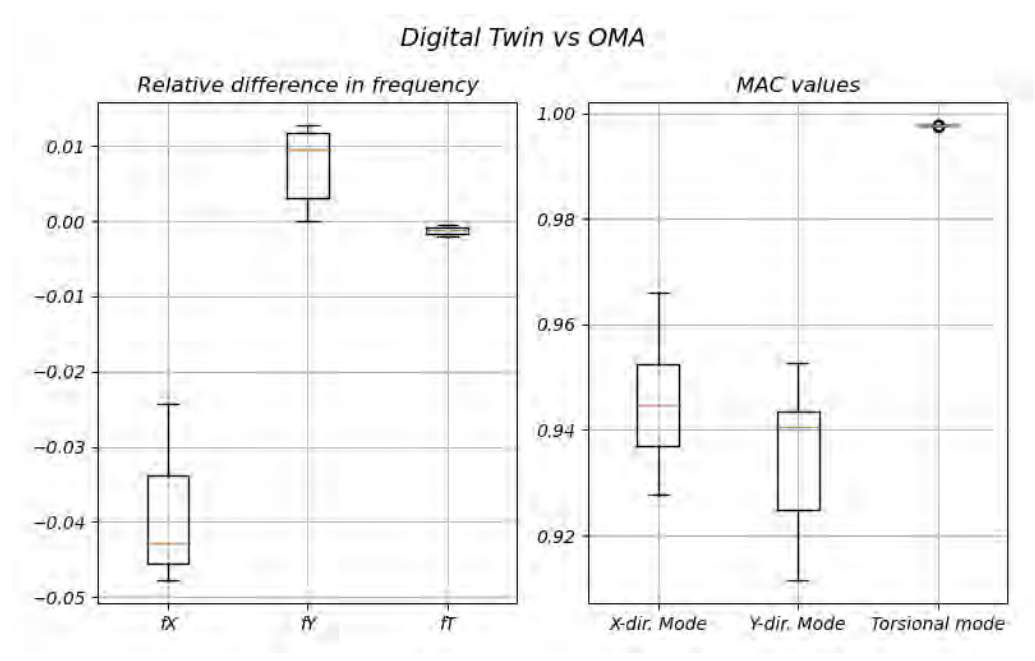


Figure 6.17: Box plots with comparison between HDT and OMA in scaled jacket structure.

	$w_{\delta_f} \cdot \delta_f + w_{\delta_{MAC}} \cdot \delta_{MAC}$	Similarity		
HDT vs HDT	0.0000	0.0378	-	
HDT vs Case 2	0.0378	0.0376	0.0158	
HDT vs Case 3	0.0536	0.0079	0.0136	
HDT vs Case 5	0.0615	0.0079	0.0015	
HDT vs Case 6	0.0631	0.0040	0.0013	
HDT vs Case 1	0.0671	0.0040	0.0134	
HDT vs Case 4	0.0804	0.0238	0.0134	
HDT vs Case 7	0.1042	0.0230	-	

Table 6.11: Similarity between cases in scaled jacket structure.

### 6.2.4 Damage Detection

The procedure behind the method is presented in Subsection 5.2.5. A confusion matrix is also used to present the result of the predictions, in which the cases have also been ordered so that the most similar cases are next to each other. For more details on this topic, see Subsection 6.1.4.

The similarity between the cases can be seen in Table 6.11, in which the cases have already been ordered in the table so that the most similar cases are next to each other. Furthermore, the confusion matrix is shown in Figure 6.18, in which it should be noted that missclassifications occur only because the predicted cases are more similar to the correct one. Additionally, it seems that the digital twin has some issues differentiating between a mass concentrated in one node at level 85 and masses evenly distributed in all nodes at level 85.

The accuracy of the method for OMA is 90% for a mass that represents 10% of the total weight of the structure and that produces an average relative frequency difference of 6.3%.

Moreover, the impact of feature weighting is evaluated by comparing the classification

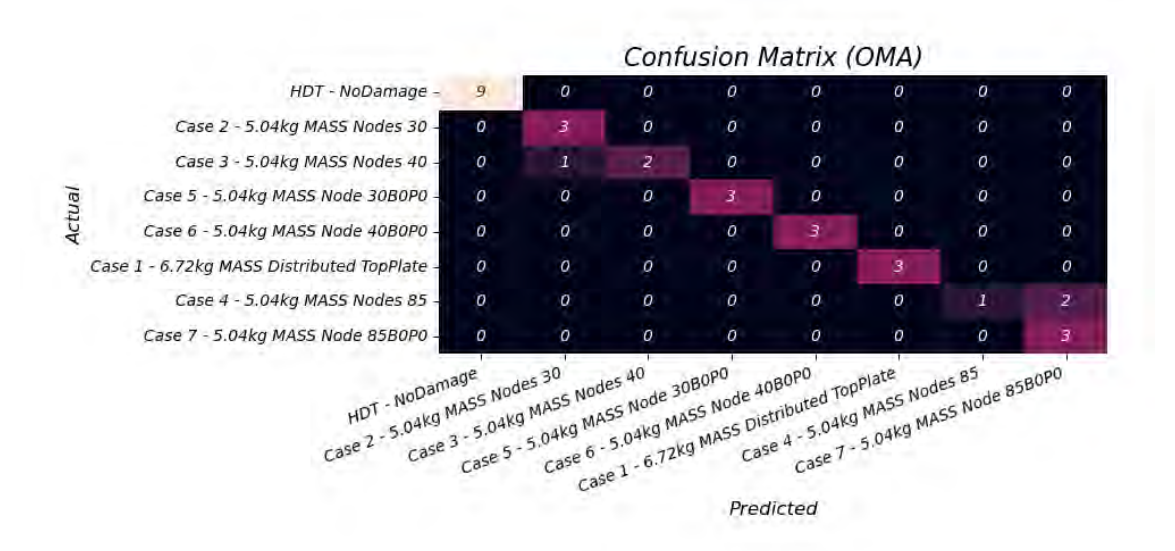


Figure 6.18: Confusion Matrix using OMA in scaled jacket structure.

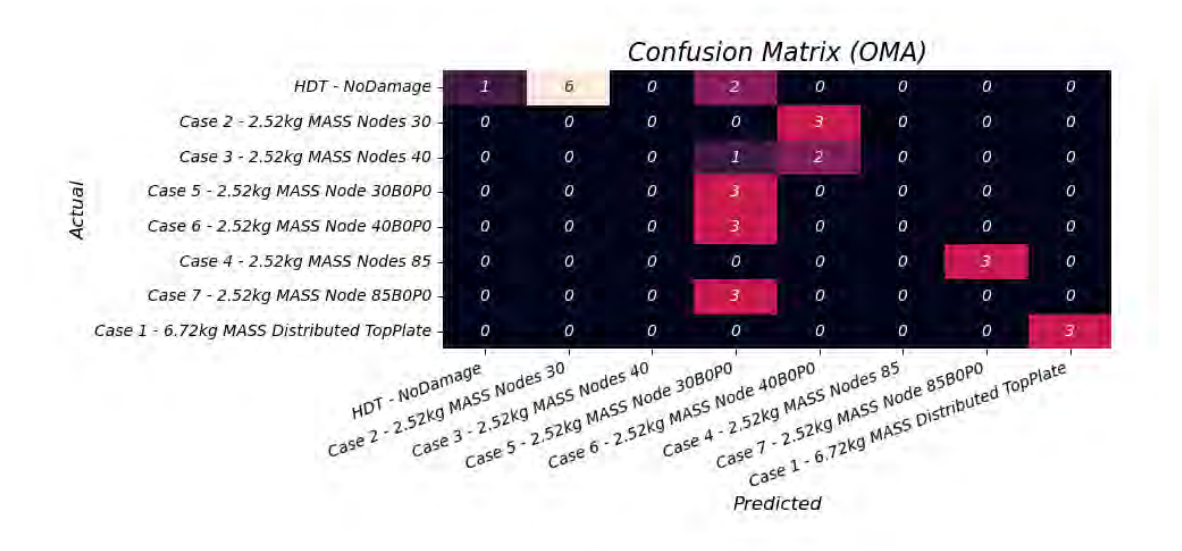


Figure 6.19: Confusion Matrix for a 2.52 kg mass using OMA in scaled jacket structure.

accuracy with and without applying the inverse coefficient of variation weights. For the scaled jacket structure, the accuracy dropped significantly from 90% to 50% when weights were not applied (the confusion matrix using no weights is shown in Subsection A.6.2). This suggests that the method without weights is not robust in complex structures, and this is likely due to boundary condition uncertainties and fabrication imprefections.

In order to evaluate the performance of the method using lower masses, a 2.52 kg mass is used instead of the 5.02 kg mass. A 2.52 kg mass represents 5% of the total weight of the structure and produces an average relative frequency difference of 3.6%. If this mass is used instead of the 5.02 kg mass and the confusion matrix (using weights) is plotted again (Figure 6.19), it can be seen that the accuracy of the method drops to 23.3%, which is by no means acceptable. Therefore, it is concluded that the method performs well when the "damage" produces an average relative change in frequency of at least 6.3%.

# 7 Discussion

This study investigated the feasibility of using a Digital Twin (DT) for Structural Health Monitoring (SHM) and damage detection in offshore jacket foundations. The approach combined numerical modeling via FEM and experimental methods, such as Experimental Modal Analysis (EMA) and Operational Modal Analysis (OMA), to validate and enhance the reliability of the proposed damage detection strategy.

This chapter is organized as follows: First, a comparative assessment between EMA and OMA is presented. Subsequently, a discussion of the impact of assumptions made in the FE models, and finally the performance of the digital twin and the damage detection method is addressed.

## 7.1 Comparative assessment between EMA and OMA

Both EMA and OMA provided consistent natural frequencies and mode shapes. However, the determination of damping ratios using OMA showed significant inaccuracy, making it unsuitable as a parameter for damage detection. Therefore, since the method relied only on natural frequencies and mode shapes, there was no clear benefit from using EMA. If damping ratios are to be included in the analysis, EMA is preferred. Overall, EMA exhibited slightly higher precision due to its controlled excitation conditions, while OMA proved advantageous for its simplicity and relevance to in-situ monitoring scenarios.

As described in [31], modal parameters identified using OMA are influenced by environmental conditions. The reliability of the SHM system thus depends on its ability to distinguish between changes in modal parameters caused by environmental factors and those due to structural damage. This could be addressed by correcting modal properties using an environmental model that incorporates parameters such as air temperature, wind speed and direction, wave amplitude, and wave frequency.

Furthermore, the presence of two closely spaced modes in the scaled jacket structure posed a challenge for OMA. Consequently, the performance of the HDT (Subsection 6.2.3) (together with other reasons) was not as good as that of the three-story frame structure. However, the HDT was still sufficiently accurate in this early phase of the method, where only external masses were introduced as damage.

# 7.2 Impact of assumptions made in FE models

In general, the three-story frame structure involved fewer uncertainties in its boundary conditions and constraints than the scaled jacket, as the former was reasonably assumed to have fully fixed supports and rigid column-to-floor connections. While this assumption was not entirely accurate, it was easily adjusted in the model updating process by tuning the Young's modulus of the columns, as shown in Subsection 6.1.3. Furthermore, as demonstrated in Subsection 4.1.1, it was important to account for geometric stiffness due to the low moment of inertia of the columns. Neglecting this leads to overestimated stiffness. In this case, incorporating geometric stiffness caused a shift of 11.5% in the first natural frequency, and therefore geometric stiffness should never be ignored in low-inertia columns.

In the scaled jacket structure, geometric stiffness played no significant role due to the absence of a superstructure. However, the primary challenges lied in the boundary conditions, joints, and connections. Because the scaled jacket could not be mounted on a

strong floor when performing dynamics tests, achieving fixed or simply supported conditions proved to be difficult. Instead, the structure was first placed on a strong table, which produced satisfactory results in the model update but with a low performance in the damage detection method due to coupling effects between the strong table and the scaled jacket. As a consequence, the structure was removed from the strong table and the mounting conditions presented in Section 3.3 were adopted, which showed better performance during model update and in the damage detection method. Moreover, although the current experimental boundary conditions using neoprene pads introduced some compliance that is difficult to characterize numerically, it is shown to be an advantage when the structure is moved to a cold chamber for future tests in cold climate conditions (which was the main goal when the structure was designed).

Furthermore, the joints in the scaled jacket were modeled as fully rigid, which did not reflect real behavior due to weld flexibility. To compensate, the Young's modulus of the braces was adjusted accordingly (as described in Subsection 6.2.3). Additional uncertainties arose from minor fabrication imperfections in the legs, braces, and transition piece, such as misalignments and non-ideal welds.

## 7.3 Performance of the digital twin

This section presents some discussion about the results and performance of the digital twin of both structures, namely the three-story frame structure and the scaled jacket.

## 7.3.1 Three-story frame structure

When the results of the undamaged tests of the three-story frame structure were compared to the HDT (Subsection A.5.1), the maximum relative frequency differences for the first, second, and third modes were 0.34%, 0.14%, and 0.16%, respectively. Additionally, the lowest MAC values for these modes were 0.9925, 0.9989, and 0.9978, respectively. This demonstrates that the HDT replicated the behavior of the real structure with high fidelity.

When the results of the damaged tests of the three-story frame structure were compared to the corresponding DDT (Subsection A.5.1), the maximum relative frequency differences showed values of 1.6%, 1.1%, and 1.5% for the first, second, and third modes, respectively, and the lowest MAC values were 0.9845, 0.9978, and 0.9974.

In summary, the DT performed nearly identically to the real structure in terms of modal properties, and there is limited room for further improvement in the DT.

### 7.3.2 Scaled jacket structure

When the results of the undamaged OMA-based tests of the scaled jacket were compared to the HDT (Subsection A.5.2), the bending mode in the Y-direction and the torsional mode showed excellent agreement, with a maximum relative frequency difference of approximately 1%. However, the X-direction bending mode showed a larger deviation of about 4%. Moreover, MAC values for both bending modes were approximately 0.94, and around 0.998 for the torsional mode. Despite these discrepancies, the HDT was sufficiently accurate to differentiate between damaged and undamaged states.

When the results of the damaged OMA-based tests of the scaled jacket were compared to the corresponding DDT (Subsection A.5.2), the maximum relative frequency differences showed deviations of approximately 4% for the bending modes and 7.7% for the torsional mode. Additionally, the lowest MAC values were 0.86 (X-bending), 0.88 (Y-bending), and 0.98 (torsional).

In general, the DT did not replicate the exact behavior of the real structure, which could be attributed to the challenges outlined in Section 7.2. Thus, there is considerable room for improving the fidelity of the scaled-jacket's digital twin.

## 7.4 Performance of the damage detection method

The damage detection method for the three-story frame structure presented in Subsection 6.1.4 achieved an accuracy of 97% using EMA and 93.3% using OMA for a simulated damage (added mass) that produced an average relative frequency difference of 2.5%. The approach based on weighted Euclidean distance (using  $\delta_f$  and  $\delta_{MAC}$ ) proved effective. The weighting based on coefficients of variation allowed better sensitivity to features with higher confidence. When weighting was not considered, the accuracy shifted to 90%, suggesting that the method is naturally robust (less sensitive to weighting) in simple structures. Although this method is simple, it showed robust results in the three-story frame structure and it has the benefit of transparency and interpretability compared to complex neural network approaches. Furthermore, smaller masses are believed to still be detected with acceptable accuracy. A logical next step would be to apply the method to other types of damage that result in a similar frequency change and evaluate its ability to distinguish between them.

For the scaled jacket structure (Subsection 5.2.5), the method using weights achieved 90% accuracy using OMA for a damage scenario (added mass) that induced an average relative frequency difference of 6.3%. However, when weighting was not considered, the accuracy dropped to 50%, suggesting that the method without weighting is not robust in the scaled jacket structure. This is attributed to the mounting conditions and fabrication imperfections that are difficult to model in a FE model. The result also demonstrated that the weighting scheme in complex structures mitigates the effect of unreliable features and leads to more stable and trustworthy damage predictions.

Furthermore, for a smaller mass that produced only a relative frequency difference of 3.6%, the accuracy of the method dropped to unacceptable levels. Therefore, under the current boundary conditions, a minimum average frequency shift of approximately 6% appears to be necessary for the method to function reliably.

In addition, the method performed successfully even when the symmetry was broken (e.g., Figure 3.11c), and it is also capable of predicting concentrated damage. Therefore, the method shows good potential for application in cases where the dynamic properties of the RNA are included, and localized damage (such as cracks) needs to be detected.

In conclusion, the performance of the damage detection method for the scaled jacket can be significantly improved if the boundary conditions are better represented in the FE model. One potential improvement is to relocate the structure to a strong floor, where well-defined support conditions (fixed or simply supported) can be realistically implemented. This would reduce the uncertainty associated with the current boundary conditions, improve the performance of the model updating, and consequently, the accuracy of the damage detection method.

# 8 Conclusion

This project has investigated the design and dynamic properties of a scaled jacket using digital twin, which is capable of detecting damages based on SHM system utilizing straightforward, existing tools. Through a combination of experimental testing (EMA and OMA), Finite Element Model Updating (FEMU), Digital Twin (DT), and damage classification via modal features, the study demonstrated a methodology that balances simplicity, interpretability, and accuracy.

Two structures were studied: a laboratory-scale three-story frame and a 1:50 scaled offshore jacket model. Each structured played a crucial role in verifying different aspects of the method.

Modal properties of the structures were obtained using EMA and OMA and it was shown that although EMA exhibited slightly higher precision, the damage detection method did not improve considerably. Moreover, for large structure OMA is preferred due to its simplicity and relevance to in-situ monitoring scenarios.

One of the challenges of this study was to set a proper boundary condition in the FE model of the scaled jacket structure that represented the supports of the real structure. Moreover, there are uncertainties due to fabrication imperfections that are difficult to predict and model in numerical software. However, some of the uncertainties described above were diminished when model updating was performed.

A simple yet effective damage detection algorithm was implemented, based on computing Euclidean distances between feature vectors containing relative frequency differences  $(\delta_f)$  and deviations in mode shapes  $(\delta_{MAC})$ . The use of coefficient-of-variation-based weighting allowed better handling of uncertainty in modal identification, particularly in the scaled jacket structure. This algorithm achieved 90–97% classification accuracy, depending on the structure and test method.

The approach developed in this thesis is characterized by its simplicity and low computational cost. Unlike black-box machine learning models that require extensive training and offer limited transparency, this method is based on physical understanding and interpretable metrics.

### 8.1 Further work

This project has provided valuable information on damage detection in offshore wind applications. However, several aspects require further development and exploration. This section briefly discusses different methodological considerations and outlines potential directions for future research.

Impact hammer testing provides reliable results, but is not time-efficient and requires a lot of effort when the number of tests increases. Therefore, in future studies, a more effective exciter should be considered.

In addition, in the early stages of the thesis, other types of damage were considered and designed, such as removable legs and braces, and scour representation using vibration isolation mounts. However, due to time constraints, these damages were not manufactured. In addition, more diverse damages could be included in future work, such as cracks and defects in welds. Including several types of damage will push the method to the limit,

and it would be possible to realize if it has some potential applicability in real offshore jacket foundations.

Furthermore, it is well known that the mass and moment of inertia of the RNA have an influence on the modal properties, as they are no longer rotationally symmetric around the tower. Consequently, conducting similar tests with a representation of the tower and the RNA is essential to provide additional data that can support the development of the current approach.

Last but not least, identification of local modes in the braces would be beneficial if damages are included in the braces. However, this would require more accelerometers installed in the structure, which might be impractical in real offshore applications.

## References

- [1] H. Nahvi and M. Jabbari. "Crack detection in beams using experimental modal data and finite element model". In: *International Journal of Mechanical Sciences* 47 (2005).
- [2] D. Tcherniak, S. Chauhan, and M.H. Hansen. "Applicability Limits of Operational Modal Analysis to Operational Wind Turbines". In: Structural Dynamics and Renewable Energy. 2011.
- [3] N. Stubbs, C. Farrar, and J. Kim. "Field Verification of a Nondestructive Damage Localization and Severity Estimation Algorithm". In: *Proceedings of the 13th International Modal Analysis Conference, Vols 1 and 2.* 1995.
- [4] W.N. Wandji. "Rayleigh's quotient–based damage detection algorithm: Theoretical concepts, computational techniques, and field implementation strategies". In: *Structural Health Monitoring*. 2018.
- [5] M. Pastor, M. Binda, and T. Harcarik. "Modal assurance criterion". In: *Procedia Engineering*. 2012.
- [6] A. Rytter. Vibrational based inspection of civil engineering structures. Dept. of Building Technology and Structural Engineering, Aalborg University, 1993.
- [7] W. Kritzinger et al. "Digital Twin in manufacturing: A categorical literature review and classification". In: *Ifac-papersonline*. 2018.
- [8] U. T. Tygesen et al. "The true digital twin concept for fatigue re-assessment of marine structures". In: Proceedings of the International Conference on Offshore Mechanics and Arctic Engineering Omae. 2018.
- [9] D. Augustyn et al. "Data-driven model updating of an offshore wind jacket substructure". In: Zenodo (cern European Organization for Nuclear Research) (2020).
- [10] G. Oliveira et al. "Vibration-based damage detection in a wind turbine using 1 year of data". In: *Structural Control and Health Monitoring* (2018).
- [11] M. Richmond, U. Smolka, and A. Kolios. "Feasibility for damage identification in offshore wind jacket structures through monitoring of global structural dynamics". In: *Energies* (2020).
- [12] Z. Mousavi et al. "A digital twin-based framework for damage detection of a floating wind turbine structure under various loading conditions based on deep learning approach". In: *Ocean Engineering* (2024).
- [13] Z. Mousavi et al. "Deep neural networks—based damage detection using vibration signals of finite element model and real intact state: An evaluation via a lab-scale offshore jacket structure". In: Structural Health Monitoring (2021).
- [14] A. Brandt. Noise and Vibration Analysis: Signal Analysis and Experimental Procedures. 2nd Edition. Wiley, 2023.
- [15] M. T. Steffensen, Tcherniak D., and Thomsen J. J. "Uncertainty in frequency response function estimates in experimental modal analysis". In: *Journal of Sound and Vibration* (2025).
- [16] Brüel & Kjær Sound & Vibration Measurement. *Modal Testing and Analysis*. Lecture Notes and Multimedia Presentation from B&K, 2000.
- [17] R. Brincker and C. Ventura. *Introduction to Operational Modal Analysis*. John Wiley & Sons, 2015.
- [18] Kvåle K. A., O. Øiseth, and A. Rönnquist. "Covariance-driven stochastic subspace identification of an end-supported pontoon bridge under varying environmental con-

- ditions". In: Conference Proceedings of the Society for Experimental Mechanics Series. 2017.
- [19] Wikipedia. "Pearson correlation coefficient". URL: https://en.wikipedia.org/wiki/ Pearson\_correlation\_coefficient (visited on 04/23/2025).
- [20] Wikipedia. "Spearman's rank correlation coefficient". URL: https://en.wikipedia.org/wiki/Spearman%27s\_rank\_correlation\_coefficient (visited on 04/10/2025).
- [21] ANSYS Inc. DesignXplorer Optimization Tutorials. 2021.
- [22] S. Selvakumar and R. Ravikumar. "A Novel Approach for Optimization to Verify RSM Model by Using Multi-Objective Genetic Algorithm (MOGA)". In: *International Conference on Materials Manufacturing and Modelling* (2018).
- [23] P. Avitabile. *Experimental modal analysis. A simple non-mathematical presentation*. University of Massachussetts Lowell.
- [24] M.W. Trethewey and J.A. Cafeo. "Tutorial: Signal processing aspects of structural impact testing". In: *The International Journal of Analytical and Experimental Modal Analysis* (1992).
- [25] SciPy Community. *SciPy module*. 2025. URL: https://docs.scipy.org/doc/scipy/index.html (visited on 02/17/2025).
- [26] Janko Slavič, Klemen Zaletelj, and Domen Gorjup. *SDyPy module*. 2024. URL: https://github.com/sdypy/sdypy (visited on 02/29/2024).
- [27] D. Pasca. *pyOMA2 module*. 2024. URL: https://pyoma.readthedocs.io/en/main/ (visited on 03/17/2025).
- [28] S. Pontow et al. *Design Solution for a Support Structure Concept for future 20MW*. Tech. rep. INNWIND.EU, 2017.
- [29] B.T. Svendsen. *The evaluation of damage detection and structural health monitoring for integrity management of offshore structures*. Tech. rep. Ramboll, 2022.
- [30] S. Krenk and J. Høgsberg. Statics and Mechanics of Structures. Springer, 2013.
- [31] Z. Chen et al. "Modal Parameter Identification of Jacket-Type Offshore Wind Turbines Under Operating Conditions". In: *Journal of Marine Science and Engineering* (2024).

# A Appendices

### A.1 Equipment documentation

### A.1.1 Accelerometers: Brüel & Kjær 4507-B

### PRODUCT DATA

#### Piezoelectric Accelerometer Types 4507 and 4508

Accelerometer families that include both CCLD and charge variants

This family of small ThetaShear accelerometers is perfect for structural analysis applications. Each accelerometer has a lightweight titanium housing with an integrated 10–32 UNF coaxial connector, which is located on either the top (Type 4508 family) or the side (Type 4507 family). Types 4507 and 4508 are available in charge or CCLD\* versions, and CCLD variants are equipped with TEDS (transducer electronic datasheet).

CCLD variants have an engraved data matrix code for use with the Brüel & Kjær app for multichannel test set up: Transducer Smart Setup.

#### CCLD accelerometers offer the following advantages:

- · Connect directly to power supply
- Use inexpensive cables
- Use long cables
- >100 dB dynamic range
- Sensitivities from 10 mV/g to 1 V/g
- Hermetic connector

#### Charge accelerometers offer the following advantages:

- Sensitivity of 5 pC/g
- Operating temperature up to 250 °C (482 °F)

#### **Uses and Features**

#### Uses

- · Structural analysis measurements
- Multichannel measurements
- General purpose

# Features

- · Titanium housing
- Integrated titanium connector with hermetic sealing
- Excellent low-frequency response
- · Low sensitivity to RF (radio frequency) electromagnetic fields
- Low magnetic sensitivity
- ThetaShear design providing:
  - High sensitivity-to-weight ratio
  - Low sensitivity to environmental factors
- · Mounting clips (for most variants)
- Triaxial mounting facility
- Engraved data matrix codes (on CCLD variants with TEDS only)

<sup>\*</sup> CCLD: Constant current line drive, also known as DeltaTron® (ICP® and IEPE compatible)





### Specifications - CCLD Accelerometer Type 4507 Family (side connector)

Type Number		4507-B	4507-B-003	4507-B-004	4507-B-001	4507-B-002	4507-B-005	4507-B-006
General								
W-12.LZ	gram	4.8	4.9	4.6	4.8	4.8	4.6	4.6
Weight	oz	0.17	0.17	0.16	0.17	0.17	0.16	0.16
Voltage Sensitivity	mV/ms <sup>-2</sup>		10 ± 5%		1±5%	100	± 10%	50 ± 5%
(at 159.2 Hz, 4 mA supply current)	mV/g		98 ± 5%		9.8 ± 5%	980 :	± 10%	490 ± 5%
Amplitude (±10%)	700		0.3 to 6000		0.1 to 6000	0.4 to	6000	0.2 to 6000
Frequency Range Phase (±5°)	Hz		2 to 5000		0.5 to 5000	2 to	5000	1 to 5000
Mounted Resonance Frequency	kHz		18		18	1	8	18
Max. Transverse Sensitivity (at 30 Hz, 100 ms-2)	%		<5		<5		5	<5
Transverse Resonance Frequency	kHz		>18		>18	>	18	>18
Max Operational Continuous Sinusoidal	kms <sup>-2</sup>		0.7		7	0.	07	0.14
Acceleration (± peak)	g		70		700		7	14
TEDS			Yes		Yes	Y	es	Yes
Electrical								
Bias Voltage (at full temp. and curr. range)	V		13 ± 1		13 ± 1	13	±2	13 ± 2
Constant current	mA		2 to 20		2 to 20	2 to	20	2 to 20
Power Supply Unloaded supply voltage	V		24 to 30*		24 to 30*	24 t	o 30 <sup>*</sup>	24 to 30*
Output Impedance	Ω		30		30	3	10	30
Start-up time (to final bias ± 10%)	s		<5		<50	<	5	<5
Residual Noise (inherent rms broadband noise in	μV		<35		<8	<1	150	<80
the specified frequency range)	ца		<350		<800	<1	150	<160
10 Hz			0.15 (15)		0.25 (25)	0.0	8 (8)	0.08 (8)
Noise (spectral) 100 Hz	mms <sup>-2</sup> /√Hz		0.035 (3.5)		0.06 (6)		2 (2)	0.02(2)
1000 Hz	(μg/√Hz)		0.02 (2)		0.035 (3.5)		1(1)	0.01(1)
Environmental			3.55 (4)		5.55 2.75.57		- 1-1	
	°C		-54 to +121		-54 to +121	-54 to	+100	-54 to +100
Operating Temperature Range	°F.		-65 to +250		-65 to +250		+212	-65 to +212
Temperature Coefficient of Sensitivity	%/°C		0.09		0.09		18	0.18
	ms <sup>-2</sup> /°C		0.2		0.2		2	0.2
Temperature Transient Sensitivity  3 Hz Lower Limiting Freq. (–3 dB, 6 dB/octave)	g/°F		0.011		0.011		011	0.011
, , , , , , , , , , , , , , , , , , ,	ms <sup>-2</sup> /T		3		3		3	3
Magnetic Sensitivity (50 Hz, 0.038 T)	g/kG		0.03		0.03		03	0.03
	ms <sup>-2</sup> /με		0.005		0.005		05 <sup>†</sup>	0.005
Base Strain Sensitivity (at 250 με in base plane)	g/µE	-	0.005 <sup>†</sup>		0.005	(4)	005 <sup>†</sup>	0.0005 <sup>†</sup>
	kms <sup>-2</sup>		50		1000	-	60	50
Max. Non-destructive Shock (± peak)			5000		5000		000	5000
Mechanical	g	-	2000		3000	3.	100	3000
Case Material		_		Tibne	nium ASTM Gr	oda 1		
			חל כם	Illai			27	07.27
Piezoelectric Sensing Element			PZ 23	_	PZ 23	PZ	.27	PZ 27
Construction					ThetaShear			
Sealing				, etc0	Hermetic	20		
Electrical Connector					le, 10-32 UNF			-
Mounting Slots (pairs)		1	0	3	1	1	3	.3

<sup>\*</sup> Min. +18 V DC (reduced measuring range)

Note: All values are typical at 25 °C (77 °F), unless measurement uncertainty is specified. All uncertainty values are specified at 2 $\sigma$ , that is, expanded uncertainty using a coverage factor of 2)

Polarity: Positive (for an acceleration in the direction of the engraved arrows)

<sup>†</sup> Mounted on adhesive tape 0.09 mm thick

### A.1.2 Impact Hammer: Brüel & Kjær 8206



Impact Hammers — Types 8206, 8206-001, 8206-002 and 8206-003

#### USES

- Impact-force measurements on small to medium structures
- Measurement of frequency response functions using impact excitation techniques
- As part of a dynamic structural testing system for modal analysis and the prediction of structural response

#### **FEATURES**

- · Four types with sensitivity from 1 to 22 mV/N
- · Ergonomic handle
- Negligible changes to dynamic properties of test structure
- · Three replaceable tips
- · Acceleration compensated

#### Description

This series of Impact Hammers has been designed to excite and measure impact forces on small to medium structures such as engine blocks, car frames and automotive components. An accelerometer (or laser velocity transducer) is used to measure the response of the structure. By using a multichannel FFT analyzer, such as the PULSE<sup>TM</sup> system, the frequency response function and mode shapes of the test structure can then be derived. Contrary to using an electrodynamic exciter, an impact hammer does not apply additional mass loading to the test object and it provides a very portable solution for excitation.

### Characteristics

The Type 8206 series feature built-in electronics and the output sensitivity is expressed in terms of voltage per unit force (mV/N or mV/lbf). The hammers also have built-in acceleration compensation that removes unwanted noise from the resonance of the hammer from the output signal. This results in a clean, smooth output signal representing the excitation in both amplitude and phase.



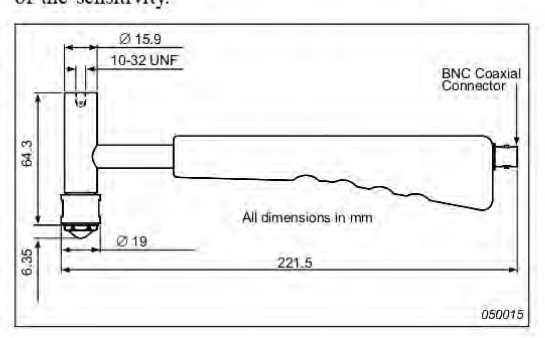
The impact hammer is supplied with three interchangeable impact tips of aluminium, plastic and rubber. The choice of impact tip determines the impulse shape (amplitude and duration) and the bandwidth of the excitation.

For increased head mass, a 40 gram head extender is available

The handle has been ergonomically designed for optimal control of impact, thus reducing the risk of "double hits".

#### Calibration

The transducer is supplied with an individual calibration of the sensitivity.



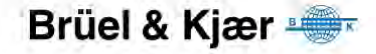
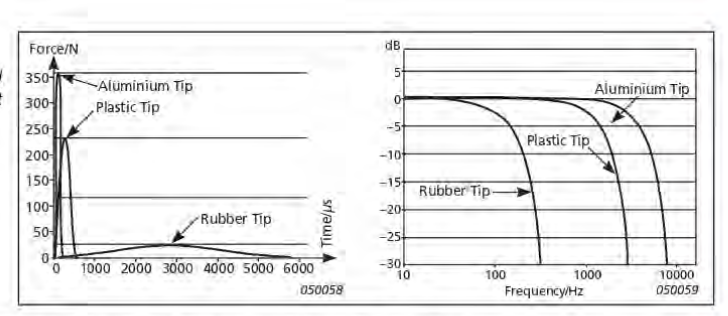


Fig. 1
Impulse shapes for the hammer tips as a
function of time showing the pulse decay and
peak value (left); Force spectrum of an impact
on an aluminium plate (right)



#### Specifications - Impact Hammers Types 8206, 8206-001, 8206-002 and 8206-003

	Units	8206	8206-001	8206-002	8206-003	
Dynamic Characteristics						
Voltage Sensitivity (typical)	mV/N (mV/lbf)	22.7 (100)	11,4 (50)	2.27 (10)	1.14 (5)	
Full Scale Force Range Compression	N (lbf)	220 (50)	445 (100)	2200 (500)	.4448 (1000)	
Linear Error at Full Scale	% full scale		<	±1		
Electrical Characteristics						
Full Scale Output Voltage	V		-	-5		
DC Output Bias Voltage	V		10	±1		
Output Impedance	Ω		<	100		
Power Supply	mA	2 to 20				
Voltage Range	V DC	+18 to +30				
Environmental Characteristics						
Temperature Range	³C (°F)		-73 to +60 (-	-100 to +140)		
Max. Force Compression	N (lbf)		4448 (1000)		8896 (2000)	
Physical Characteristics		·				
Dimensions			See outlin	ne drawing		
Overall Length	mm (in.)		221.5	(8.72)		
Effective Seismic Mass	gram (oz.)	100 (3.53)				
Sensor Housing Material		Stainless steel (17-4PH)				
Handle Material			Fibre	eglass		
Connector			В	NC:		

All values are typical at 25°C (77°F) unless measurement uncertainty is specified

#### COMPLIANCE WITH STANDARDS

Compliance with EMC Directive and Low Voltage Directive of the EU



Compliance with the EMC requirements of Australia and New Zealand

#### Ordering Information

Type 8206, 8206-001, 8206-002 and 8206-003 include:

- Impact tip of aluminium
- · Impact tip of plastic (Delrin)
- Impact tip of rubber (Polyurethane)
- Carrying box
- · Calibration chart
- Head extender (40 grams)
- PVC Insulated Cable, 70°C, 10–32 UNF to BNC Connector, 5 m (16.4 ft)
- Plug Adaptor, BNC to 10-32 UNF

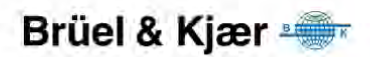
#### OPTIONAL ACCESSORIES\*

- AO0531; 70°C, Insulated single screen flexible cable, 10–32 UNF to BNC, 5 m (16.4 ft)
- JP 0145: Plug adaptor, BNC/10-32 UNF
- AO0406: Low-noise, double-screened cable, 10–32 UNF to BNC, 200°C, 5 m (16.4 ft)
- DB 3996: Head extender (40 grams) for Impact Hammer Type 8206
- UA 2059: Set of three impact tips for Type 8206 series impact hammers
- ZZ0245: In-line TEDS Adaptor, 10–32 UNF to 10–32 UNF
- \*Additional accessories and cables are available (see www.bksv.com)

Bruel & Kjær reserves the right to change specifications and accessories without notice

HEADQUARTERS: DK-2850 Nærum - Denmark - Telephone: +45 4580 0500 - Fax: +45 4580 1405 www.bksv.com - Info@ bksv.com

Australia (+61) 2 9889-8888. Austria (+43) 1 865 74 00. Brazil (+55) 11 5188-8166 · Canada (+1) 514 695-8225 China (+68) 10 680 29906 · Czech Republic (+420) 26702 1100 · Finland (+358) 9-521 300 · France (+33) 169 907 100 Germany (+49) 421 17 870 · Hong Kong (+852) 2548 7486 · Hungary (+36) 12158 905 · Fiteland (+351) 1807 4083 Italy (+39) 0257 68061 · Japan (+81) 35715 1612 · Korea (+82) 2347 30605 · Netherlands (+31) 318 55 9290 Norway (+47) 68771155 · Poland (+48) 2216756 · Potruga (+45) 2474 11453 · Singapore (+65) 377 4512 Slovak Republic (+421) 25 443 0701 · Spain (+34) 91 659 0820 · Sweden (+46) 8449 890 Switzerland (+41) 4480 7035 · Talwan (+86) 22 520 27255 · United Kingdom (+44) 14 38 739 900 USA (+1) 90 032 2400 · Local representatives and service organisations worthwide



### A.2 Documentation of jacket structure of 20 MW wind turbine

In Figure A.1, the arrow next to each element indicates its defined orientation. Each leg element consists of 4 subelements, while each brace element consists of 3 subelements. The boxes next to each element indicate its sectional properties. A "P" in front of the "Diameter x Thickness" defines a pipe section (sections with constant diameter). A "C" means that the subelement is a conical section. Note that the upper sectional property in the box denotes the first subelement, while the sectional property shown at the bottom of the box denotes the last subelement (arrow points in direction of the last element).

In Figures A.2, A.3, A.4 and A.5, the boxes next to each node indicate its ID, X-coordinate, Y-coordinate, and Z-coordinate, respectively.

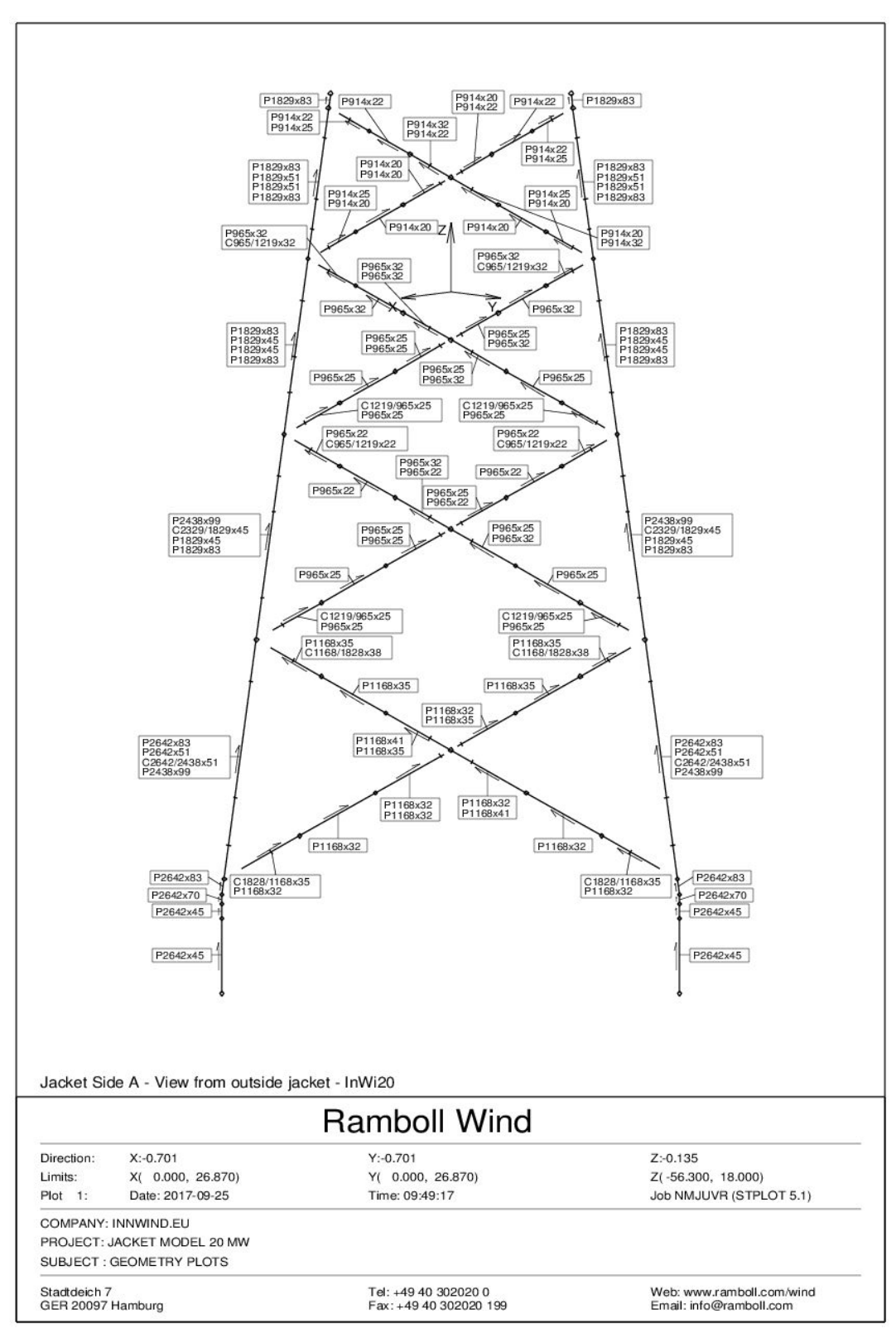


Figure A.1: Elements of jacket dimensions

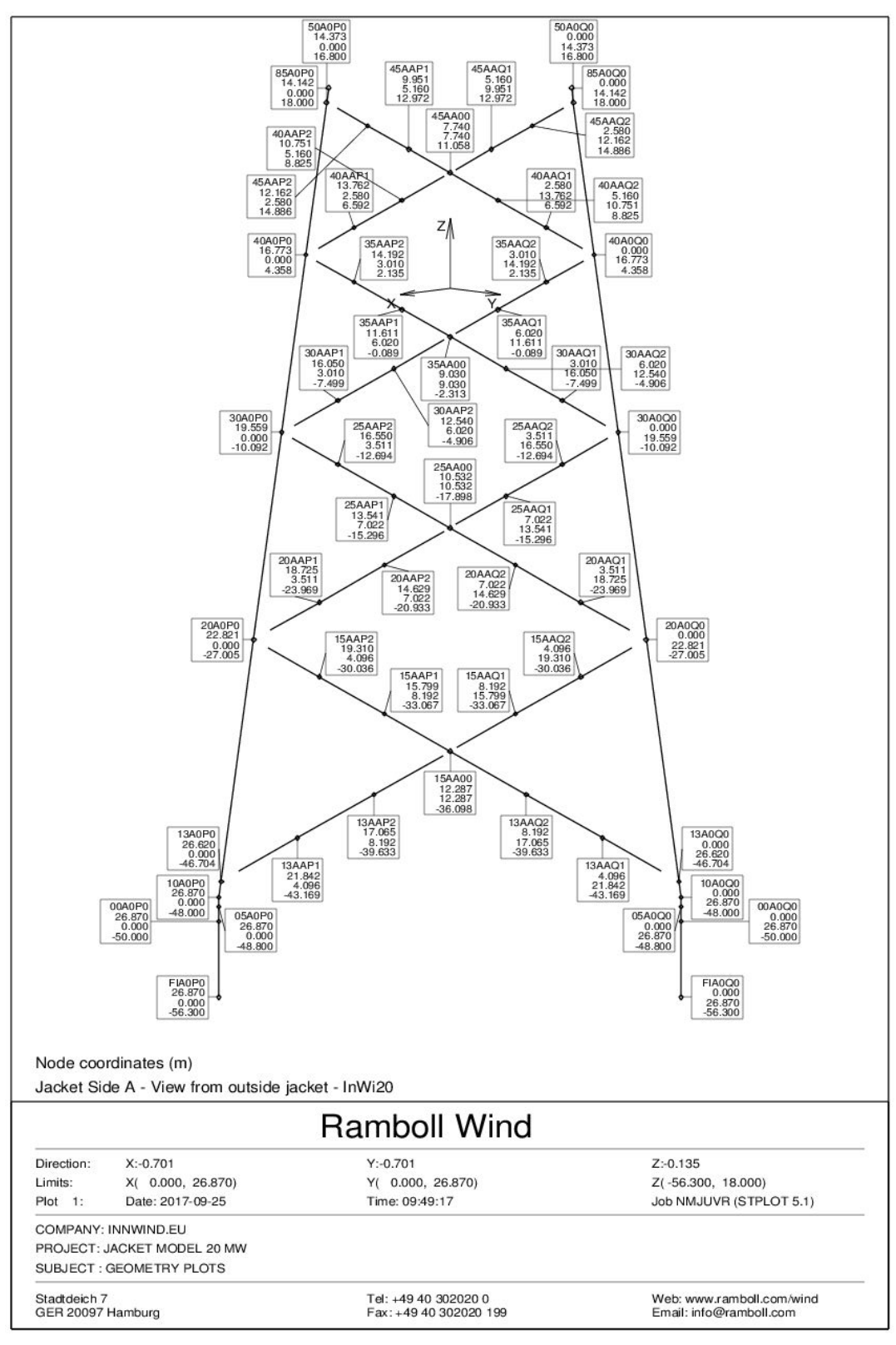


Figure A.2: Node coordinates of jacket. Side A

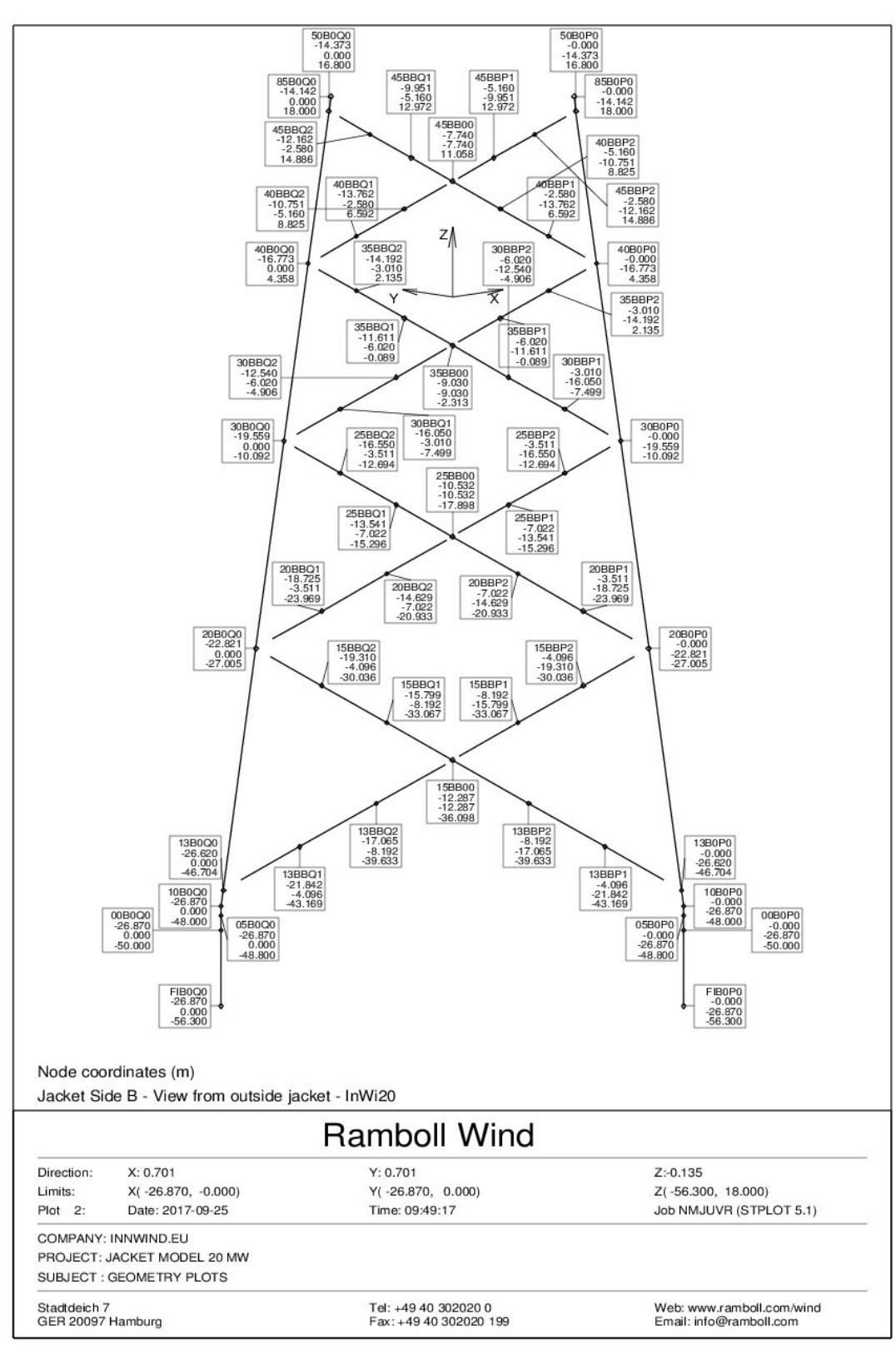


Figure A.3: Node coordinates of jacket. Side B

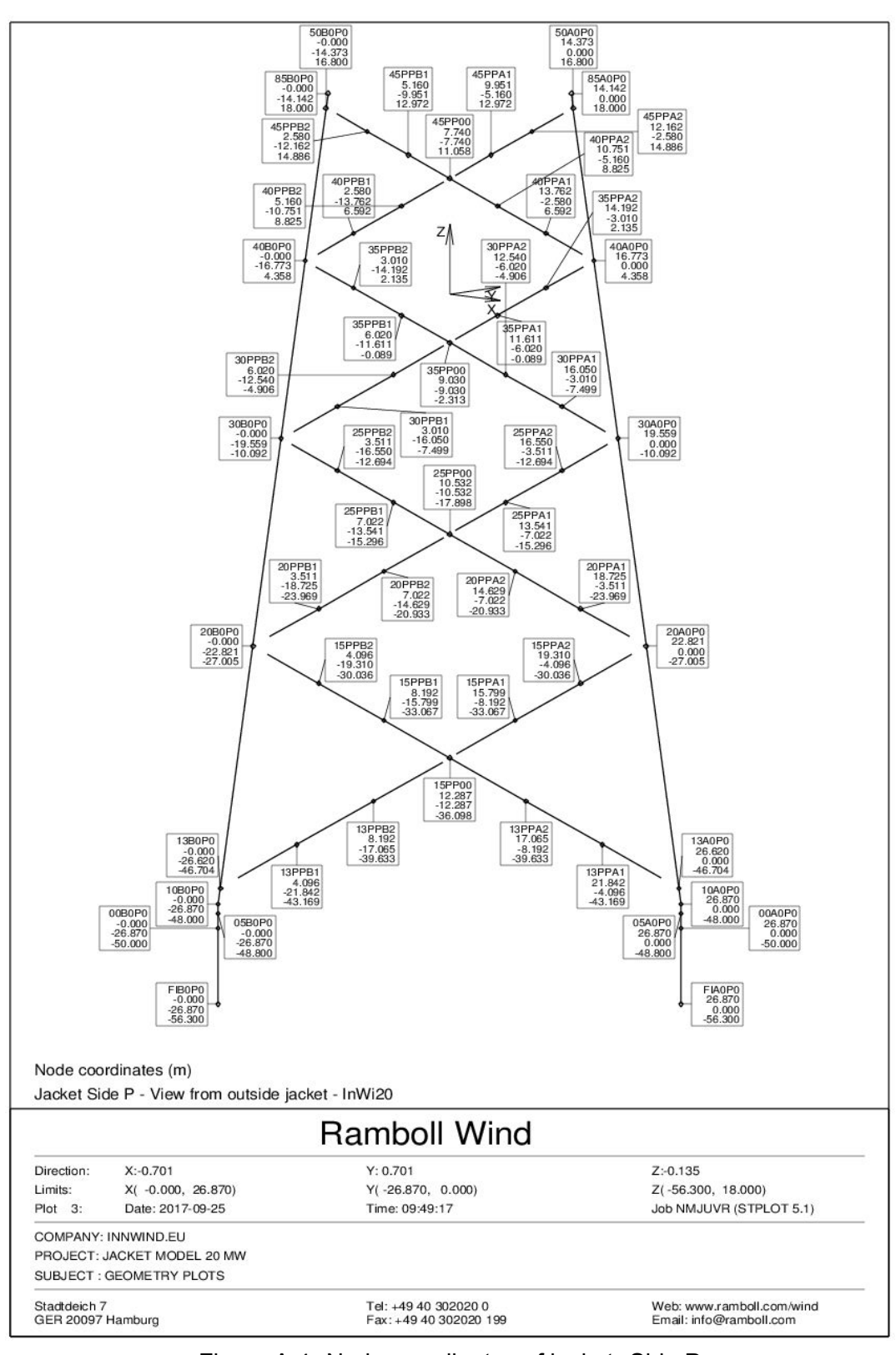


Figure A.4: Node coordinates of jacket. Side P

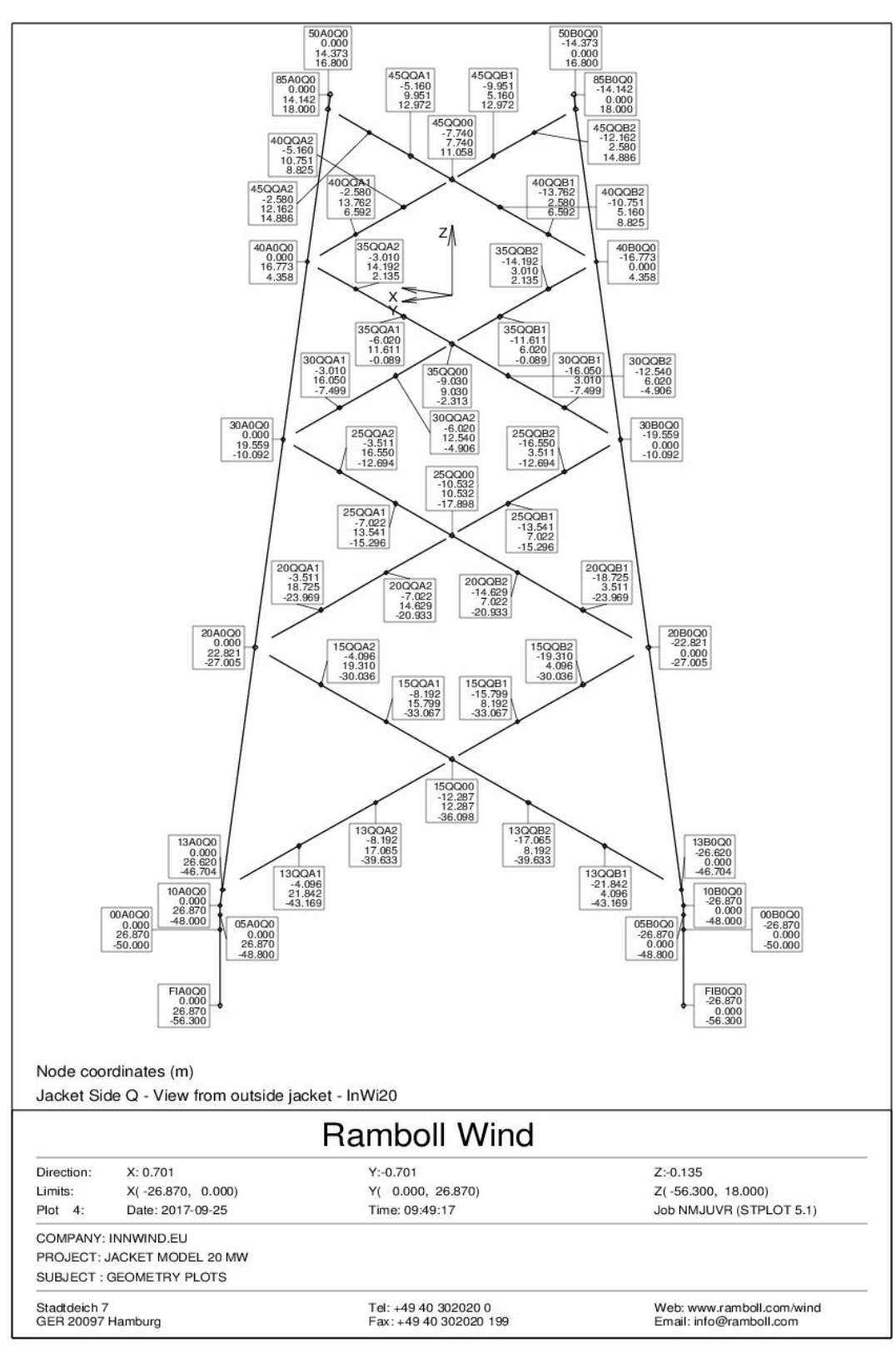
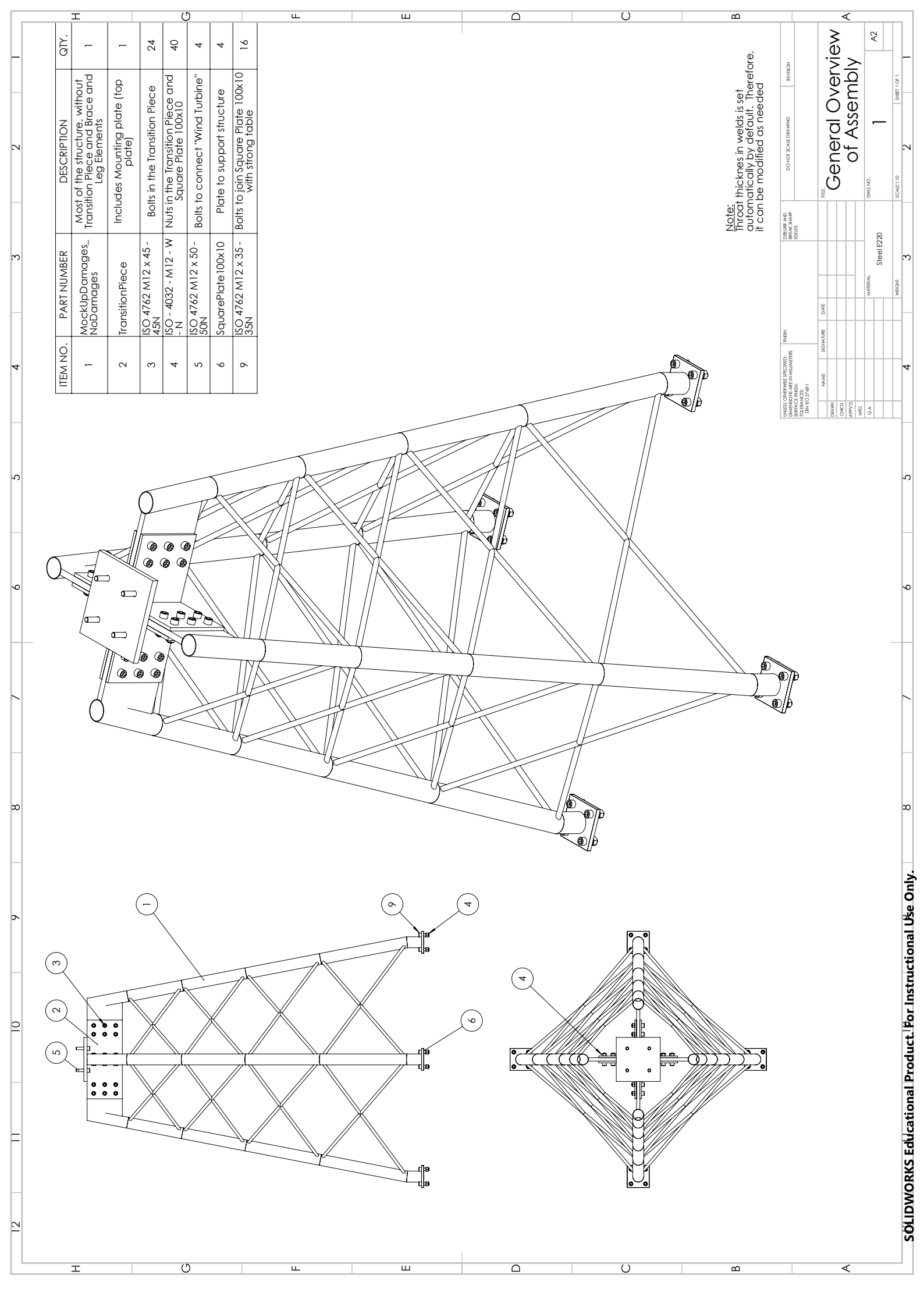
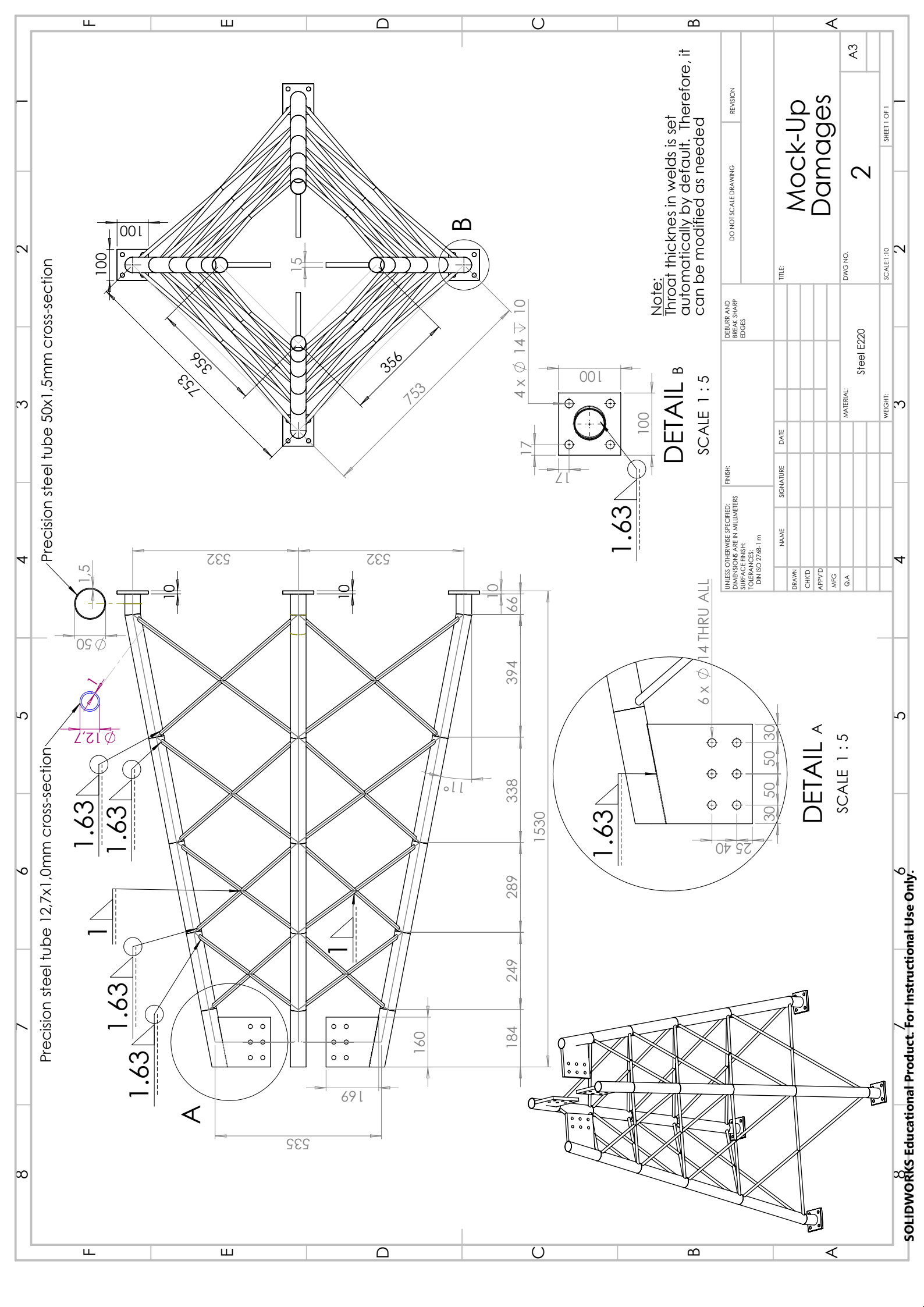
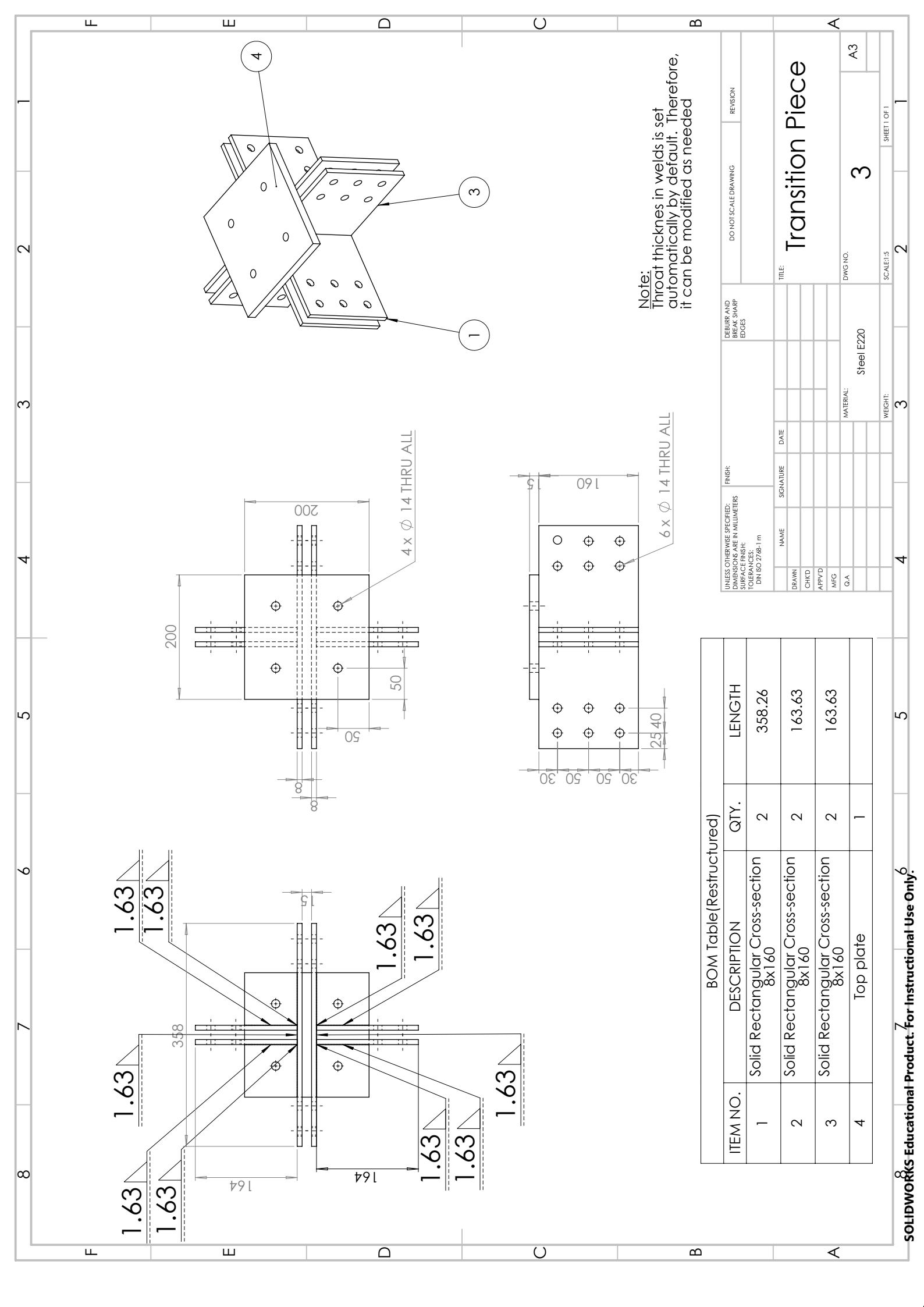


Figure A.5: Node coordinates of jacket. Side Q

# A.3 Drawings for workshop







## A.4 Results

A.4.1 Three-story Frame Structure
Natural frequencies and mode shapes of HDT and DDT for three-story frame structure

	Floor	$f_1\\[Hz]$	$f_2 \\ [Hz]$	$f_3$ $[Hz]$	$u_1$	$u_2$	$u_3$
	$m_1$				0.504	-1.099	0.696
HDT	$m_2$	1.782	5.252	7.737	0.840	-0.279	-1.078
	$m_3$				0.995	0.826	0.583
	$m_1$				0.507	-1.077	0.628
Case 1	$m_2$	1.768	5.127	7.671	0.836	-0.225	-1.094
	$m_3$				0.988	0.818	0.607
	$m_1$				0.498	-1.088	0.717
Case 2	$m_2$	1.751	5.231	7.560	0.832	-0.274	-1.022
	$m_3$				0.979	0.838	0.593
	$m_1$				0.491	-1.092	0.715
Case 3	$m_2$	1.741	5.166	7.662	0.822	-0.318	-1.081
	$m_3$				0.981	0.790	0.533
	$m_1$				0.501	-1.070	0.645
Case 4	$m_2$	1.738	5.109	7.491	0.828	-0.221	-1.039
	$m_3$				0.972	0.827	0.619
	$m_1$				0.494	-1.073	0.646
Case 5	$m_2$	1.728	5.044	7.593	0.818	-0.265	-1.098
	$m_3$				0.973	0.783	0.556
	$m_1$				0.486	-1.080	0.737
Case 6	$m_2$	1.712	5.144	7.485	0.815	-0.314	-1.025
	$m_3$				0.965	0.803	0.541
	$m_1$				0.489	-1.064	0.664
Case 7	$m_2^-$	1.700	5.025	7.413	0.811	-0.260	-1.042
	$m_3$				0.958	0.794	0.566

### Natural frequencies and mode shapes of three-story frame structure using EMA

State	Floor	$f_1$ $[Hz]$	$f_2 \\ [Hz]$	$f_3$ $[Hz]$	$u_1$	$u_2$	$u_3$
	$m_1$				0.049	-0.782	0.507
Healthy	$m_2$	1.783	5.274	7.752	0.646	-0.228	-0.776
	$m_3$				0.762	0.580	0.374
	$m_1$				-0.348	0.786	-0.515
Healthy	$m_2$	1.793	5.285	7.748	-0.495	0.211	0.772
•	$m_3$				-0.796	-0.581	-0.373
	$m_1$				0.364	0.788	-0.516
Healthy	$m_2$	1.799	5.291	7.747	0.411	0.203	0.771
	$m_3$				0.836	-0.581	-0.374
	$m_1$				0.361	0.784	0.514
Healthy	$m_2$	1.789	5.282	7.747	0.441	0.209	-0.771
	$m_3$				0.821	-0.584	0.375
	$m_1$				0.339	-0.791	0.515
Healthy	$m_2$	1.790	5.299	7.761	0.683	-0.236	-0.774
	$m_3$				0.647	0.564	0.367

	$m_1$				-0.308	0.780	0.517
Healthy	$m_2$	1.797	5.281	7.762	-0.634	0.229	-0.770
	$m_3$				-0.709	-0.581	0.374
	$m_1$				-0.352	-0.787	0.514
Healthy	$m_2$	1.797	5.295	7.759	-0.715	-0.233	-0.773
	$m_3$				-0.604	0.571	0.372
	$m_1$				0.295	-0.779	-0.507
Healthy	$m_2$	1.797	5.274	7.763	0.627	-0.241	0.778
	$m_3$				0.721	0.579	-0.370
	$m_1$				-0.307	-0.785	-0.511
Healthy	$m_2$	1.795	5.284	7.781	-0.629	-0.236	0.779
	$m_3$				-0.715	0.573	-0.363
	$m_1$				-0.151	-0.730	-0.407
38g 1st F.	$m_2$	1.780	5.146	7.729	0.672	-0.219	0.820
J	$m_3$				0.725	0.647	-0.402
	$\overline{m_1}$				-0.360	0.787	-0.471
38g 1st F.	$m_2$	1.779	5.177	7.711	-0.503	0.184	0.792
3 3	$m_3$				-0.786	-0.589	-0.388
	$\frac{m_3}{m_1}$				-0.326	-0.788	-0.472
38g 1st F.	$m_2$	1.786	5.177	7.733	-0.667	-0.205	0.795
9	$m_3$				-0.670	0.581	-0.381
	$m_1$				-0.300	0.781	-0.520
38g 2nd F.	$m_2$	1.751	5.262	7.629	-0.630	0.219	0.759
00g 2nd 1.	$m_3$	1.701	0.202	7.020	-0.716	-0.584	-0.391
	$\frac{m_3}{m_1}$				0.301	0.784	-0.524
38g 2nd F.	$m_1$	1.755	5.256	7.637	0.628	0.212	0.756
00g 2na 1.	$m_3$	1.700	0.200	7.007	0.717	-0.583	-0.391
	$\frac{m_3}{m_1}$				-0.308	0.781	0.522
38g 2nd F.	$m_1$ $m_2$	1.768	5.303	7.638	-0.635	0.229	-0.757
oog zna i .		1.700	0.000	7.000	-0.709	-0.581	0.392
	$m_3$				0.293	0.787	-0.503
38g 3rd F.	$m_1 \ m_2$	1.745	5.145	7.698	0.626	0.259	0.790
oog ord i .		1.7-10	0.140	7.000	0.722	-0.559	-0.351
	$\frac{m_3}{m_4}$				0.299	0.789	-0.521
38g 3rd F.	$m_1$	1.744	5.183	7.691	0.621	0.753	0.782
oog ord i .	$m_2$	1.777	5.105	7.001	0.725	-0.557	-0.341
	$m_3$				0.301	0.789	-0.526
38g 3rd F.	$m_1$	1.758	5.194	7.711	0.626	0.769	0.781
oog ord i .	$m_2$	1.750	J. 13 <del>7</del>	1.111	0.020	-0.554	-0.336
	$m_3$				0.719	0.782	0.480
38g 1st&2nd F.	$m_1$	1.749	5.158	7.595	0.299	0.782	-0.778
JUY TSIOZITU F.	$m_2$	1.748	5.150	า .อฮอ	0.030	-0.594	0.406
	$m_3$				0.717		
38a 1ct9 2nd E	$m_1$	1 750	5 10 <i>1</i>	7 502		0.781	-0.484 0.774
38g 1st&2nd F.	$m_2$	1.753	5.184	7.583	0.627	0.193	0.774
	$m_3$				0.718	-0.593	-0.407
00~ 4a+00~	$m_1$	4 750	E 405	7 000	0.311	0.781	0.484
38g 1st&2nd F.	$m_2$	1.759	5.185	7.603	0.635	0.193	-0.770
	$m_3$				0.707	-0.594	0.415
00-4-400 15	$m_1$	4 744	F 0 10	7.004	0.300	0.787	-0.473
38g 1st&3rd F.		1.741	5.046	7.661			

$\begin{array}{c ccccccccccccccccccccccccccccccccccc$		$m_2$				0.629	0.232	0.804
$\begin{array}{c ccccccccccccccccccccccccccccccccccc$		_						
$\begin{array}{c ccccccccccccccccccccccccccccccccccc$	-							
$\begin{array}{c ccccccccccccccccccccccccccccccccccc$	38a 1st&3rd F	-	1 747	5 091	7 640			
$\begin{array}{c ccccccccccccccccccccccccccccccccccc$	oog rotstora r	_		0.00				
$\begin{array}{c ccccccccccccccccccccccccccccccccccc$								
$\begin{array}{c ccccccccccccccccccccccccccccccccccc$	38g 1st&3rd F.	_	1.757	5.101	7.689	0.628	0.234	
$\begin{array}{c ccccccccccccccccccccccccccccccccccc$	J	_				0.713	-0.571	-0.357
$\begin{array}{c ccccccccccccccccccccccccccccccccccc$						0.293	0.784	-0.540
$\begin{array}{c ccccccccccccccccccccccccccccccccccc$	38g 2nd&3rd F.	$m_2$	1.716	5.177	7.549	0.631	0.251	0.762
$\begin{array}{c ccccccccccccccccccccccccccccccccccc$	J	$m_3$				0.718	-0.567	-0.357
$\begin{array}{c ccccccccccccccccccccccccccccccccccc$		$m_1$				0.295	-0.785	-0.541
$\begin{array}{c ccccccccccccccccccccccccccccccccccc$	38g 2nd&3rd F.	$m_2$	1.720	5.166	7.555	0.626	-0.242	0.761
$\begin{array}{c ccccccccccccccccccccccccccccccccccc$		$m_3$				0.722	0.569	-0.358
$\begin{array}{c ccccccccccccccccccccccccccccccccccc$		$m_1$				0.298	0.786	0.538
$\begin{array}{c ccccccccccccccccccccccccccccccccccc$	38g 2nd&3rd F.	$m_2$	1.710	5.208	7.547	0.628	0.261	-0.762
$\begin{array}{c ccccccccccccccccccccccccccccccccccc$		$m_3$				0.719	-0.560	0.360
$\begin{array}{c ccccccccccccccccccccccccccccccccccc$		$m_1$				0.295	0.786	-0.496
$\begin{array}{c ccccccccccccccccccccccccccccccccccc$	38g 1st,2nd&3rd F.	$m_2$	1.713	5.076	7.515	0.627	0.221	0.783
$\begin{array}{c ccccccccccccccccccccccccccccccccccc$		$m_3$				0.721	-0.577	-0.375
$\begin{array}{c ccccccccccccccccccccccccccccccccccc$		$m_1$				0.305	0.790	-0.496
$m_1$ 0.303 -0.788 -0.506 38g 1st,2nd&3rd F. $m_2$ 1.702 5.092 7.514 0.625 -0.227 0.781	38g 1st,2nd&3rd F.	$m_2$	1.712	5.089	7.502	0.621	0.214	0.783
38g 1st,2nd&3rd F. $m_2$ 1.702 5.092 7.514 0.625 -0.227 0.781		$m_3$				0.722	-0.574	-0.375
0.740 0.574 0.000		$\overline{m_1}$				0.303	-0.788	-0.506
$m_3$ 0.719 0.571 -0.366	38g 1st,2nd&3rd F.	$m_2$	1.702	5.092	7.514	0.625	-0.227	0.781
		$m_3$				0.719	0.571	-0.366

## Natural frequencies and mode shapes of three-story frame structure using OMA

State	Floor	$f_1\\[Hz]$	$f_2\\[Hz]$	$f_3$ $[Hz]$	$u_1$	$u_2$	$u_3$
	$m_1$				0.509	1.000	-0.634
Healthy	$m_2$	1.783	5.254	7.743	0.849	0.290	1.000
	$m_3$				1.000	-0.726	-0.472
	$m_1$				0.419	1.000	-0.649
Healthy	$m_2$	1.78	5.253	7.728	0.933	0.284	1.000
	$m_3$				1.000	-0.742	-0.479
	$m_1$				0.392	1.000	-0.632
Healthy	$m_2$	1.783	5.253	7.74	0.860	0.291	1.000
	$m_3$				1.000	-0.742	-0.483
	$m_1$				0.477	1.000	-0.644
Healthy	$m_2$	1.785	5.253	7.738	0.885	0.288	1.000
	$m_3$				1.000	-0.724	-0.469
	$m_1$				0.511	1.000	-0.644
Healthy	$m_2$	1.782	5.247	7.737	0.902	0.292	1.000
	$m_3$				1.000	-0.734	-0.475
	$m_1$				0.419	1.000	-0.651
Healthy	$m_2$	1.777	5.247	7.734	0.771	0.290	1.000
	$m_3$				1.000	-0.728	-0.479

	$m_1$				0.425	1.000	-0.642
Healthy	$m_2$	1.786	5.242	7.732	0.876	0.280	1.000
	$m_3$				1.000	-0.756	-0.501
	$m_1$				0.472	1.000	-0.638
Healthy	$m_2$	1.782	5.240	7.719	0.901	0.273	1.000
	$m_3$				1.000	-0.747	-0.493
	$m_1$				0.500	1.000	-0.650
Healthy	$m_2$	1.782	5.239	7.735	0.915	0.276	1.000
	$m_3$				1.000	-0.741	-0.485
	$m_1$				0.411	1.000	-0.585
38g 1st F.	$m_2$	1.780	5.140	7.730	0.865	0.261	1.000
	$m_3$				1.000	-0.777	-0.487
	$m_1$				0.406	1.000	-0.584
38g 1st F.	$m_2$	1.785	5.140	7.729	0.852	0.251	1.000
-	$m_3$				1.000	-0.755	-0.483
	$m_1$				0.716	1.000	-0.581
38g 1st F.	$m_2$	1.765	5.142	7.713	0.856	0.247	1.000
J	$m_3$				1.000	-0.772	-0.499
	$\overline{m_1}$				0.422	1.000	-0.668
38g 2nd F.	$m_2$	1.751	5.251	7.610	0.959	0.273	1.000
3 3	$m_3$				1.000	-0.743	-0.521
	$m_1$				0.445	1.000	-0.678
38g 2nd F.	$m_2$	1.758	5.250	7.597	0.845	0.275	1.000
009 =	$m_3$	00	0.200		1.000	-0.740	-0.529
	$\frac{m_3}{m_1}$				0.418	1.000	-0.681
38g 2nd F.	$m_2$	1.756	5.246	7.580	0.907	0.264	1.000
00g <u>2</u> 110 1 .	$m_3$	1.700	0.2.10	7.000	1.000	-0.758	-0.536
	$\frac{m_3}{m_1}$				0.434	1.000	-0.653
38g 3rd F.	$m_1$	1.743	5.174	7.675	0.962	0.322	1.000
oog ord it.	$m_3$	1.7 10	0.17 1	7.070	1.000	-0.703	-0.431
	$\frac{m_3}{m_1}$				0.449	1.000	-0.656
38g 3rd F.	$m_1$ $m_2$	1.746	5.171	7.658	0.927	0.329	1.000
oog ord r.		1.740	0.171	7.000	1.000	-0.693	-0.436
	$\frac{m_3}{m_4}$				0.405	1.000	-0.658
38g 3rd F.	$m_1$	1.733	5.147	7.661	0.807	0.316	1.000
Jog Jiu i .	$m_2$	1.755	J. 1 <del>7</del> 1	7.001	1.000	-0.724	-0.451
	$\frac{m_3}{m_1}$				0.461	1.000	-0.606
38g 1st&2nd F.	$m_1$	1.736	5.141	7.582	0.987	0.231	1.000
Jog Tstazna i .	$m_2$	1.750	J. 1 <del>-7</del> 1	1.302	1.000	-0.756	-0.525
	$m_3$						
38g 1st&2nd F.	$m_1$	1 7//	5.154	7 560	0.422	1.000	-0.617 1.000
Joy ISIAZIIU F.	$m_2$	1.744	5. 15 <del>4</del>	7.568	0.940	0.238	1.000
	$m_3$				1.000	-0.740	-0.519
38a 1c+2 2nd □	$m_1$	1 727	5 12O	7 570	0.415	1.000	-0.610 1.000
38g 1st&2nd F.	$m_2$	1.737	5.130	7.572	0.824	0.227	1.000
	$m_3$				1.000	-0.782	-0.548
200 1040 254 5	$m_1$	1 750	E 050	7 6 4 4	0.450	1.000	-0.602
38g 1st&3rd F.	$m_2$	1.758	5.059	7.641	0.970	0.286	1.000
	$m_3$				1.000	-0.721	-0.436
00 m 4 c t 0 0 m -1 . F	$m_1$	4 750	E 000	7.047	0.445	1.000	-0.600
38g 1st&3rd F.		1.752	5.060	7.647			

	$m_2$				0.886	0.287	1.000
	$m_3$				1.000	-0.718	-0.444
	$m_1$				0.395	1.000	-0.603
38g 1st&3rd F.	$m_2$	1.731	5.045	7.603	0.914	0.281	1.000
	$m_3$				1.000	-0.744	-0.454
	$m_1$				0.451	1.000	-0.698
38g 2nd&3rd F.	$m_2$	1.713	5.171	7.52	0.861	0.306	1.000
	$m_3$				1.000	-0.711	-0.476
	$m_1$				0.449	1.000	-0.695
38g 2nd&3rd F.	$m_2$	1.707	5.162	7.521	0.954	0.308	1.000
	$m_3$				1.000	-0.707	-0.480
	$m_1$				0.377	1.000	-0.705
38g 2nd&3rd F.	$m_2$	1.714	5.156	7.527	0.861	0.298	1.000
	$m_3$				1.000	-0.738	-0.484
	$m_1$				0.460	1.000	-0.631
38g 1st,2nd&3rd F.	$m_2$	1.699	5.058	7.523	0.964	0.266	1.000
	$m_3$				1.000	-0.730	-0.492
	$m_1$				0.441	1.000	-0.631
38g 1st,2nd&3rd F.	$m_2$	1.702	5.075	7.497	0.773	0.276	1.000
	$m_3$				1.000	-0.731	-0.478
	$m_1$				0.454	1.000	-0.623
38g 1st,2nd&3rd F.	$m_2$	1.702	5.049	7.496	0.932	0.263	1.000
	$m_3$				1.000	-0.739	-0.504

A.4.2 Scaled Jacket Structure
Natural frequencies and mode shapes of HDT and DDT for scaled jacket structure

	Accelerometer	$f_X \ [Hz]$	$f_Y \ [Hz]$	$f_T \ [Hz]$	$u_X$	$u_Y$	$u_T$
	X-dir. HalfHeight (ch.1)				-0.069	0.008	-0.138
	X-dir. TP1 (ch.2)				-0.161	0.019	-0.245
HDT	X-dir. TP2 (ch.3)	13.186	13.184	142.80	-0.161	0.019	0.244
וטח	Y-dir. HalfHeight (ch.4)	13.100	13.104	142.00	0.008	0.069	0.138
	Y-dir. TP3 (ch.5)				0.020	0.162	0.250
	Y-dir. TP4 (ch.6)				0.020	0.162	-0.250
	X-dir. HalfHeight (ch.1)				-0.063	0.007	0.134
	X-dir. TP1 (ch.2)				-0.148	0.017	0.230
0 1	X-dir. TP2 (ch.3)	40.070	10.071	400.40	-0.148	0.017	-0.235
Case 1	Y-dir. HalfHeight (ch.4)	12.072	12.071	139.42	0.007	0.063	-0.133
	Y-dir. TP3 (ch.5)				0.017	0.148	-0.236
	Y-dir. TP4 (ch.6)				0.017	0.148	0.239
	X-dir. HalfHeight (ch.1)				-0.067	0.008	-0.145
	X-dir. TP1 (ch.2)				-0.158	0.020	-0.218
	X-dir. TP2 (ch.3)				-0.158	0.020	0.218
Case 2	Y-dir. HalfHeight (ch.4)	12.908	12.906	132.94	0.008	0.067	0.145
	Y-dir. TP3 (ch.5)				0.020	0.158	0.143
	Y-dir. TP4 (ch.6)				0.020	0.158	-0.223
	X-dir. HalfHeight (ch.1)				-0.066	0.138	-0.223
	X-dir. TP1 (ch.2)				-0.155	0.019	-0.214
Case 3	X-dir. TP2 (ch.3)	12.713	12.711	129.22	-0.155	0.019	0.214
	Y-dir. HalfHeight (ch.4)				0.008	0.066	0.131
	Y-dir. TP3 (ch.5)				0.019	0.156	0.218
	Y-dir. TP4 (ch.6)				0.019	0.156	-0.219
	X-dir. HalfHeight (ch.1)				-0.065	0.008	-0.113
	X-dir. TP1 (ch.2)				-0.152	0.018	-0.218
Case 4	X-dir. TP2 (ch.3)	12.407	12.405	124.15	-0.152	0.018	0.218
	Y-dir. HalfHeight (ch.4)				0.008	0.065	0.113
	Y-dir. TP3 (ch.5)				0.018	0.152	0.223
	Y-dir. TP4 (ch.6)				0.018	0.152	-0.223
	X-dir. HalfHeight (ch.1)				-0.068	0.000	0.177
	X-dir. TP1 (ch.2)				-0.159	-0.001	0.180
Case 5	X-dir. TP2 (ch.3)	12.935	12.878	129.96	-0.159	-0.001	-0.218
Case 3	Y-dir. HalfHeight (ch.4)	12.933	12.070	129.90	0.000	-0.068	-0.132
	Y-dir. TP3 (ch.5)				0.001	-0.159	-0.204
	Y-dir. TP4 (ch.6)				0.000	-0.159	0.204
	X-dir. HalfHeight (ch.1)				-0.067	0.000	0.131
	X-dir. TP1 (ch.2)				-0.157	-0.001	0.181
00000	X-dir. TP2 (ch.3)	40 704	10.004	107.04	-0.157	-0.001	-0.227
Case 6	Y-dir. HalfHeight (ch.4)	12.731	12.691	127.81	0.001	-0.067	-0.129
	Y-dir. TP3 (ch.5)				0.001	-0.157	-0.212
	Y-dir. TP4 (ch.6)				0.001	-0.157	0.212
	X-dir. HalfHeight (ch.1)				-0.065	-0.002	0.082
	X-dir. TP1 (ch.2)				-0.152	-0.005	0.202
	` ,				-0.151	-0.005	-0.233
Case 7	X-dir. TP2 (ch.3)	12.337	12.316	119.86	-U. 10 I	-0.000	-U.Z.J.)

Accelerometer	$f_X$ $[Hz]$	$f_Y \\ [Hz]$	$f_T$ $[Hz]$	$u_X$	$u_Y$	$u_T$
Y-dir. TP3 (ch.5)				0.005	-0.152	-0.196
Y-dir. TP4 (ch.6)				0.004	-0.152	0.198

## Natural frequencies and mode shapes of scaled jacket structure using OMA

State	Accelerometer	$f_X \ [Hz]$	$f_Y \ [Hz]$	$f_T$ $[Hz]$	$u_X$	$u_Y$	$u_T$
	X-dir. HalfHeight (ch.1)				0.468	-0.104	0.467
	X-dir. TP1 (ch.2)				1.000 0.994	-0.076	0.911
Healthy	X-dir. TP2 (ch.3)	12.874	13.285	142.720		-0.086	-0.898
	Y-dir. HalfHeight (ch.4)				0.088 0.089	0.515	-0.477
	Y-dir. TP3 (ch.5) Y-dir. TP4 (ch.6)				0.083	0.975 1.000	-0.975 1.000
	· · · · · · · · · · · · · · · · · · ·				0.593	-0.075	0.470
	X-dir. HalfHeight (ch.1) X-dir. TP1 (ch.2)				1.000	-0.073	0.470
	` ,				0.996	-0.072 -0.085	-0.899
Healthy	X-dir. TP2 (ch.3)	12.667	13.340	142.670	0.990	0.525	-0.699 -0.479
	Y-dir. HalfHeight (ch.4)				0.009	0.525	-0.479 -0.976
	Y-dir. TP3 (ch.5) Y-dir. TP4 (ch.6)				0.102	1.000	1.000
	X-dir. HalfHeight (ch.1)				0.107	-0.113	0.470
	X-dir. TP1 (ch.2)				1.000	-0.113 -0.157	0.470
	X-dir. TP1 (ch.2) X-dir. TP2 (ch.3)				0.993	-0.137	-0.898
Healthy	Y-dir. HalfHeight (ch.4)	12.781	13.354	142.530	0.993	0.530	-0.696 -0.479
	Y-dir. TP3 (ch.5)				0.077	0.955	-0.479 -0.976
	Y-dir. TP4 (ch.6)				0.131	1.000	1.000
	X-dir. HalfHeight (ch.1)				0.137	-0.080	0.469
	X-dir. TP1 (ch.2)				1.000	-0.104	0.409
	X-dir. TP1 (ch.2) X-dir. TP2 (ch.3)				1.000	-0.10 <del>4</del> -0.112	-0.898
Healthy	Y-dir. HalfHeight (ch.4)	12.620	13.310	142.520	0.061	0.535	-0.479
	Y-dir. TP3 (ch.5)				0.001	0.965	-0.479
	Y-dir. TP4 (ch.6)				0.093	1.000	1.000
	X-dir. HalfHeight (ch.1)				0.585	-0.106	0.470
	X-dir. TP1 (ch.2)				1.000	-0.146	0.470
	X-dir. TP2 (ch.3)				0.998	-0.161	-0.898
Healthy	Y-dir. HalfHeight (ch.4)	12.611	13.225	142.620	0.068	0.533	-0.479
	Y-dir. TP3 (ch.5)				0.111	0.957	-0.976
	Y-dir. TP4 (ch.6)				0.116	1.000	1.000
	X-dir. HalfHeight (ch.1)				0.582	-0.102	0.470
	X-dir. TP1 (ch.2)				1.000	-0.132	0.911
	X-dir. TP2 (ch.3)				0.998	-0.148	-0.899
Healthy	Y-dir. HalfHeight (ch.4)	12.754	13.350	142.650	0.070	0.529	-0.479
	Y-dir. TP3 (ch.5)				0.127	0.962	-0.976
	Y-dir. TP4 (ch.6)				0.131	1.000	1.000
	X-dir. HalfHeight (ch.1)				0.585	-0.085	0.470
	X-dir. TP1 (ch.2)				1.000	-0.109	0.910
11 10	X-dir. TP2 (ch.3)	40.000	40 400	4.40.000	0.999	-0.123	-0.899
Healthy	Y-dir. HalfHeight (ch.4)	12.606	13.183	142.680	0.058	0.535	-0.480
	Y-dir. TP3 (ch.5)				0.093	0.960	-0.976

State	Accelerometer	$f_X$	$f_Y$	$f_T$	$u_X$	$u_Y$	$u_T$
		[Hz]	[Hz]	[Hz]			
	Y-dir. TP4 (ch.6)				0.097	1.000	1.000
	X-dir. HalfHeight (ch.1)				0.586	-0.076	0.470
	X-dir. TP1 (ch.2)				1.000 0.998	-0.095 -0.110	0.911 -0.898
Healthy	X-dir. TP2 (ch.3) Y-dir. HalfHeight (ch.4)	12.644	13.337	142.560	0.030	0.536	-0.696 -0.479
	Y-dir. TP3 (ch.5)				0.030	0.961	-0.47 <i>9</i> -0.976
	Y-dir. TP4 (ch.6)				0.040	1.000	1.000
	X-dir. HalfHeight (ch.1)				0.585	-0.074	0.471
	X-dir. TP1 (ch.2)				1.000	-0.074	0.910
	X-dir. TP2 (ch.3)				1.000	-0.109	-0.898
Healthy	Y-dir. HalfHeight (ch.4)	12.584	13.198	142.580	0.026	0.534	-0.480
	Y-dir. TP3 (ch.5)				0.035	0.958	-0.976
	Y-dir. TP4 (ch.6)				0.037	1.000	1.000
-	X-dir. HalfHeight (ch.1)				0.592	-0.013	-0.468
	X-dir. TP1 (ch.2)				1.000	-0.027	-0.911
	X-dir. TP2 (ch.3)				0.991	-0.048	0.843
Case 1	Y-dir. HalfHeight (ch.4)	11.622	12.195	141.900	0.047	0.533	0.489
	Y-dir. TP3 (ch.5)				0.078	0.959	1.000
	Y-dir. TP4 (ch.6)				0.083	1.000	-0.914
	X-dir. HalfHeight (ch.1)				0.587	-0.032	-0.468
	X-dir. TP1 (ch.2)		12.142		1.000	-0.023	-0.907
	X-dir. TP2 (ch.3)	44.044			0.998	-0.039	0.844
Case 1	Y-dir. HalfHeight (ch.4)	11.644		141.980	0.049	0.532	0.490
	Y-dir. TP3 (ch.5)				0.074	0.951	1.000
	Y-dir. TP4 (ch.6)				0.081	1.000	-0.916
	X-dir. HalfHeight (ch.1)				0.585	-0.072	-0.468
	X-dir. TP1 (ch.2)				1.000	-0.089	-0.909
Case 1	X-dir. TP2 (ch.3)	11.625	12 222	141 020	1.000	-0.107	0.848
Case	Y-dir. HalfHeight (ch.4)	11.025	12.233	141.920	0.077	0.533	0.490
	Y-dir. TP3 (ch.5)				0.128	0.951	1.000
	Y-dir. TP4 (ch.6)				0.134	1.000	-0.921
	X-dir. HalfHeight (ch.1)				0.591	-0.136	0.565
	X-dir. TP1 (ch.2)				1.000	-0.196	0.898
Case 2	X-dir. TP2 (ch.3)	12.778	13.392	137.990	0.995	-0.214	-0.894
0030 2	Y-dir. HalfHeight (ch.4)	12.770	10.002	107.550	0.071	0.517	-0.556
	Y-dir. TP3 (ch.5)				0.141	0.949	-0.966
	Y-dir. TP4 (ch.6)				0.140	1.000	1.000
	X-dir. HalfHeight (ch.1)				0.591	-0.028	0.563
	X-dir. TP1 (ch.2)				0.999	-0.026	0.898
Case 2	X-dir. TP2 (ch.3)	12.538	13.018	138.000	1.000	-0.046	-0.893
2000 =	Y-dir. HalfHeight (ch.4)				0.021	0.536	-0.561
	Y-dir. TP3 (ch.5)				0.030	0.960	-0.967
	Y-dir. TP4 (ch.6)				0.036	1.000	1.000
	X-dir. HalfHeight (ch.1)				0.585	-0.099	0.562
	X-dir. TP1 (ch.2)				1.000	-0.150	0.896
Case 2	X-dir. TP2 (ch.3)	12.722	13.318	138.120	0.994	-0.167	-0.892
	Y-dir. HalfHeight (ch.4)				0.073	0.535	-0.559
	Y-dir. TP3 (ch.5)				0.118	0.959	-0.963

State	Accelerometer	$f_X$	$f_Y$	$f_T$	$u_X$	$u_Y$	$u_T$
	Y-dir. TP4 (ch.6)	[Hz]	[Hz]	[Hz]	0.126	1.000	1.000
	X-dir. HalfHeight (ch.1)				0.120	-0.101	0.446
	X-dir. TP1 (ch.2)				1.000	-0.101	0.901
	X-dir. TP2 (ch.3)				0.999	-0.107 -0.125	-0.900
Case 3	Y-dir. HalfHeight (ch.4)	12.488	13.221	134.410	0.085	0.536	-0.446
	Y-dir. TP3 (ch.5)				0.142	0.961	-0.974
	Y-dir. TP4 (ch.6)				0.150	1.000	1.000
	X-dir. HalfHeight (ch.1)				0.587	-0.076	0.454
	X-dir. TP1 (ch.2)				1.000	-0.067	0.899
	X-dir. TP2 (ch.3)				0.997	-0.087	-0.899
Case 3	Y-dir. HalfHeight (ch.4)	12.632	13.070	134.700	0.010	0.535	-0.452
	Y-dir. TP3 (ch.5)				0.009	0.961	-0.970
	Y-dir. TP4 (ch.6)				0.011	1.000	1.000
	X-dir. HalfHeight (ch.1)				0.585	-0.113	0.450
	X-dir. TP1 (ch.2)				0.999	-0.128	0.901
	X-dir. TP2 (ch.3)				1.000	-0.148	-0.901
Case 3	Y-dir. HalfHeight (ch.4)	12.356	13.058	134.370	0.046	0.537	-0.449
	Y-dir. TP3 (ch.5)				0.070	0.963	-0.974
	Y-dir. TP4 (ch.6)				0.074	1.000	1.000
	X-dir. HalfHeight (ch.1)				0.580	-0.122	0.284
	X-dir. TP1 (ch.2)		12.894		1.000	-0.151	0.904
	X-dir. TP2 (ch.3)				0.995	-0.167	-0.903
Case 4	Y-dir. HalfHeight (ch.4)	12.263		128.150	0.050	0.530	-0.288
	Y-dir. TP3 (ch.5)				0.079	0.959	-0.975
	Y-dir. TP4 (ch.6)				0.082	1.000	1.000
	X-dir. HalfHeight (ch.1)				0.597	-0.060	0.286
	X-dir. TP1 (ch.2)				0.993	-0.061	0.902
	X-dir. TP2 (ch.3)	10.001	10010	400 400	1.000	-0.105	-0.902
Case 4	Y-dir. HalfHeight (ch.4)	12.261	12.949	128.160	-0.010	0.529	-0.287
	Y-dir. TP3 (ch.5)				-0.034	0.925	-0.970
	Y-dir. TP4 (ch.6)				-0.043	1.000	1.000
	X-dir. HalfHeight (ch.1)				0.583	-0.117	0.285
	X-dir. TP1 (ch.2)				1.000	-0.135	0.904
	X-dir. TP2 (ch.3)	4004=	40.000	400.000	0.997	-0.153	-0.903
Case 4	Y-dir. HalfHeight (ch.4)	12.215	12.956	128.080	0.041	0.531	-0.287
	Y-dir. TP3 (ch.5)				0.063	0.957	-0.975
	Y-dir. TP4 (ch.6)				0.065	1.000	1.000
	X-dir. HalfHeight (ch.1)				0.594	-0.112	1.000
	X-dir. TP1 (ch.2)				1.000	-0.130	0.692
0	X-dir. TP2 (ch.3)	40.740	40 457	404.070	0.987	-0.146	-0.910
Case 5	Y-dir. HalfHeight (ch.4)	12.713	13.157	134.670	0.073	0.535	-0.457
	Y-dir. TP3 (ch.5)				0.126	0.963	-0.868
	Y-dir. TP4 (ch.6)				0.144	1.000	0.915
	X-dir. HalfHeight (ch.1)				0.592	-0.161	1.000
	X-dir. TP1 (ch.2)				1.000	-0.213	0.697
0-5-5	X-dir. TP2 (ch.3)	40.000	40.040	404.000	0.986	-0.226	-0.916
Case 5	Y-dir. HalfHeight (ch.4)	12.806	13.319	134.690	0.068	0.535	-0.455
	Y-dir. TP3 (ch.5)				0.116	0.964	-0.879
-	( /					*	

State	Accelerometer	$f_X$	$f_Y$	$f_T$	$u_X$	$u_Y$	$u_T$
	Y-dir. TP4 (ch.6)	[Hz]	[Hz]	[Hz]	0.132	1.000	0.916
	X-dir. HalfHeight (ch.1)				0.132	-0.096	1.000
	X-dir. TP1 (ch.2)				1.000	-0.102	0.692
	X-dir. TP2 (ch.3)				0.984	-0.102	-0.912
Case 5	Y-dir. HalfHeight (ch.4)	12.827	13.321	134.730	0.904	0.537	-0.452
	Y-dir. TP3 (ch.5)				0.137	0.960	-0.432
	Y-dir. TP4 (ch.6)				0.157	1.000	0.912
	X-dir. HalfHeight (ch.1)				0.591	-0.148	-0.486
	X-dir. TP1 (ch.2)				1.000	-0.188	-0.770
	X-dir. TP2 (ch.3)				0.985	-0.201	1.000
Case 6	Y-dir. HalfHeight (ch.4)	12.559	13.016	132.480	0.082	0.539	0.403
	Y-dir. TP3 (ch.5)				0.149	0.961	0.966
	Y-dir. TP4 (ch.6)				0.173	1.000	-0.939
	X-dir. HalfHeight (ch.1)				0.595	-0.121	-0.486
	X-dir. TP1 (ch.2)				1.000	-0.149	-0.766
_	X-dir. TP2 (ch.3)				0.987	-0.165	1.000
Case 6	Y-dir. HalfHeight (ch.4)	12.532	13.052	132.450	-0.008	0.537	0.403
	Y-dir. TP3 (ch.5)				-0.013	0.960	0.964
	Y-dir. TP4 (ch.6)				0.003	1.000	-0.938
	X-dir. HalfHeight (ch.1)				0.591	-0.157	-0.485
	X-dir. TP1 (ch.2)	12.476	13.009		1.000	-0.206	-0.768
00	X-dir. TP2 (ch.3)			400 440	0.987	-0.220	1.000
Case 6	Y-dir. HalfHeight (ch.4)			132.440	0.042	0.539	0.402
	Y-dir. TP3 (ch.5)				0.076	0.962	0.963
	Y-dir. TP4 (ch.6)				0.096	1.000	-0.940
	X-dir. HalfHeight (ch.1)				0.575	-0.134	-0.217
	X-dir. TP1 (ch.2)		12.433	129.790	1.000	-0.153	-0.853
Case 7	X-dir. TP2 (ch.3)	12.056			0.979	-0.178	1.000
Case 1	Y-dir. HalfHeight (ch.4)	12.000	12.433		0.191	0.538	0.326
	Y-dir. TP3 (ch.5)				0.328	0.965	0.965
	Y-dir. TP4 (ch.6)				0.368	1.000	-0.907
	X-dir. HalfHeight (ch.1)				0.584	-0.192	-0.204
	X-dir. TP1 (ch.2)				1.000	-0.269	-0.844
Case 7	X-dir. TP2 (ch.3)	12.044	12.423	129.070	0.983	-0.280	1.000
Ouse 1	Y-dir. HalfHeight (ch.4)	12.044	12.420	123.070	0.169	0.537	0.315
	Y-dir. TP3 (ch.5)				0.297	0.971	0.957
	Y-dir. TP4 (ch.6)				0.330	1.000	-0.900
	X-dir. HalfHeight (ch.1)				0.587	-0.094	-0.214
	X-dir. TP1 (ch.2)			129.900	1.000	-0.093	-0.856
Case 7	X-dir. TP2 (ch.3)	12.110	12.522		0.991	-0.112	1.000
	Y-dir. HalfHeight (ch.4)	3			0.035	0.538	0.328
	Y-dir. TP3 (ch.5)				0.053	0.967	0.966
	Y-dir. TP4 (ch.6)				0.077	1.000	-0.908

# A.5 Relative frequency difference and MAC values

## A.5.1 Three-story Frame Structure

Nama		Manas						
Name	VS.	Name	$\delta_{f_1}$	$\delta_{f_2}$	$\delta_{f_3}$	$MAC_1$	$MAC_2$	$MAC_3$
of test		of DT	[%]	[%]	[%]	4.0000	0.0000	0.0000
Healthy	VS.	HDT	0.01	0.14	0.15	1.0000	0.9990	0.9980
Healthy	VS.	HDT	0.17	0.12	0.04	0.9926	0.9995	0.9984
Healthy	VS.	HDT	0.01	0.12	0.11	0.9935	0.9993	0.9986
Healthy	VS.	HDT	0.11	0.12	0.09	0.9988	0.9990	0.9978
Healthy	VS.	HDT	0.06	0.01	0.07	0.9990	0.9991	0.9982
Healthy	VS.	HDT	0.34	0.01	0.03	0.9960	0.9990	0.9984
Healthy	VS.	HDT	0.16	0.09	0.01	0.9961	0.9998	0.9994
Healthy	VS.	HDT	0.06	0.13	0.16	0.9980	0.9998	0.9991
Healthy	VS.	HDT	0.06	0.15	0.05	0.9983	0.9997	0.9987
38gMass 1stFloor	VS.	Case 1	0.60	0.34	0.85	0.9947	0.9988	0.9978
38gMass 1stFloor	VS.	Case 1	0.87	0.34	0.84	0.9946	0.9992	0.9976
38gMass 1stFloor	VS.	Case 1	0.25	0.38	0.63	0.9845	0.9994	0.9986
38gMass 2ndFloor	VS.	Case 2	0.08	0.47	0.73	0.9912	0.9994	0.9985
38gMass 2ndFloor	VS.	Case 2	0.32	0.46	0.56	0.9982	0.9992	0.9990
38gMass 2ndFloor	VS.	Case 2	0.21	0.38	0.33	0.9942	0.9998	0.9993
38gMass 3rdFloor	VS.	Case 3	0.02	0.26	0.23	0.9918	0.9993	0.9983
38gMass 3rdFloor	VS.	Case 3	0.19	0.20	0.01	0.9954	0.9987	0.9986
38gMass 3rdFloor	VS.	Case 3	0.55	0.27	0.05	0.9960	0.9998	0.9993
38gMass 1st&2ndFloor	VS.	Case 4	0.17	0.71	1.28	0.9919	0.9996	0.9980
38gMass 1st&2ndFloor	VS.	Case 4	0.29	0.96	1.09	0.9921	0.9989	0.9976
38gMass 1st&2ndFloor	VS.	Case 4	0.12	0.50	1.15	0.9957	0.9999	0.9991
38gMass 1st&3rdFloor	VS.	Case 5	1.62	0.38	0.71	0.9920	0.9992	0.9975
38gMass 1st&3rdFloor	VS.	Case 5	1.28	0.40	0.78	0.9970	0.9991	0.9981
38gMass 1st&3rdFloor	VS.	Case 5	0.08	0.10	0.21	0.9909	0.9996	0.9986
38gMass 2nd&3rdFloor	VS.	Case 6	0.03	0.63	0.52	0.9984	0.9993	0.9989
38gMass 2nd&3rdFloor	VS.	Case 6	0.38	0.46	0.53	0.9938	0.9991	0.9990
38gMass 2nd&3rdFloor	VS.	Case 6	0.03	0.34	0.61	0.9920	1.0000	0.9993
38gMass 1st&2nd&3rdFloor	VS.	Case 7	0.11	0.75	1.53	0.9936	0.9996	0.9990
38gMass 1st&2nd&3rdFloor	VS.	Case 7	0.07	1.08	1.19	0.9971	0.9994	0.9983
38gMass 1st&2nd&3rdFloor	VS.	Case 7	0.07	0.57	1.17	0.9954	0.9998	0.9994

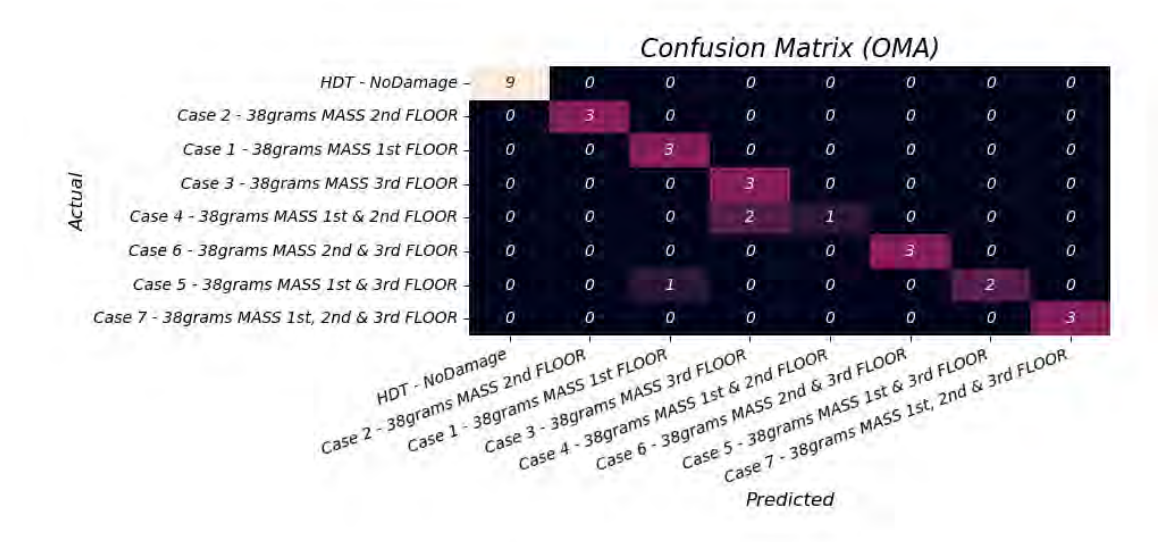
### A.5.2 Scaled Jacket Structure

Name	VC	Name	$\delta_{f_X}$	$\delta_{f_Y}$	$\delta_{f_T}$	$MAC_X$	$MAC_{Y}$	$MAC_T$
of test	VS.	of DT	[%]	[%]	[%]	MACX	MACY	$MAC_T$
Healthy	VS.	HDT	2.42	0.76	0.06	0.9523	0.9498	0.9975
Healthy	VS.	HDT	4.10	1.17	0.09	0.9392	0.9528	0.9976
Healthy	VS.	HDT	3.17	1.27	0.19	0.9278	0.9114	0.9976
Healthy	VS.	HDT	4.48	0.95	0.20	0.9452	0.9405	0.9976
Healthy	VS.	HDT	4.56	0.31	0.13	0.9369	0.9178	0.9976
Healthy	VS.	HDT	3.39	1.24	0.11	0.9309	0.9248	0.9976
Healthy	VS.	HDT	4.60	0.01	0.08	0.9448	0.9365	0.9977
Healthy	VS.	HDT	4.29	1.15	0.17	0.9624	0.9430	0.9976
Healthy	VS.	HDT	4.78	0.11	0.15	0.9659	0.9435	0.9977
6.72kgMass TopPlate	VS.	Case 1	3.87	1.02	1.75	0.9520	0.9718	0.9959

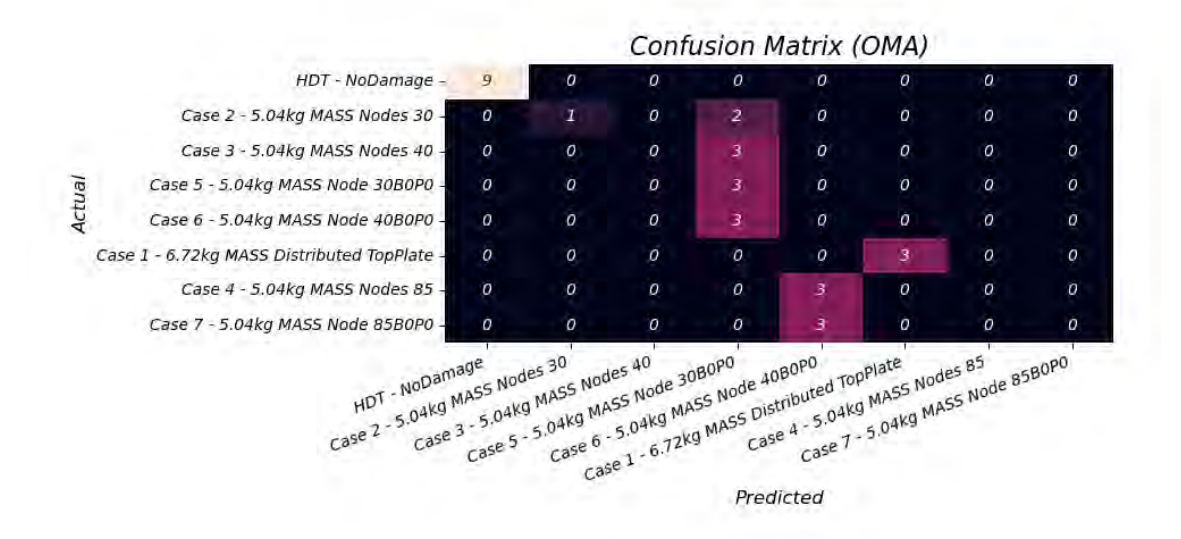
Name	VS.	Name	$\delta_{f_X}$	$\delta_{f_Y}$	$\delta_{f_T}$	$MAC_X$	$MAC_{Y}$	$MAC_T$
of test		of DT	[%]	[%]	[%]			
6.72kgMass TopPlate	VS.	Case 1	3.68	0.58	1.80	0.9538	0.9720	0.9960
6.72kgMass TopPlate	VS.	Case 1	3.85	1.32	1.76	0.9324	0.9473	0.9961
5.04kgMass Nodes30	VS.	Case 2	1.02	3.63	3.66	0.9233	0.8864	0.9975
5.04kgMass Nodes30	VS.	Case 2	2.95	0.86	3.67	0.9652	0.9678	0.9976
5.04kgMass Nodes30	VS.	Case 2	1.46	3.09	3.75	0.9312	0.9144	0.9975
5.04kgMass Nodes40	VS.	Case 3	1.80	3.86	3.86	0.9219	0.9341	0.9920
5.04kgMass Nodes40	VS.	Case 3	0.64	2.75	4.07	0.9726	0.9517	0.9928
5.04kgMass Nodes40	VS.	Case 3	2.89	2.66	3.83	0.9532	0.9233	0.9923
5.04kgMass Nodes85	VS.	Case 4	1.17	3.79	3.12	0.9507	0.9132	0.9805
5.04kgMass Nodes85	VS.	Case 4	1.19	4.20	3.13	0.9813	0.9492	0.9806
5.04kgMass Nodes85	VS.	Case 4	1.57	4.25	3.07	0.9567	0.9207	0.9804
5.04kgMass Node30B0P0	VS.	Case 5	1.75	2.12	3.50	0.9703	0.9708	0.9812
5.04kgMass Node30B0P0	VS.	Case 5	1.01	3.31	3.51	0.9733	0.9406	0.9817
5.04kgMass Node30B0P0	VS.	Case 5	0.84	3.33	3.54	0.9678	0.9781	0.9811
5.04kgMass Node40B0P0	VS.	Case 6	1.37	2.50	3.53	0.9631	0.9499	0.9912
5.04kgMass Node40B0P0	VS.	Case 6	1.59	2.77	3.50	0.9885	0.9642	0.9913
5.04kgMass Node40B0P0	VS.	Case 6	2.04	2.44	3.50	0.9812	0.9425	0.9912
5.04kgMass Node85B0P0	VS.	Case 7	2.33	0.94	7.65	0.8625	0.9505	0.9875
5.04kgMass Node85B0P0	VS.	Case 7	2.43	0.86	7.14	0.8828	0.8995	0.9860
5.04kgMass Node85B0P0	VS.	Case 7	1.87	1.65	7.73	0.9804	0.9728	0.9873

## A.6 Confusion matrix for method using no weights

### A.6.1 Three-story frame structure



### A.6.2 Scaled jacket structure



# A.7 List of scripts and description

The list below gives a short description of the main Python scripts used in this project. The scripts along with the various functions utilized, and all the data are included in the accompanying  $MasterThesis\_GianMaratta.zip$  folder.

Script	Application	Description
read_TDMS_Modified	Reading tdms files	Used to read the data obtained from the experiments using FlexLogger.
EMA-Hammer-3story	Experimental Modal Analysis in a 3-story frame structure	Signal processing of recorded accelerations and modal identification using Welch's method and SDyPy package. The script is built to excite a 3-story frame structure with an impact hammer.
OMA_3story	Operational Modal Analysis in a 3-story frame structure	Signal processing of recorded accelerations and modal identification of a 3-story frame structure using FDD from pyOMA2 package.
OMA_Jacket	Operational Modal Analysis in a scaled jacket structure	Signal processing of recorded accelerations and modal identification of a scaled jacket structure using FDD from pyOMA2 package.
BoxPlotsAnalysis	Generation of box plot figures	Comparison between the updated finite element model and the experiments. The comparison is performed in terms of natural frequencies and MAC values.
DamageDetectionEMA_3Story	Damage detection performed in a 3-story frame structure using EMA	The modal properties of the experiments are extracted using $EMA-Hammer.py$ . Relative frequency difference and MAC values are calculated and used as parameters to calculate Euclidean distances and predict the type and location of damage.

DamageDetectionOMA\_3Story

Damage detection performed in a 3-story frame structure using OMA

The modal properties of the experiments are extracted using  $OMA\_3story.py$ . Relative frequency differences and MAC values are calculated and used as parameters to calculate Euclidean distances and predict the type and location of damage.

DamageDetectionOMA\_Jacket

Damage detection performed in a scaled jacket structure using OMA

The modal properties of the experiments are extracted using  $OMA\_3story.py$ . Relative frequency differences and MAC values are calculated and used as parameters to calculate Euclidean distances and predict the type and location of damage.

Technical University of Denmark

Koppels Allé, Building 404 2800 Kgs. Lyngby, Denmark Tlf. 4525 1700

www.construct.dtu.dk